ABSTRACT

JEROME, AKASH. Flame Synthesis of Silica Nanoparticles in External Electric Fields. (Under the direction of Dr. Alexei V. Saveliev).

Interest in the field of nanotechnology has had an upward trajectory in recent decades. The advancement of nanotechnology stems from its impact on electronics, information technology, memory storage, and sensing industries, driving global digitization. Various methods are currently available for producing sub-micron-sized particles essential for nanotechnology. Flame synthesis has emerged as a highly efficient, one-step, continuous, and scalable method for nanoparticle production. Flame synthesis offers advantages such as short residence times and ease of processing. Flame synthesis at the industrial scale is often carried out in hydrocarbon flames. Several process variables are utilized to control particle characteristics and collection in these reactors, such as equivalence ratio, gas mixture velocity, precursor introduction method, process temperature, and charging. Charging is particularly important since it narrows down the particle size distribution and improves the particle collection.

In this study, flame-generated particles are charged by applying an electric field across the flame volume during their synthesis in hydrocarbon flames. The effect of flame-generated nanoparticles on the flame Voltage-Current Characteristics (VCC) is studied experimentally. The particles are formed by adding hexamethyldisiloxane to a premixed methane-air flat flame. The VCC measurements are performed with negative and positive DC polarities that range from -30 kV to 30 kV. The VCC of the particle-laden flame is observed to be vastly different from a pristine flame. Overextended deposition times, a high-resistivity layer of silica nanoparticles accumulates on the mesh electrode. This buildup influences the flame current by generating secondary charge carriers.

The particles collected on the electrode are weighed and characterized using electron microscopy. Maximum production of nanoparticles was marked by the peak in particle yield. Overlaying the current and particle yield trends revealed that maximum collection occurs at the voltage corresponding to the peak current. Electron microscopy images of the collected particles show that the particle size distribution is marginally smaller under a negative e-field.

The density of the nanoparticle cloud upstream and downstream of the electrode is visualized utilizing laser imaging. Rayleigh scattered intensity indicates that the particle density upstream of the electrode remains relatively unchanged. The scattered intensity downstream of the electrode exhibits a trend opposite that of the particle yield measurement. An ion-flame mechanism including the decomposition of silicon precursor is used to predict the flame characteristics such as temperature and charged species concentration for seeded and unseeded flames.

Flame Synthesis of Silica Nanoparticles in External Electric Fields

by
Akash Jerome

A dissertation submitted to the Graduate Faculty of
North Carolina State University
in partial fulfillment of the
requirements for the degree of
Doctor of Philosophy

Mechanical Engineering

Raleigh, North Carolina
2025

APPROVED BY:

Dr. Alexei Saveliev Committee Chair	Dr. Tarek Echekki
Dr. Tiegang Fang	Dr. Kevin Lyons
Dr. Elizabeth Kautz	

DEDICATION

To the Lord Jesus Christ, my parents, sister, friends, and extended family who put up with the highs and lows.

BIOGRAPHY

Akash Jerome was born in 1994 in Chennai, a coastal city in south-east India, to Mr. Martin Pragasam and Mrs. Rita Nirmala. From a young age, he developed a passion for mechanical engineering, reflected in his extensive model collection.

He earned his bachelor's degree in mechanical engineering from Loyola-ICAM College of Engineering and Technology, Chennai. During his undergraduate studies, he worked on several projects, including designing a hand-driven tiller and developing a cost-effective device for inducing Neonatal Therapeutic Hypothermia. Akash also participated in the SAE BAJA competition.

To further pursue his passion, he enrolled at North Carolina State University, where he joined Dr. Tiegang Fang's research group. There, Akash focused on studying combustion processes in internal combustion engines and conducting research on fuel jet dynamics.

He then enrolled at North Carolina State University, where he joined Dr. Alexei Saveliev's research group for his doctoral academics. He researched the flame synthesis of silica nanoparticles under the influence of external electric fields.

ACKNOWLEDGMENTS

I would like to express my heartfelt gratitude to Dr. Alexei Saveliev for his patient guidance throughout my academic journey. I am also deeply thankful to my committee members—Dr. Kevin Lyons, Dr. Tiegang Fang, Dr. Tarek Echekki, and Dr. Elizabeth Kautz—for their valuable insights and support.

A special thanks to my parents, Mr. Martin Pragasam and Mrs. Rita Nirmala, for their unwavering encouragement throughout my graduate studies. I am profoundly grateful to my sister, Mrs. Arthi Grace Jackson, my brother-in-law, Mr. Jackson Pillai, and my wonderful godchild, Ms. Gianna Maria Jackson, for their love and inspiration.

I am fortunate to have had the continuous support and friendship of Dr. Moses, Dr. Bala, Dr. Ramakrishna, Dr. Arun, Dr. Abinash, Vaishnavi, Divya, Dheepak, Asok, Dan, Josin, Rosemary, Shakthi, Uma, Ganesh, Anisha and soon-to-be Dr. Hari, Madusudhan and Meghna. Their encouragement has been invaluable.

Finally, I extend my gratitude to the staff of MAE and NCSU for their assistance during my graduate studies. I would especially like to thank Dr. Christopher Winkler and Charles Mooney from AIF for their support with electron microscopy imaging, as well as Cheryl Tran for her help with my TA appointments. Additionally, my sincere thanks to Mr. Steve Cameron and Mr. Vincent Chicarelli from the machine shop for their guidance and expertise.

TABLE OF CONTENTS

LIST OF TABLES

LIST OF FIGURES

CHAPTER 1: Introduction

1.1 Combustion and particle synthesis

Combustion is a rapid exothermic reaction that results in the conversion of the fuel's chemical energy into thermal energy. During combustion the fuel undergoes oxidation, breaking down into simpler molecules producing energy mainly in the form of heat light. The main reaction products of combustion of hydrocarbon fuels are carbon dioxide and water vapor. Carbon monoxide, nitrogen oxides, particulates, and harmful emissions are common byproducts depending on the fuel and flame conditions used. The thermal energy is then converted to electricity in a power plant or into mechanical work in an internal combustion engine. Combustion often produces solid or liquid particles, commonly called particulate matter (PM) (Wu, 2005). These particles vary in size and composition depending on the type of fuel, impurities, and flame parameters. Rapid heating and cooling during combustion produce materials with special structure, morphology, composition, and high purity levels (Changhui et al., 2008; Kusters et al., 1995). The PM produced in the combustion process is typically in the micron/sub-micron size range. Nanosized particles are known to have distinctly different properties compared to bulk materials due to the number of atoms on the surface being comparable to those within the particle (Andres et al., 1989). Due to their high surface-to-volume ratio, these particles find applications in catalysis, electronics, energy storage, photovoltaics, sensors, drug delivery, additives in fuels to improve combustion efficiency, and additives to materials to enhance their structural properties (Bonnemain, 1998; Munir, 1995; Gupta et al., 2005; Ulrich, 1984; Wang et al., 2017; Pratsinis et al., 1992; Zhao, Liu et al., 2008). Current methods for the production of nanomaterials are chemical vapor deposition, thermal decomposition, gas condensation, and wet chemistry (Aruna et al., 2008; Liu et al., 1999; Siegel et al., 1989; Siegel et al., 1988; Zhou et al., 2019). These methods involve several consecutive time-consuming steps such as precursor solution production, precipitation or sol-gel, filtration washing and drying, and calcination and drying. The complexity of these processes makes it difficult to control the properties of the particles and increases the difficulty in large-scale production.

1.2 Flame synthesis of nanoparticles

In recent times combustion synthesis or flame synthesis has emerged as a powerful method for the production of nanoparticles. The volume of production for flame-synthesized nanoparticles has scaled up to million metric tons per annum (Wegner et al., 2004). Certain chemicals introduced as precursors in the combustion mixture can produce desirable compounds in the form of particulate matter. The main advantage of nanomaterial production through combustion synthesis is attributed to the following characteristics:

- The source of energy is the heat of combustion that activates the pyrolysis, hydrolysis, and vaporization of the precursor.
- Parameters such as the equivalence ratio, flame velocity, and the residence time of the particles within the high-temperature zone may be varied to manipulate the morphology of the final particle.
- Flame synthesis is a single-step process compared to wet chemistry methods
- The particles are readily separated from the gas phase without the need for post-processing
- Particles produced by combustion synthesis have a narrow size distribution and are of high purity (Yuping Chen et al., 2010).
- Flame synthesis methods are highly scalable.

Flame synthesis is considered to be one of the most economical routes for the production of advanced materials in the sub-micron range. Sub-micron and nanomaterials are classified based on the number of dimensions. Four classes of nanomaterials can be obtained: zero-dimensional

(0D), one-dimensional (1D), two-dimensional (2D), and three-dimensional (3D). For 0D all dimensions (x, y, and z) are in the nanoscale, for 1D all but one dimension is in the nanoscale, for 2D all but one dimension is not in the nanoscale. 3D units consist of a variety of nanostructures, such as nanowires, and nanoflakes (Bielański et al., 1957; Halavaara et al., 2002; Stamatakis et al., 1991; Yu Ting, 2008).

1.2.1 Types of flame synthesis of nanoparticles

Due to the short duration of the reactions and rapid cooling during the combustion process, products with unique electrochemical, physical, biological, optical, and mechanical properties are produced (Pratsinis, 1996). Figure 1.1 shows the difference between the nanoparticle production of vanadium-based catalysts using the wet chemistry method and the flame synthesis method. The classic synthesis routes of co-precipitation or impregnation often involve multiple steps that take up to a few days. In contrast flame synthesis produces the end production in a single step and within a matter of minutes.

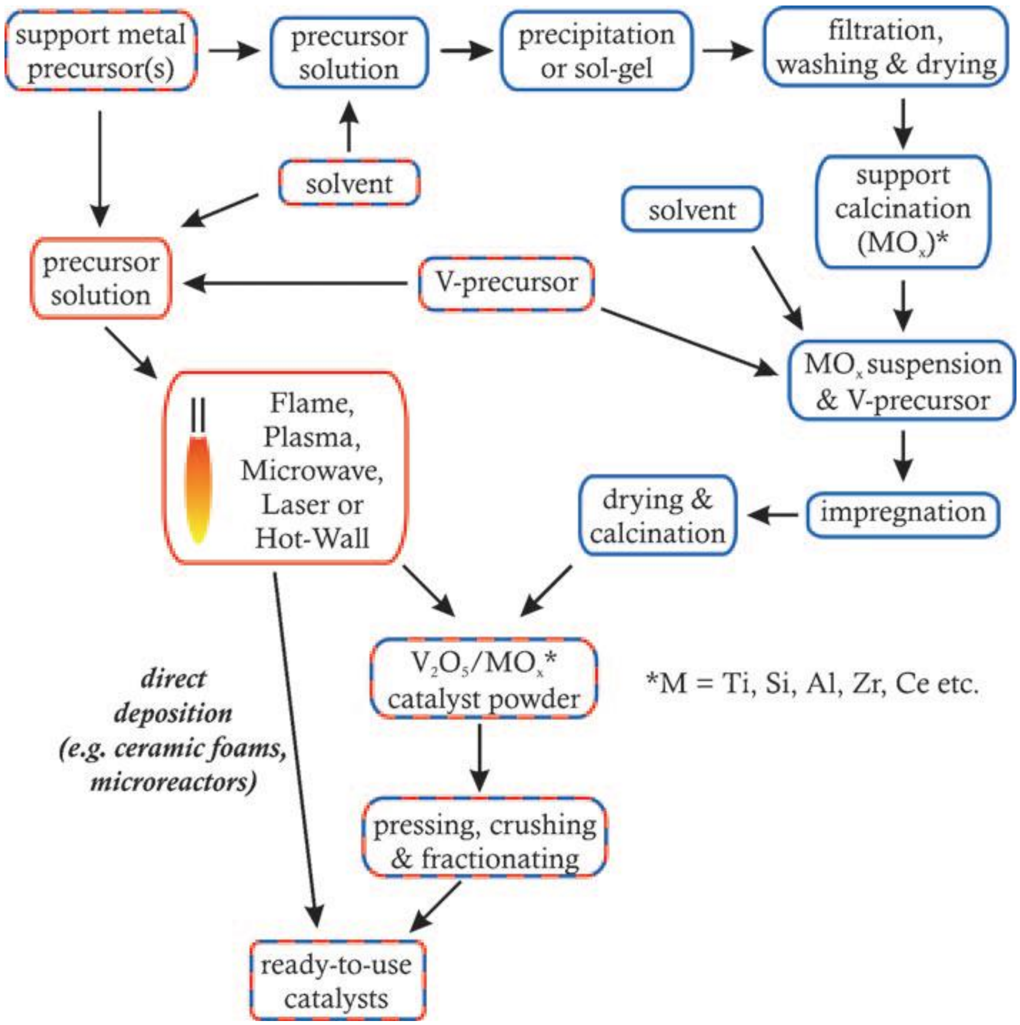

Figure 1.1. Comparison of wet chemistry (blue boxes) and flame synthesis method (red boxes) of vanadium nanoparticles (Kammler et al., 2002)

Based on the physical state of the reactive media, three methods of combustion synthesis processes can be distinguished: (1) solid-phase combustion synthesis (SP-CS), (2) solution combustion synthesis (SCS), and (3) gas-phase flame synthesis (FS).

In SP-CS, a self-sustaining combustion wave propagates through a solid mixture of the precursor and fuel using the heat released from the chemical reactions. Figure 1.2 shows a schematic of self-propagating high-temperature synthesis (SHS) which is a type of SP-CS (Morrison et al., 1997; Morsi, 2017; Vemury et al., 1997).

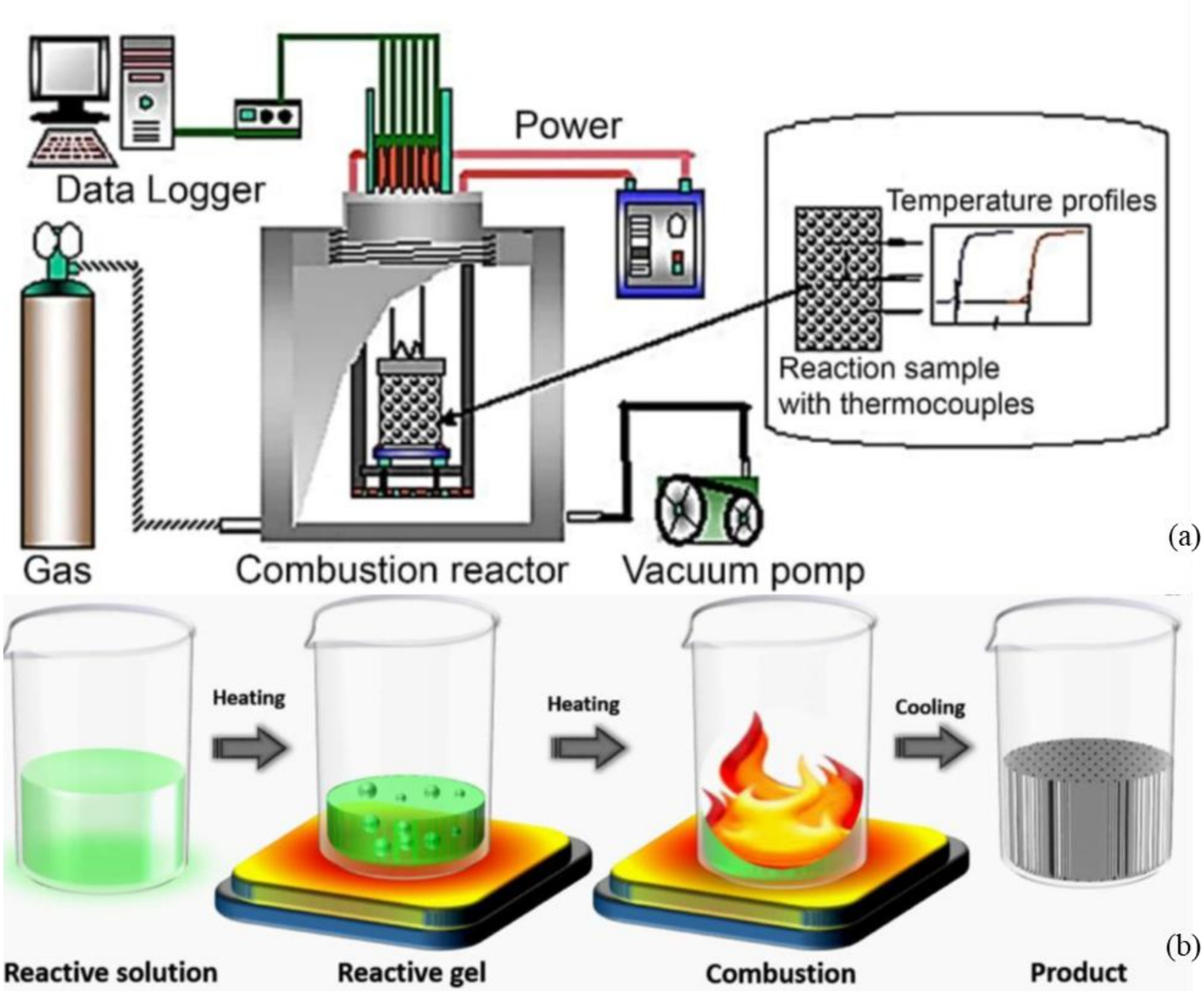

Figure 1.2. (a) Experimental set-up for the production of nanostructured materials using SP-CS (Kammler et al., 2003; Katzer et al., 2001), (b) Schematic representation of the various steps required for the SCS process (Xiong et al., 2017).

SHS in principle can be used for any solid-state exothermic mixture that can maintain a self-sustaining reaction and results in the production of useful products. The reaction pellet is produced by compacting a solid reaction mixture with the desired precursor powder into a cylindrical cup. To initiate the self-sustaining combustion wave, a heat or flame source is used on the surface of the solid reactants. This produces a thermal wave that propagates through the reactants converting the solid precursor's mixture into the desired products. The process typically is carried out in a high-pressure reactor filled with an inert gas such as argon or nitrogen.

Figure 1.2(a) shows SCS synthesis that involves a mixture of reactive media and oxidizers in the aqueous state (Vercoulen et al.,1994). The SCS process relies on exothermic self-sustaining reactions by using the reactive media and oxidizer solution (Fujimoto et al., 2003; Kammler et al., 2000). Figure 1.2(b) shows the steps necessary for the SCS process: (i) preparation of the combustion aqueous mixture, (ii) preheating the mixture to the reaction initiation temperature, (iii) combustion, and (iv) cooling. The most important step in SCS is the dissolving at a molecular level of solid precursor, fuel and oxidizer in a liquid solvent to produce the reactive solution. SCS may occur either by volume or layer-by-layer combustion wave propagation methods depending on the precursor and the conditions used for the process organization. SCS is often used for the synthesis of metal oxides.

In the FS process, a combustion reaction occurs in the gaseous phase (Katz et al., 1991). FS involves the combustion of gaseous fuels such as hydrocarbons or hydrogen with an oxidizer, often air. The precursor, which is a gaseous or atomized liquid is injected into the fuel stream and is ignited. The particles formed by combustion are collected for various uses such as the manufacturing of carbon black, silica, titania, zinc oxide, and alumina nanoparticles. It is also capable of producing various dimensions of nanoparticles. FS has the advantage of being atmospheric, fast, and catalyst-free for the production of nanoparticles. Single-crystalline ZnO nanowires were grown directly on zinc-plated substrates without the use of catalysts under atmospheric conditions (Xu et al., 2007). Similarly, iron oxide nanorods were produced in an opposed-flow flame under atmospheric conditions (Merchan-Merchan et al., 2008). Flame-synthesized titanium dioxide has the advantage of being atmospheric, catalyst-free, rapid, mild, and scalable when compared to its current production method by chemical vapor deposition (Rao et al., 2011).

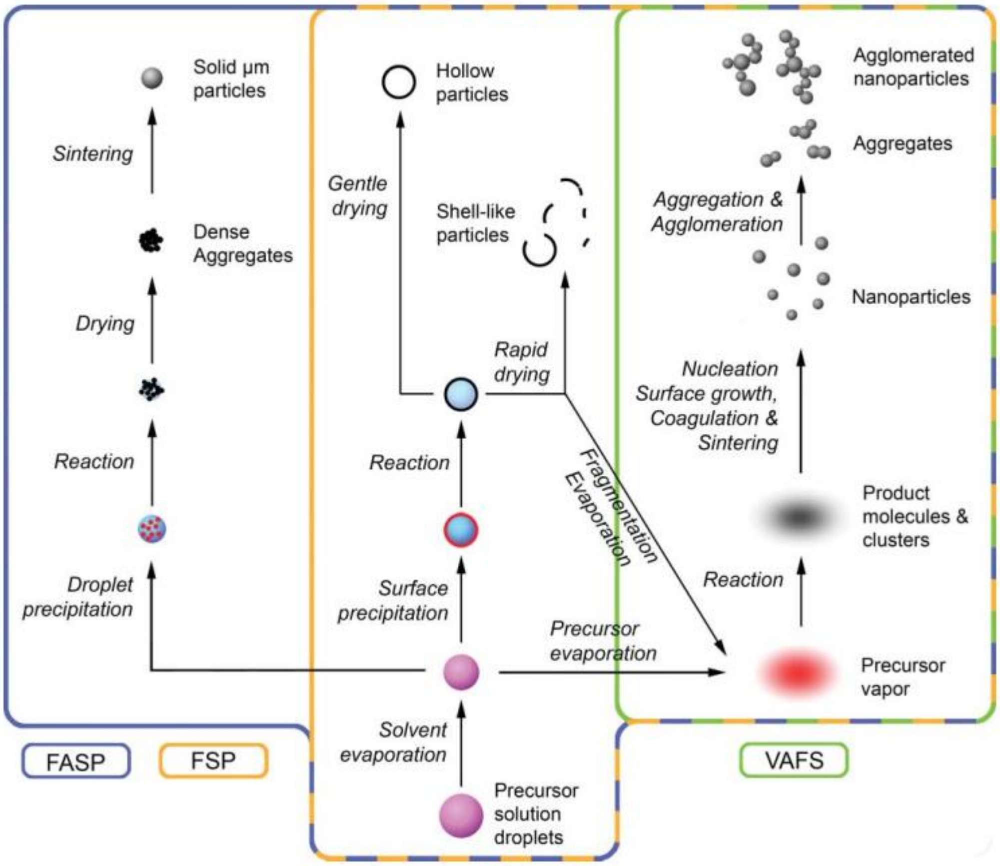

Figure 1.3. Schematics for particle formation mechanism during flame-assisted spray pyrolysis (FASP), flame spray pyrolysis (FSP), and vapor-fed aerosol flame synthesis (VAFS) (Hardesty et al., 1973).

1.2.2 Parameters affecting flame synthesis

There is a need to control the size and distribution of the particle, and crystallinity, as it affects its applications in catalysis, electro-optical devices, and semiconductors. Recent trends predict the need for finer control in the structure especially the size of the particles being produced (Granqvist et al., 1976). Combustion synthesis is mainly carried out in hydrocarbon flames as it offers high temperature and ease of use. The main hurdle is the production of soot which is avoided by using a low equivalence ratio (Kumfer et al., 2023).

Flame generated nanoparticles are generally aggregates or agglomerates of primary particles. Aggregates are used in reinforcing, catalysis, and porous film applications. The important parameters used to control the characteristics of the particles are gas mixing (equivalence ratio), precursor concentration, charging, residence time, and flame temperature (Pratsinis, 1998).

Primary particle residence time has a noticeable effect on the size of the nuclei. Shorter residence times and faster cooling reduce primary particle size and extent of aggregation. Quenching the downstream flow using a quench ring reduced the residence time and increased the cooling rate of the produced Pt particles which reduced in size by up to 30% (Schulz et al., 2005). The specific surface area increased by a factor of 3 from 20 m^2/g to 60 m^2/g by quenching (Hansen et al., 2001). Precisely controlled TiO_2 particles within the range of 5 nm to 60 nm were produced by forced quenching to reduce residence time (Wegner et al., 2003).

Electric fields or laser irradiation also contribute to the control of product properties. Electric fields in the form of gaseous corona were used to reduce the residence time of the particles in the flame, thereby reducing the size of the primary particle. Increasing the potential from 5 to 8 kV reduced the particle size by 50 % (Vemury et al., 1995). Charging especially has found importance as it is shown to effectively narrow down the size distribution of particles.

1.2.3 Ionization in flames

Studies have shown the generation of ions and electrons in hydrocarbon flames (Fig. 1.4). The two main ionization mechanisms are chemi-ionization and thermal ionization (Calcote, 1957).

Chemi-ionization occurs at the flame front where the chemical reactions provide the energy for ionization. This mechanism is dominant at temperatures below 2000 K (Becker, 1970).

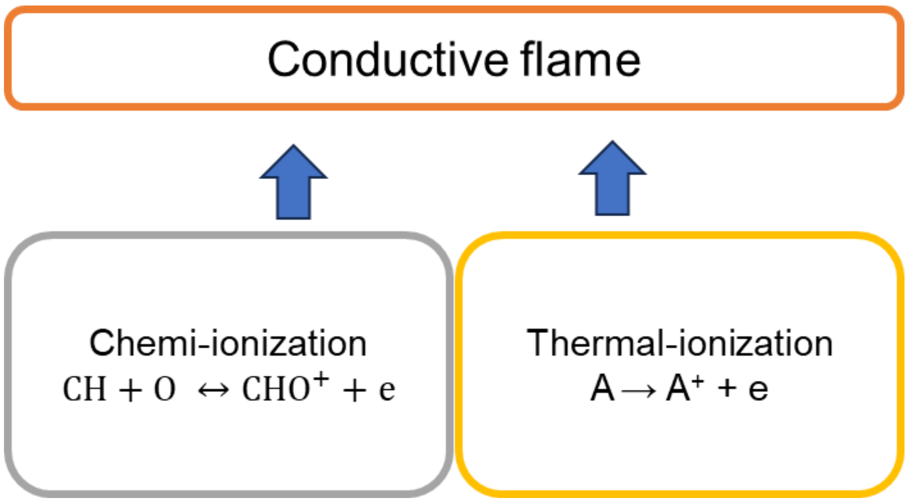

Figure 1.4. Flame ionization mechanism (Calcote, 1957).

Chemi-ionization is responsible for the formation of electrons in hydrocarbon flames due to the abundance of CH radicals (Calcote, 1961). From the reaction, CHO^+ reacts further to produce other ions such as H_3O^+, CH_5O^+, O_2^-, and OH^- (Goodings et al., 1979a, 1979b). The negative ions are generally unstable and break down into electrons and neutral particles (Altendorfner et al., 2010). Therefore, negative charge carriers are predominantly electrons. The location of ion production was studied. Most of the ion production was found to be at the reaction zone at normal flame temperatures. The only exception was at lower flame temperatures where the ion production shifted upstream of the reaction zone (Eraslan et al., 1988; Fialkov et al., 1985). With increasing equivalence ratio, the ion concentration increased to its peak near the stoichiometric ratio. The concentration then drops off as the equivalence ratio increases further (Brown et al., 1988). The concentration of the charged species depends upon the equivalence ratio, flow velocity, and inlet gas properties (Hartwell et al., 1951).

$$CH + O \Leftrightarrow CHO^+ \quad \text{(R1.1)}$$

The second ionization mechanism is through thermal ionization which was assumed to be the dominant ionization mechanism before the discovery of chemi-ionization (Calcote et al., 1955). Thermal ionization involves the interactions of high-energy radicals with the preexisting impurities in the flame to produce charged species (Semenov et al., 1970). Impurities in the reactants boost the rate of thermal ionization, thereby increasing the concentration of the charged species (Greene, 1963; Styrikovich et al., 1977). The factors affecting the rate of chemi-ionization were the reaction pathways, transport coefficients, new ionic compounds, and flame conditions (Fialkov, 1997).

Due to the two ionization mechanisms, the flame turns into a quasi-neutral ionized gas. The flame maintains its charge neutrality, and the concentration of negative ions and electrons is equal to that of positive ions (Garanin et al., 2008). Applying an electric field to the flame affects it in one of three ways (i) ionic wind effect, (ii) chemical effect, and, (iii) Joule heating effect (Yagodnikov et al., 1994). When an electrode is used to induce an electric field on the flame, the charged species move towards the electrode with the opposite polarity. The unidirectional movement of the charged species induces a velocity on the neutral species due to collisions. As positive ions are heavier, they have a significant effect on the bulk velocity resulting in the bulk flow towards the negatively charged electrode. The bulk movement of species towards the electrode is called ionic winds (Lawton et al., 1963). The bulk movement of charged species also causes a phenomenon called flame wrinkling, which alters the shape and size of the flame front (Marcum et al., 2005; Moses John Christy Appolo, 2021). The chemical effect influences the chemical reactions in the flames (Kim et al., 2012). The Joule heating effect was the heat generated by the electric current across the flame volume. This additional heat increases the flow temperature and reaction rates (Chen et al., 2016).

Due to the high concentration of charged species formed in the reaction zone, flames possess electrical characteristics (Park et al., 2016). When an electric field is applied across a flame volume, the migration of the charged species to their respective electrodes will create a current. As the electric field is raised, the flame current increases until it reaches saturation. The measured saturation current in a lean flame was used in a feedback loop to control the equivalence ratio of the flame (Speelman et al., 2015; Speelman et al., 2015). Further increase in voltage will result in an exponential increase in current due to breakdown (Ren et al., 2018). The voltage-current characteristics (VCC) or flame electrical characteristics have been studied extensively based on different types of flames. Flame properties were diagnosed based on the electric current across them (Han et al., 2017). This technique was used in the internal combustion engine and other flame-sensing technologies.

1.2.4 Flame synthesized particle charging

Alkali and alkaline-earth metals were added to the reactants to suppress the formation of soot particles. In the presence of these additives, the particles were charged and repelled each other preventing their growth (Haynes et al., 1979). Charging particles either through the addition of ionizing alkali salt solutions or by imposing an electric field affects the flame-generated particle morphology and characteristics (Wu et al, 1993). A phase change of TiO_2 from rutile to anatase was observed when $AlCl_3$ and $SiCl_4$ were used as additives. The addition of these metal salts also resulted in the reduction of size (Akhtar et al., 1994). The ions and charged species actively collide with the produced particles and induce an electrostatic potential through diffusion charging (Jiang et al., 2007).

Flame-synthesized particles in flames are electrically polarized due to the deposition of charged species produced due to ionization in flames. As a result, the charge distribution of the flame-generated particles is altered, affecting the growth of the particles (Friedlander, 2000). The effect on the properties is further enhanced by manipulating the ion environments Low-frequency AC electric fields were found to change the shape and structure of the flames by manipulating the flame-produced ions. This could be used to manipulate the residence time and temperature profiles a flame-synthesized particle will flow through (Ren et al., 2017). Similarly, studies have shown to change the size of TiO_2 nanoparticles by utilizing the dipole-dipole forces (Zhang et al., 2011). Charging is enhanced by the application of electric fields across the flame volume. Three common electrode configurations used for the application of electric fields are needle-to-needle, needle-to-plate, and two parallel plates. Needle electrodes create highly focused electric fields resulting in the onset of ionic winds. Particle motion and particle trajectories were significantly changed under the influence of electric fields (Bradley et al., 1984). The characteristic velocity of negative ions varies between 10 to 200 m/s for 1 V/cm. This suggested that the negative ions were mainly composed of electrons and therefore were lighter than the positive ions. The needle electrodes placed perpendicular to the flow axis resulted in ionic winds that reduced the flame height, flame temperature, and residence time of the particles. The combined effect resulted in the production of smaller particle nuclei. As the needle electrodes were swapped for the plate electrode, no ionic wind was observed. Electrostatic effects resulted in the repulsion of similarly charged particles, which significantly contributed to particle size reduction. The electrostatic repulsion prevents the formation of aggregates and was used to manipulate the residence time of the flame-produced particles (Schmidt et al, 2013). Multiple studies have shown the increase in specific surface area or the reduction of primary particle size with the use of electric fields on flame-generated particles. Applying an electric field of 6 kV to a counter flow methane/air diffusion flame containing silica precursors resulted in the reduction of particle size by three orders of magnitude. This was attributed to the reduction in residence time in the flame.

Unipolar charging of particles has been shown to reduce coagulation rates and particle growth when compared to bipolar charging (Adachi et al., 1985). This is due to the repulsion of similarly charged particles. Studies have shown that negative electric fields are more effective in varying the particle's characteristics. This is attributed to the more efficient charging of the flame-generated particles by negative charge carriers. Owing to their high mobility, were more potent in charging through collision than positive ions (Hinds, 1982; Wiedensohler, 1988). In the current study, the effects of electric fields on gas-phase flame-generated particles are utilized to control their continuous coating of a semipermeable solid substrate.

1.3 Motivation

Gas phase synthesis of silica nanoparticles under the influence of electric fields noted the ability of electric fields to manipulate the particle characteristics (Hardesty et al., 1973). Gas phase synthesis of silica nanoparticles under the influence of both unipolar and bipolar DC electric fields was conducted (Strobel et al., 2006). The presence of flame-synthesized particles reduced the measured current. Prior studies related to VCC in particle-laden flames are limited (Vemury et al., 1997). Mesoporous nanostructured titanium-dioxide was produced using a stagnation swirl flame under the influence of an electric field. The application of an electric field reduced the average diameter of the particles (Xiong et al., 2017). Carbon nanotubes were grown in a counter-flow flame under the influence of an electric field. A catalytic probe was used as a solid support for the growth of the nanotubes (Merchan-Merchan et al., 2004). The alignment and growth rate of carbon nanotubes on a probe with voltage bias were observed. Both polarities enhanced the growth rate of carbon nanotubes (Xu, Zhao, & Tse, 2007).

Silica nanoparticles find application in a wide variety of categories. Silica particles find importance in the optical fiber, fumed silica, drug delivery, and catalyst industries (Bautista & Atkins, 1991). Owing to its controllable particle size, larger surface area, and great biocompatibility, silica has been used in the drug delivery, enzyme encapsulation, therapeutics, and bio-imaging fields (Huang et al., 2022; Liu et al., 2018). Porous silica nanoparticles have been extensively researched as a drug delivery medium in the treatment of lung cancer , and liver cancer (Tüncel et al., 2021) and ocular disease (Rodrigues et al., 2020). Silica is used in the electronics and microelectronics industry (Laskowski et al., 2019), supercapacitors (Aiping et al, 2013), and battery electrodes (Chadha et al., 2022). The low-k dielectrics value ($k<3$) of silica makes it crucial in the integrated circuits industry. Due to the varied uses of Silica nanoparticles, it was the primary focus for the study and development of the new process in flame synthesis.

There are very few studies following the effects of flame-generated particles on the VCC of a flame. In the present work, the gas phase production and growth of silica nanoparticles and its subsequent direct coating on a solid substrate controlled by the application of an electric field are studied.

1.4 Thesis Objectives

The objectives for the current study are:

- Perform experimental studies on flame synthesis of silica nanoparticles in a well-defined 1-D flat flame and uniform external electric field configuration.
- Study the effect of flame-synthesized particles on voltage-current characteristics of the flames (VCC) and the effect of particle build up on the VCC in seeded and unseeded flames.

- Study the effect of an external electric field on particle yield and collection efficiency on solid supports.
- Produce an experimental database on particle size distribution generated at various electric fields using scanning and transmission electron microscopy.
- Perform laser imaging to relate collection efficiency with particle concentrations upstream and downstream of the collecting electrode.
- Perform numerical modeling to study the profiles of charged species in seeded and unseeded flames.
- Examine the correlation between the observed VCC, collection efficiency, and the thickness of the deposited material layer. The correlation can be used to enhance the deposition of gas-phase synthesized particles on solid supports.

Chapter 2 describes the schematic of the experimental setup used during the study. Chapter 3 explains in detail the voltage-current characteristics of seeded and unseeded premixed burner stabilized flat flames and the effect of particle coating on the measured flame current. Chapter 4 describes the yield of the particles that is calculated from the weight measured at various electric potentials and deposition times. Chapter 5 explains the particle characterization under electron microscopy and a description of the particle size and size distribution. Chapter 6 visualizes the particle flow downstream of the flame by illuminating the test section using a laser. Chapter 7 considers s a detailed 1D flame model to understand the interactions between neutral and charged species in the flame. Followed by the summary of the results in Chapter 8.

Chapter 2: Experimental Setup

An experimental study on the formation of silica nanoparticles is performed. Figure 2.1 shows a schematic of the experimental setup. A flat flame burner forms the core of the setup. The burner is supplied with a premixed mixture of fuel, air, and precursor through the gas supply system. A semi-permeable wire mesh connected to the DC power supply acts as the electrode while the burner is grounded through a 1 MΩ non-inductive resistor.

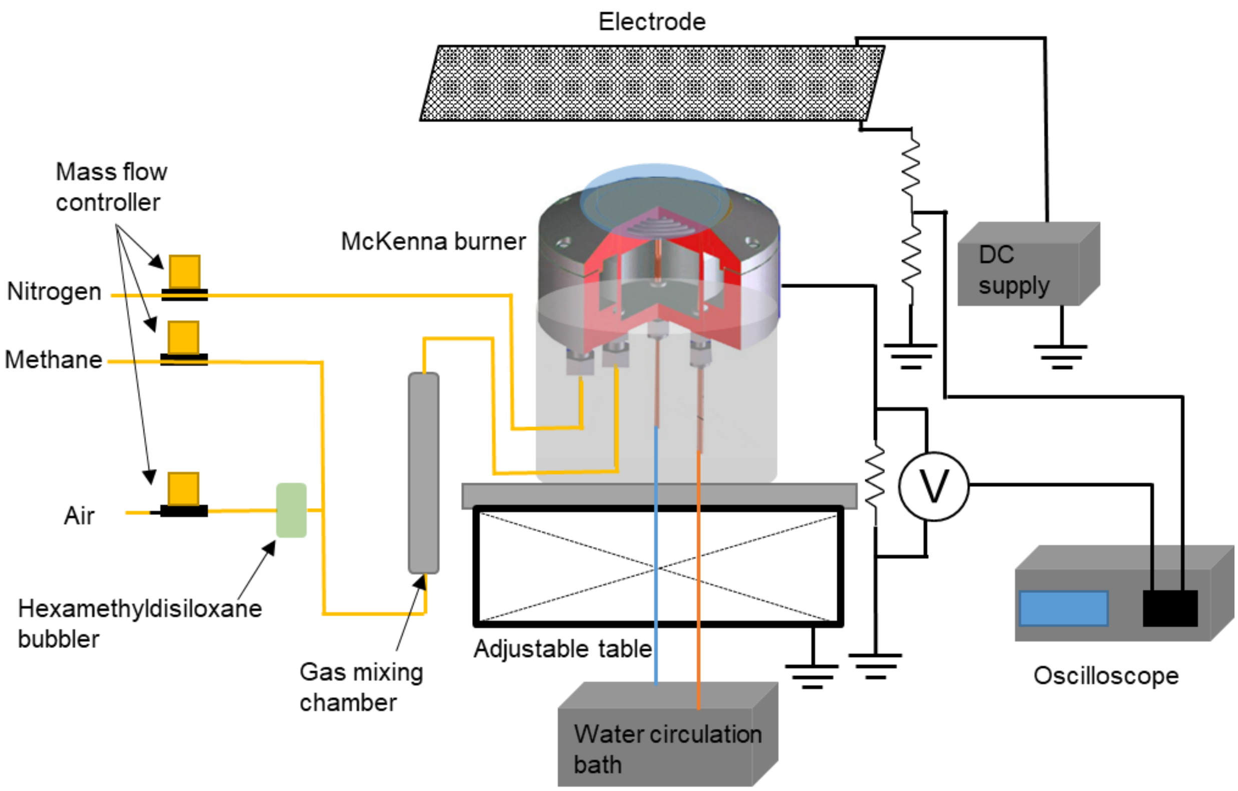

Figure 2.1. Schematic of the experimental setup

2.1 McKenna burner assembly

In the current study, a McKenna burner is used as it produces a 1-dimensional flat luminous flame. The flame provides a 1-D flat reaction front and radially uniform temperature and velocity distributions to ensure a majority of the particles experience similar synthesis conditions (Sutton et al., 2006; Vijayakumar et al., 1984). Flat flames make it simpler to develop and validate one-dimensional flame models (Speelman et al., 2015).

Figure 2.2 shows a cross-section of the McKenna burner. It consists of a sintered bronze core (6 cm diameter) with an inbuilt cooling circuit to prevent flashbacks. A water-cooling bath is used to regulate the burner temperature. A coaxial sintered bronze shroud is placed around the main porous plug. The premixed fuel/air mixture flows through the gas inlet into the chamber below the porous plug.

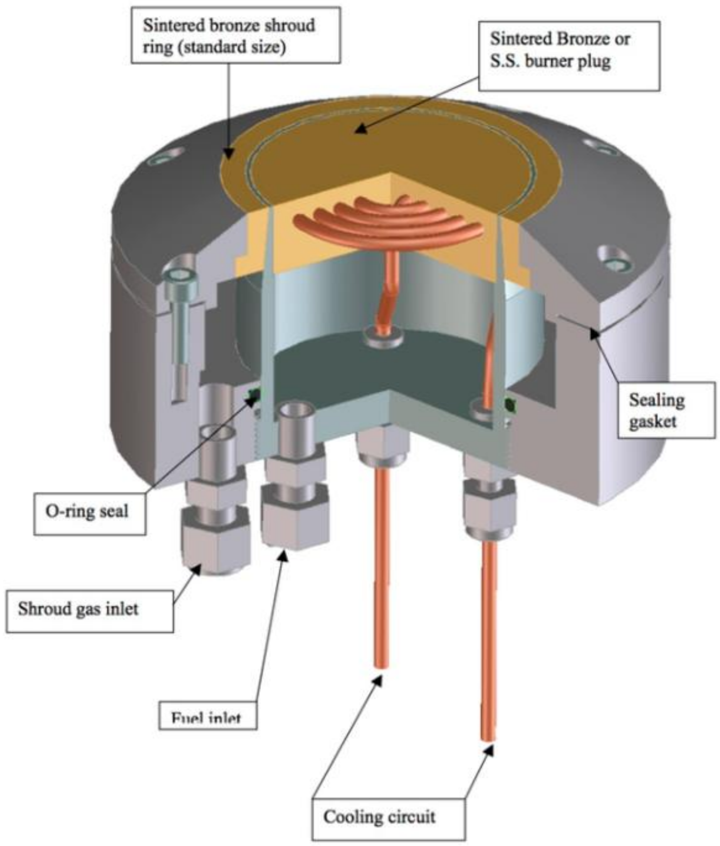

Figure 2.2. Cross-section view of the McKenna flat flame burner with the cooling circuit (Holthuis and Associates Flat Flame Burner, 2023).

2.2 Premixed gas supply system

The fuel used for the experiments is high-purity methane, supplied from compressed gas cylinders. The air is supplied from an in-house compressor system. The pressures in the fuel and air lines are regulated using pressure regulators. The flow rate for each gas is controlled using

MKS mass flow controllers (MFC). MKS 1179A with a 5 SLM rating. An MKS GE50A with a 20 SLM rating is used for supplying methane and air respectively. The MFCs are connected to MKS 247D power-supply/readout. A LabVIEW graphical program is setup for controlling the MFCs through the MKS 247D. The flow rates are adjusted to achieve equivalence ratios ranging from 0.7 to 0.9 and a cold velocity between 7 and 9 cm/s. A mixing chamber filled with 6mm alumina pellets is used downstream of the MFCs to obtain a premixed reaction mixture. Swagelok ball valves are used to control the flow of gases to the MFCs as an added layer of safety.

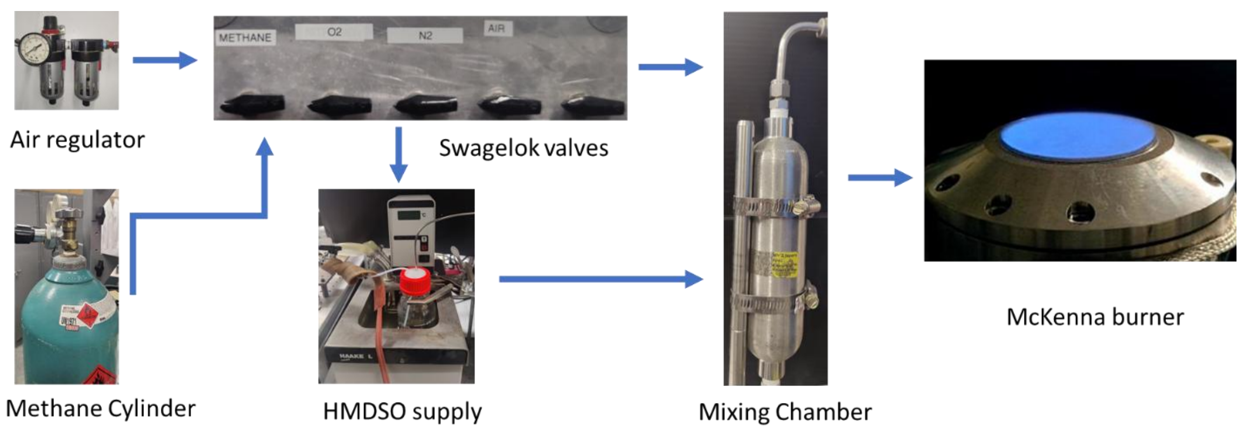

Figure 2.3. Gas supply system flow diagram.

The MKS MFCs were controlled using high-speed data acquisition and control (cDAQ9172). The control system involves multiple analog and digital, input and output modules that communicate with the LabVIEW user interface through the National Instruments data acquisition chassis. Figure 2.4 shows the electrical connections of the DAQ and the pin diagram of the MKS 247 MFC controller. The digital output module NI 9474 is used to switch the MFC on or off. The flow rates are set using a 0 to 5 V signal from the NI 9263; a signal of 0 V corresponds to no flow, and a 5 V signal corresponds to the MFC’s maximum flow. Depending on the actual flow rate each MFC communicates a signal of 0 to 5 V to the analog input module NI 9201. The actual flow information is used to calibrate the MFC.

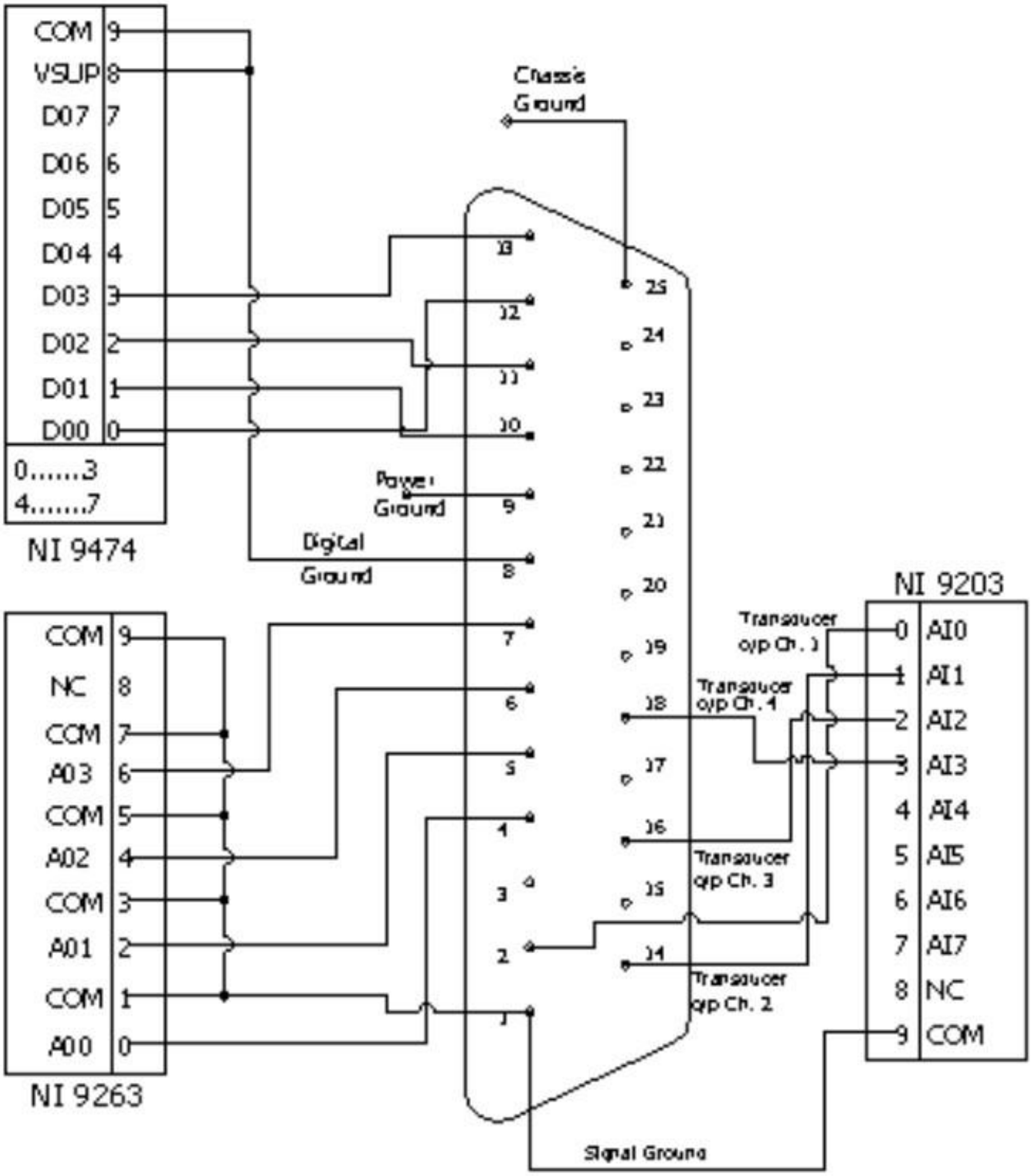

Figure 2.4. MKS 247D controller pin diagram and NI DAQ wire connections.

2.3 Precursor supply

A precursor is a substance that is added to the reaction mixture and combusted to produce a desired material. In the current study hexamethyldisiloxane (HMDSO – $C_6H_{18}Si_2$) is used as the precursor as it produces silica particles. The breakdown mechanism of HMDSO in a methane-air flame is well-understood (Chrystie et al., 2019; Feroughi et al., 2017; Yeh et al., 2001a). Research examining the impact of external electric fields on SiO_2 production from HMDSO offers valuable insights (Kammler et al., 2000). Figure 2.5 shows the bubbler used to mix the precursor vapor with the reaction mixture. Air metered through a MFC is used as the carrier gas flows into the mixing chamber and combines with the reaction gases. An MKS 1179 MFC is used to meter 50 - 150 SCCM of air to produce a mass flow rate range of 0.03 to 0.09 g/min. The bubbler is placed in a water heating bath (Haake L water bath) to maintain the precursor temperature at 50^o C, producing a vapor pressure of 9.72 kPa. To prevent the condensation of HMDSO within the supply lines, tape heaters (Omega, Inc) are wrapped around the high-pressure tubing connecting the bubbler to the mixing chamber.

2.4 Electrical supply and measurement system

Prior research related to the electrical characteristics of premixed 1-D flames provides a basis for the present study (Moses John Christy Appolo, 2021.). A wire mesh placed 35 mm above and parallel to the burner surface is used as the electrode. The burner is constantly grounded. A DC generator (Model FC, Glassman High Voltage Inc.) with a power rating of 120 W (30 kV and 4 mA) is used. The polarity of the applied electric field is changed by switching the polarity of the power supply. A multimeter is connected to the internal circuit of the DC generator to measure the flame current with a resolution of 1 µA. The 1-D nature of the flame allows for the application of a radially uniform electric field that is normal to the reaction front and parallel to the flow direction.

A resistor is connected between the burner and the ground. The current is measured across a 1 MΩ non-inductive resistor, connected to the burner at one end and grounded on the other end.

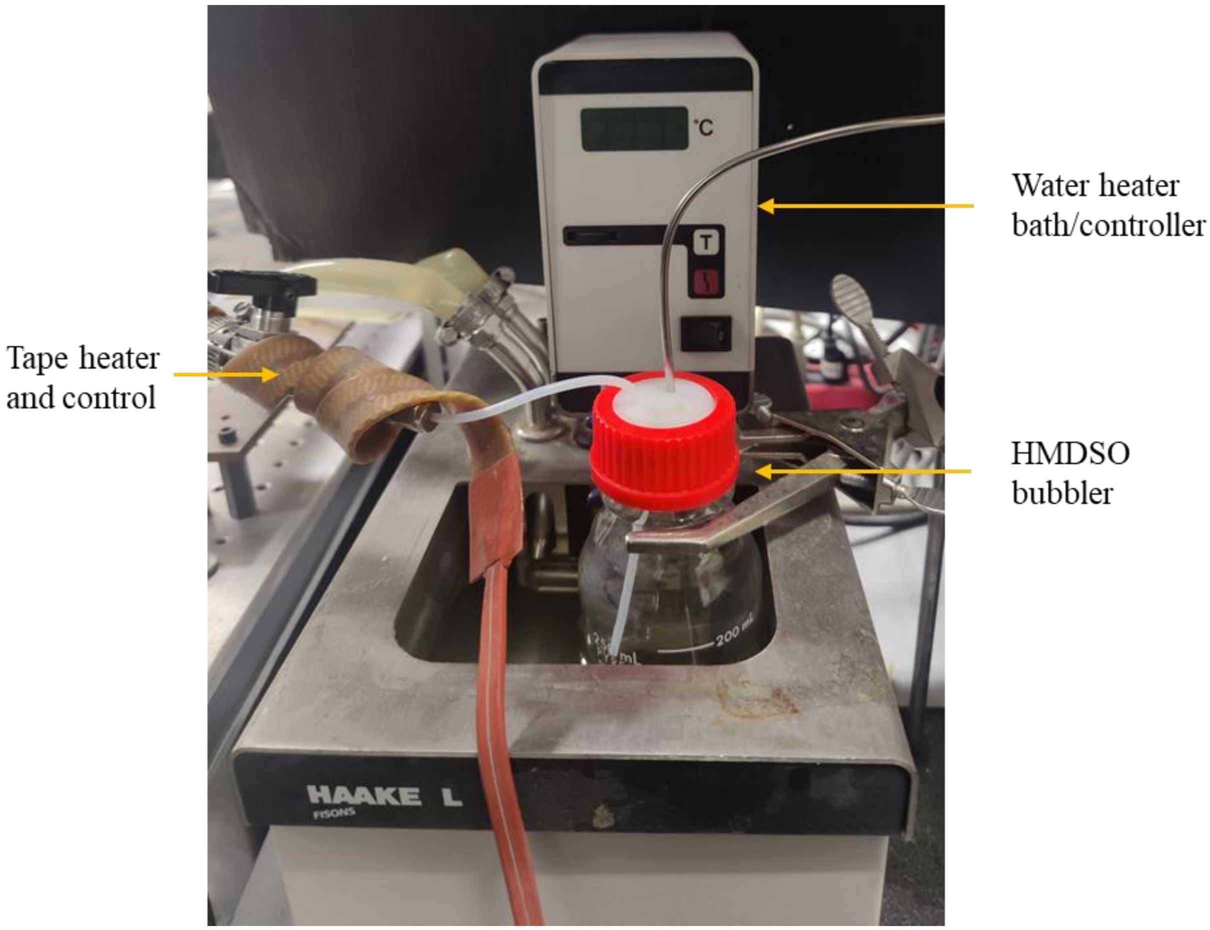

Figure 2.5. Precursor supply system.

2.5 High-resolution imaging setup

A Photonics Industries DM30-527 dual head high pulse energy Nd: YLF Laser is used to illuminate the particles downstream of the flame. Collimating and diverging lenses are placed in line with the laser beam to obtain a laser sheet above the burner. The laser sheet illuminates a region extending from the burner surface to ~ 25 mm above the electrode, as shown in Figure 2.6.

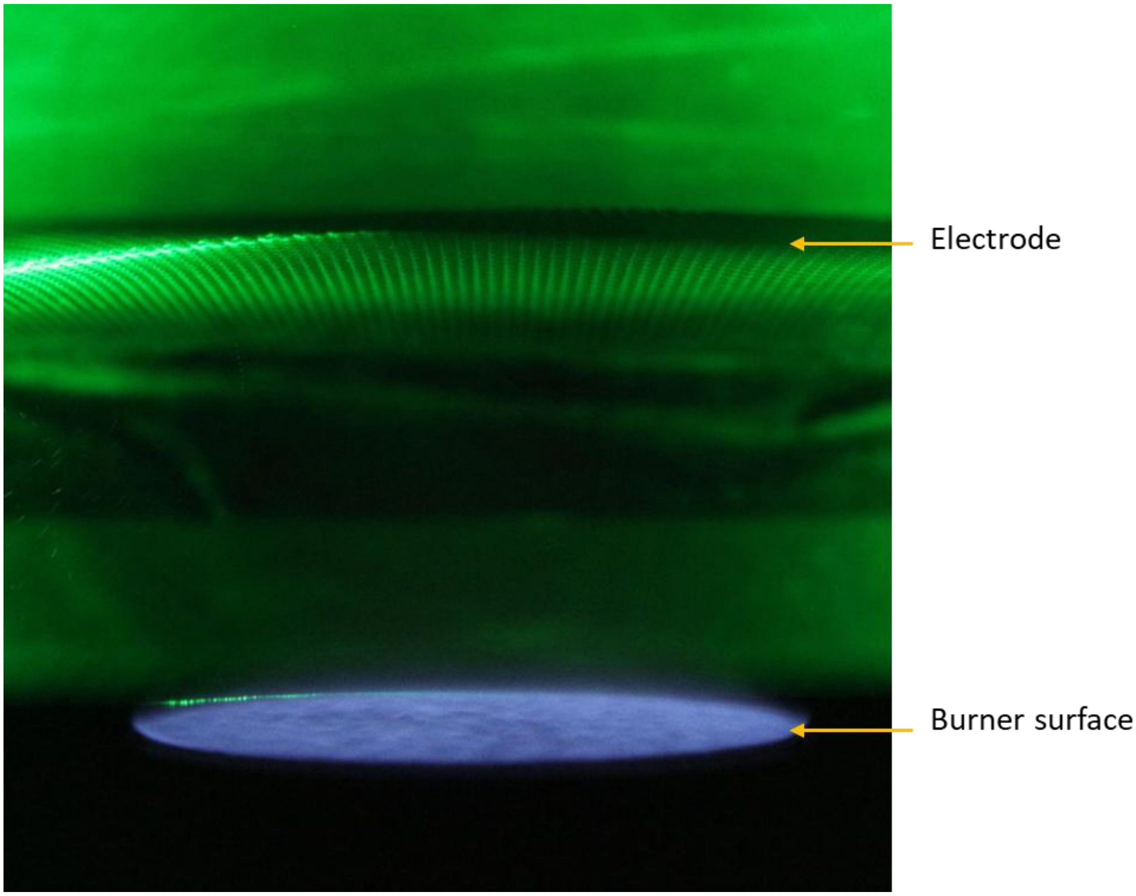

Figure 2.6. Test section: region from the burner surface to an inch above the electrode illuminated by the green laser.

A Canon EOS 90D camera measures the scattering intensity (arbitrary units) to study the effect of electric field strength on the concentration of particles. An EF-S 18-55 mm f/3.5-5.6 lens is employed to manually focus the test section. Andover Corporation 532 FSX10-50 532nm wavelength filter is utilized to capture the green laser light. A shutter speed of 1/30, ISO 3200, and F 5.6 are kept constant. The images are captured at 30 frames per second. The captured images are processed using MATLAB and ImageJ to measure the scattering intensity.

Chapter 3: Voltage-Current Characteristics of Premixed Flat Flame

Combustion of hydrocarbons creates positive and negative charge carriers through chemi-ionization (Calcote, 1957). The interaction between the flame and an external electric field was first observed in 1814 (Brande, 1814). A detailed review summarized the effect of DC and AC electric fields on flames of various configurations and fuel-oxidizer mixtures through experiments and models (Fialkov, 1997). Flame properties such as flame speed, flame stability, and soot production were altered. Experimental studies on the alteration of flame height, and, stability of a methane-air premixed flame using a cylindrical metallic burner under the influence of DC electric fields were performed (Vinogradov et al., 2001). The ionic wind, a body force generated by the movement of charged particles under the influence of electric fields, was believed to be the primary factor behind the variation in flame characteristics (Marcum et al., 2005). Ionization and subsequent recombination of ions in the flame reaction zone were proposed as an alternative mechanism for the flame interaction with DC electric fields (Wisman et al., 2008) along with the Coulomb force (Starikowskii et al., 2008).

Many studies have been conducted to observe and explain the interaction between flames and external electric fields. The interaction between a particle-laden flame and a DC electric field was seldom studied (Vemury et al., 1997). In the current study, experiments are conducted to observe the interactions of a flame with and without flame-synthesized particles under an external electric field. The VCC for pristine flames is measured by using the multimeter connected to the internal circuit of the DC power supply. The DC voltage is increased, and the corresponding current is measured. The procedure is repeated for both the positive and negative polarity of the DC power supply. The VCC corresponding to the change in equivalence ratio and velocity is measured. To obtain the VCC of the particle-laden flame, the precursor is introduced into the reaction mixture, and the same measurement procedure is followed.

3.1 Premixed flat flame

The Voltage-Current Characteristics (VCC) provides information regarding the current drawn from the flames due to the presence of ions under the influence of an electric field. Chemi-ionization is believed to be dominant in the formation of ions (Duan et al., 2015). VCC is measured for a burner-stabilized flame under the influence of an external electric field (Figure 3.1).

Figure 3.1. Burner stabilized methane-air premixed flat flame under the influence of an external electric field.

Figure 3.2 shows the VCC measured for pristine flames. When 0 kV is applied to the electrode the positive and negative charge carriers present in the flame front through chemi-ionization undergo recombination and there is zero net movement. As a positive DC potential is applied, the negative charge carriers are pulled towards the electrode. The motion of negative charge carriers prevents the recombination of charge carriers in the flame volume. The negative charge carriers along with the burnt gases flow downstream and reach the positive electrode.

Conversely, the positive charge carriers move in the opposite direction, i.e. upstream, through the premixed reaction mixture towards the grounded burner. The motion of the charge carriers towards their respective electrodes results in the current. As the voltage applied to the electrode is increased the measured flame current correspondingly increases. As the polarity of the applied potential is reversed, the negative charge carriers now move toward the burner and the positive charge carriers toward the negatively charged electrode. The movement of charge carriers through the flame volume, driven by the applied electric field, generates a space charge with a polarity opposite to that of the electrode.

Figure 3.2 shows the effect of the electrode polarity and voltage magnitude on the flame current. Three distinct regions are observed in the VCC plots: (i) sub-saturation region, (ii) saturation region, and (iii) super-saturation region. The sub-saturation region is also called the recombination region, where the positive and negative charge carriers recombine to produce neutral species. Negative charge carriers decompose into electrons and neutral particles resulting in a partial diffusion of electrons. In the sub-saturation region, an increase in voltage results in a rise in flame current, which is qualitatively attributed to the ionic wind body forces. In the saturation region, the flame current is observed to be saturated showing no increase in current with further increase in voltage. This saturation is because all charge carriers are pulled away from the flame front due to the strength of the applied electric field. The third region is known as the super-saturation region. The super-saturation region entails an applied voltage larger than the breakthrough voltage. The breakthrough voltage creates excess charge carriers that are produced due to the collisions between the flame-generated accelerated positive and negative charge carriers and the neutral particles in the flame volume. Hence, the flame current increases exponentially with the increase in voltage.

The three regions of the VCC for pristine flames (Figure. 3.2) are corroborated with previous studies (Han et al., 2017; Moses John Christy Appolo, 2021). It is observed that the current saturates at a voltage of ~1 kV, and ~8 kV for the positive and negative polarity, respectively. The majority of the negative charge carriers are assumed to be electrons. The mobility of electrons is higher as they are lighter than positive ions. Due to the difference in mobilities, a much lower voltage is required to pull the electrons from the flame front. Compared to electrons the voltage required for all the positive charge carriers to reach the electrode is higher, owing to their higher mass and lower mobility. Thus, the current saturates rapidly when a positive polarity is applied to the electrode. Even though the saturation current is achieved at difference applied voltages for the positive and negative potential, their magnitude is the same regardless of electrode polarity for the flame conditions (Speelman et al., 2015a; Speelman et al., 2015b). This shows that the applied electric field potential does not affect the chemical kinetics of the reaction as a change in the rates of chemi-ionization is not observed. As the equivalence ratio and fuel concentration are increased there is a corresponding increase in the chemi-ionization rate. This results in higher values of the saturation current, with the voltage rising beyond 12~13 kV, a sharp increase in current occurs, indicative of the flame breakdown. The VCC obtained in the current study follows trends observed in other experimental studies (Han et al., 2017; Moses John Christy Appolo, 2021).

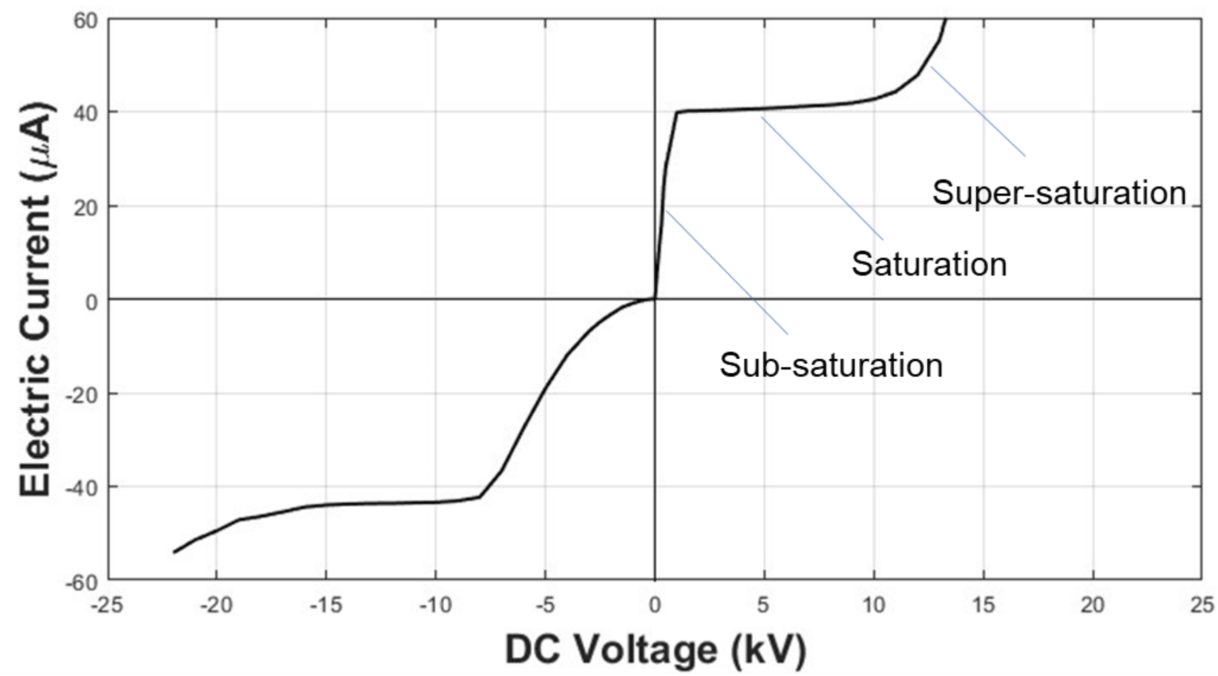

Figure 3.2. Voltage-Current Characteristics of a pristine flame at a constant velocity of 8 cm/s and φ=0.9, with the three saturation regions.

3.1.1 Effect of equivalence ratio and velocity on flame VCC

The VCC for a premixed burner stabilized flat flame is plotted in Figure 3.3 for different equivalence ratios at a constant velocity of 8 cm/s. It is observed that an increase in the equivalence ratio from 0.7 to 0.9 increased the saturation current. The increase in current is attributed to the increase in the rate of positive and negative charge carrier production due to the rise in the concentration of the radicals from the reaction mixture. Due to higher fuel and airflow rates, there is an increase in the concentration of chemi-ionized charge carriers.

Similar to the effect of the equivalence ratio, a change in reactive mixture flow velocity also affects the current (Figure 3.4). When the velocity of the mixture is increased the rate of chemi-ionization increases due to higher fuel and air flowrates. The increase in chemi-ionization rate results in the increase in new radical formation leading to higher concentrations of positive and negative charge carriers. The increase in charge carrier concentration results in a higher measured current.

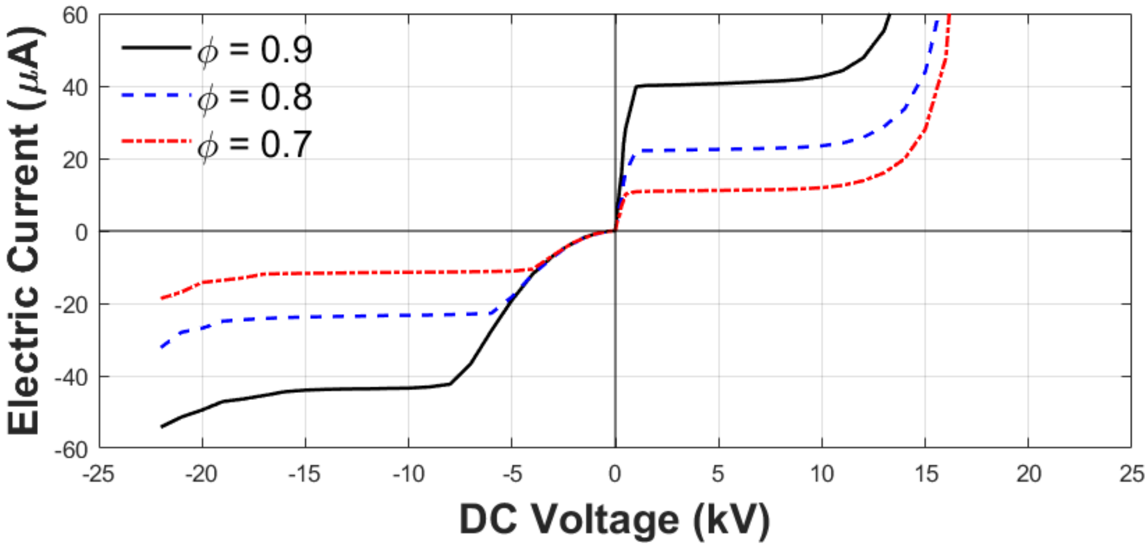

Figure 3.3. Voltage-Current Characteristics of an unseeded flame at a constant velocity of 8 cm/s with varying equivalence ratios.

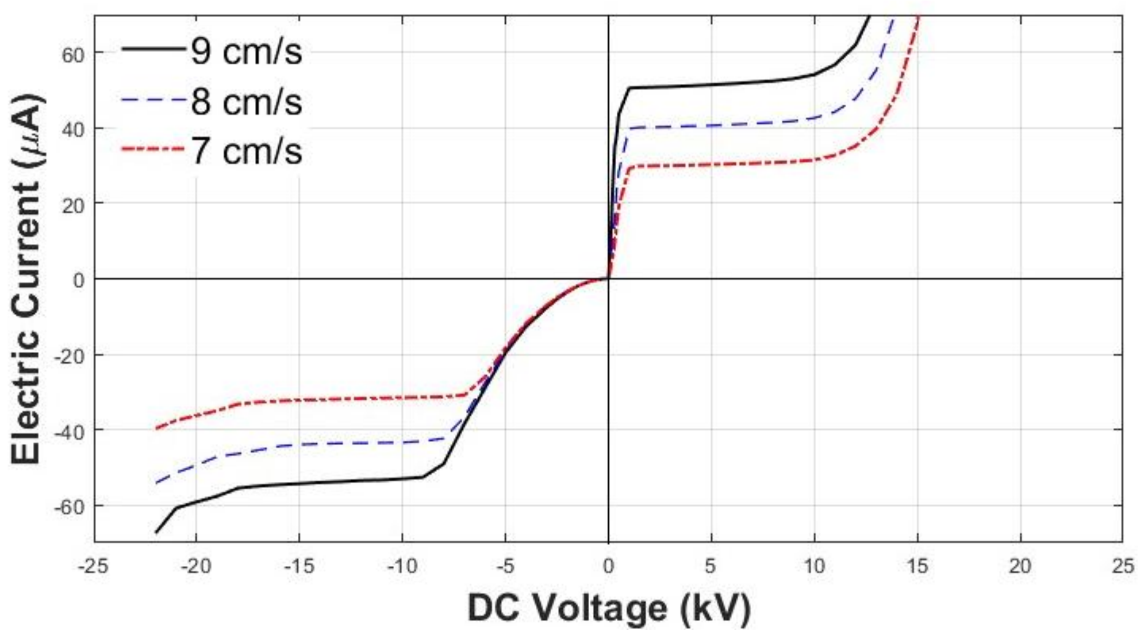

Figure 3.4. Voltage-Current Characteristics of an unseeded flame at a constant equivalence ratio of φ=0.9 with varying reactive mixture flow velocity.

Therefore, it was observed that both the equivalence ratio and flow velocity affect the rate of chemi-ionization, affecting the saturation current of the premixed burner-stabilized flat flame under the influence of a DC electric field.

3.2 VCC of particle-laden flame

The flame current or VCC of a seeded flame was shown to be lower when compared to that of an unseeded flame (Vemury, 1996). Electrode configurations such as needle-needle, plate-needle, and double plate were used to apply an external DC electric field. The electrodes were placed parallel to the flow of gases and perpendicular to the burner surface. Both unipolar and bipolar electric fields were applied. As the precursor was introduced into the flame, the measured currents were much lower compared to a pristine flame. The biggest variation was while using the double plate electrode configuration. It was hypothesized that the particles accumulate the charge carriers from the flame, and the number of ions available in the flame volume that reach the electrodes is reduced drastically. This effect was not observed while using the needle-needle electrode configuration. The charge carriers that were captured by the particles were replaced by the charges produced by the corona discharge. The particle-laden flame current was measured for both polarities, and the same trend was followed. The measured flame current was however lower by 10-15% for the positive electric field when compared to the negative electric field.

In the current study, the electrode is placed parallel to the burner's surface or perpendicular to the direction of the gas flow. A semi-permeable stainless steel wire mesh was used as the electrode. Due to the flame's one-dimensional nature, a radially uniform electric field is applied to the flame front. The procedure for measuring the VCC of the flame is repeated with the introduction of the precursor into the reaction mixture. Air is metered at a flow rate between 50 SCCM to 150 SCCM to achieve a precursor flow rate of 0.03 g/min to 0.09 g/min. The multimeter connected to the internal circuits of the DC power supply is used to measure the current at a sensitivity of 1 μA. The wire mesh electrode is charged either positively or negatively by employing the DC power supply connected to it. The burner is grounded through a 1 MΩ resistor.

Figure 3.5 (a) shows the difference in the trends between an unseeded and seeded flame at an equivalence ratio of $\varphi = 0.9$ and a reaction mixture velocity of v = 8 cm/s. As previously observed the measured flame current reduced by one order of magnitude for negative polarities. A similar reduction in the measured flame current is observed for the positive polarity; however, a monotonic growth followed by the saturation current is replaced by a complex pattern. The current initially increases to a local maximum of ~2 kV. At voltages above 2 kV, the current initially decreases and then starts increasing again until it reaches the super saturation region (~ 7 kV). As a negative polarity is applied to the electrode, the measured flame current decreases to zero. As the voltage is decreased below -8 kV the current increases exponentially. The voltage value corresponds to the voltage at which the measured current for pristine flames achieves saturation. The currents are lower by 10-15% for the negative polarity when compared to the positive polarity.

Figure 3.5 (b) shows the difference in the trends between an unseeded and seeded flame at an equivalence ratio of $\varphi = 0.8$ and a reaction mixture velocity of v = 8 cm/s. A similar trend is observed in Figure 3.5 (a). The change in equivalence ratio affects the measured flame current of the particle-laden flame in the same way as it did for pristine flames. The decrease in current is attributed to the reduction in the rate of positive and negative charge carrier production. Lower fuel and air flowrates lead to a decrease in the concentration of charge carriers resulting in a drop in the measured flame current.

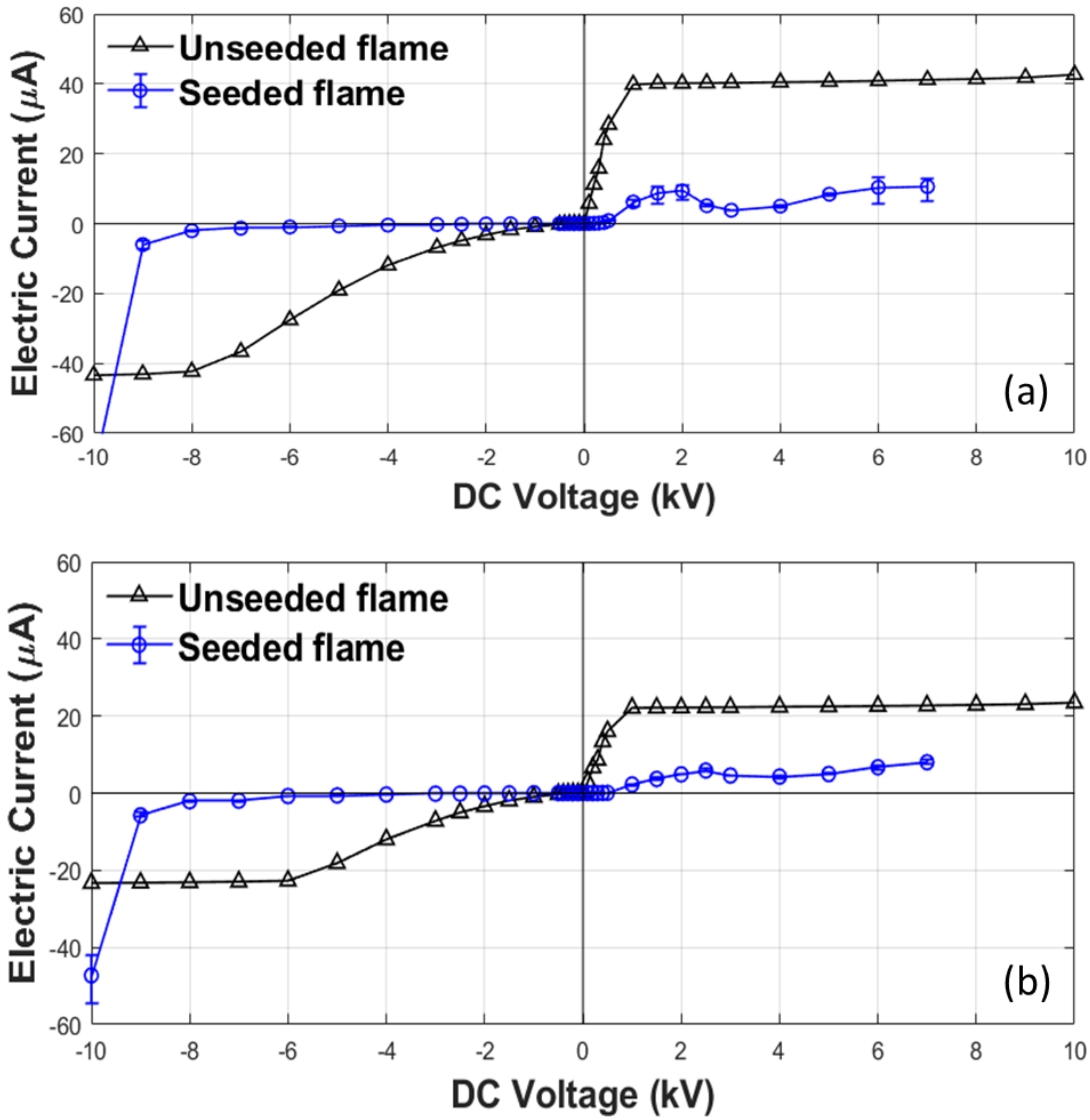

Figure 3.5. Comparison of unseeded and seeded flame VCC at constant velocity v=8cm/s for equivalence ratios (a) φ = 0.9, (b) φ = 0.8.

Figures 3.6 (a, b) show the VCC comparison between unseeded and seeded flame at a constant equivalence ratio of φ = 0.9 and velocities of 9 cm/s and 8 cm/s. The plots follow a similar trend to the plots shown in Figure 3.5. When the velocity of the premixed reactive mixture is decreased the rate of chemi-ionization decreases. The reduction in chemi-ionization rate results in lower concentrations of positive and negative charge carriers. This leads to the reduction in the measured flame current.

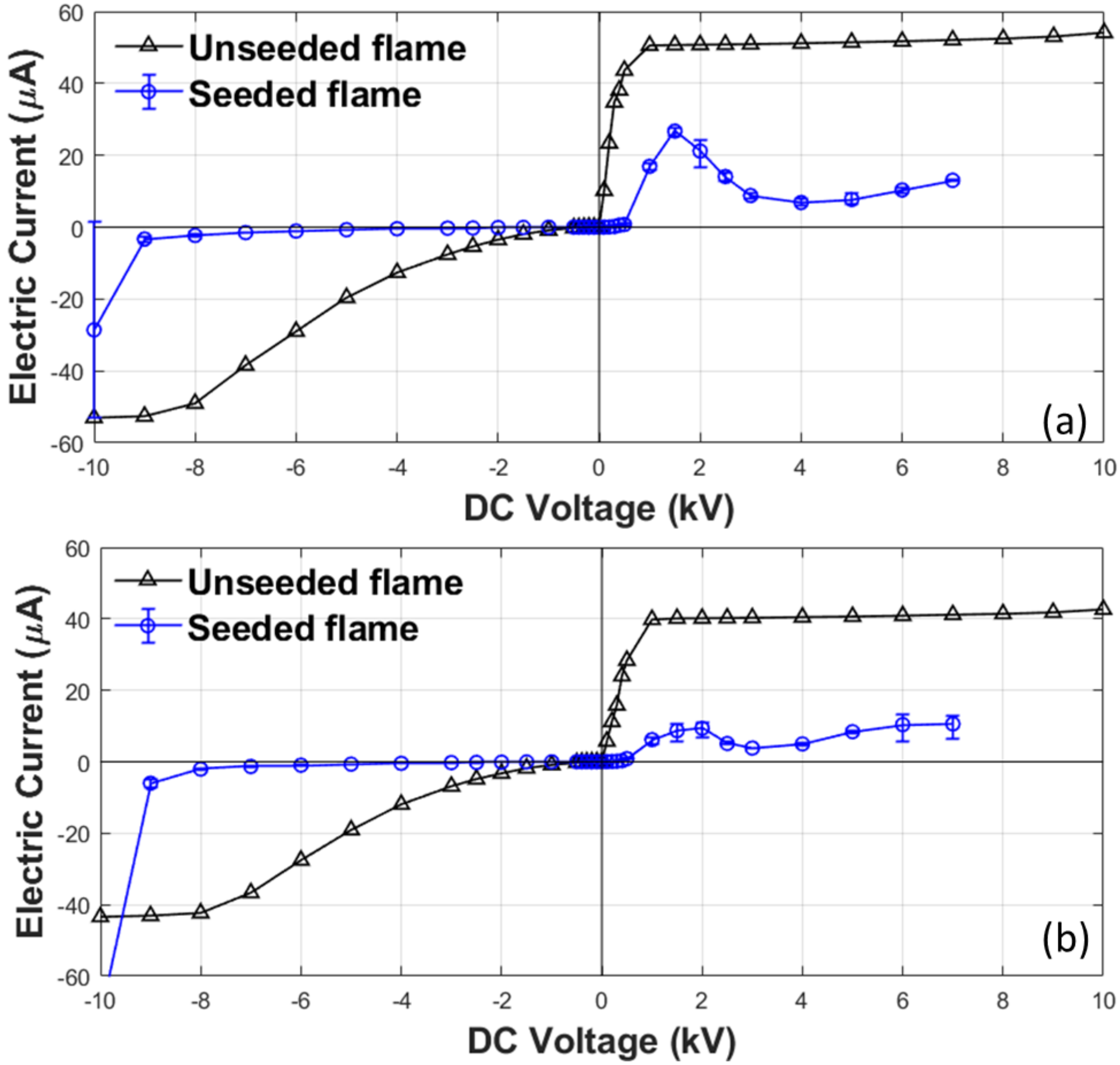

Figure 3.6. Comparison of unseeded and seeded flame VCC at constant equivalence ratio φ = 0.9 for velocities (a) v=9 cm/s, (b) v=8 cm/s.

Therefore, it was observed that both the equivalence ratio and flow velocity affect the rate of chemi-ionization, affecting the measured flame current of the particle-laden flame under the influence of a DC electric field.

3.3 Effect of particle build-up on the surface of the electrode

The introduction of the HMDSO into the flame through reaction gas mixing produces silica nanoparticles through combustion synthesis. The silica nanoparticles flow with the product gases and deposit on the surface of the electrode. The thickness of the silica nanoparticles coating on the electrode surface increases with time. Figures 3.7 and 3.8 show the effect of particle build-up on the surface of the electrode.

Figure 3.7 shows the time-resolved flame current measurement at an equivalence ratio $\varphi = 0.9$ and the reaction gas velocity of $v = 8$cm/s. The study initially started with the flame current measurement of a pristine flame in the presence of an uncoated electrode for 120 s. The precursor flow starts at 120 s into the run and continues till 780 s. The precursor flow is then shut off and the flame current of a pristine flame in the presence of a coated electrode is measured. The flame current was measured in 10-s intervals.

The experiment with positive polarity was conducted at a constant voltage of 3 kV. The flame parameters were kept constant throughout. The current remains nearly constant at 45 μA for the initial 120 s when there is no precursor flow. As the flow of precursor is initiated the current decreases sharply but increases to a local maximum 10 s later at 18 μA and remains constant for approximately ~50 s after which it decreases again. This local maximum is related to the high efficiency of particle collection on the uncoated electrode. The efficiency of collection reduces as the test runs for an extended time due to the build-up of a high-resistivity particle layer on the electrode. After 200 s, the current decreases steadily to zero. As the flow of precursor is stopped the current increases to slightly higher than pre-precursor flow values.

The experiment was repeated at negative polarity with the mesh electrode at – 3kV and the same flame conditions. Similar to the positive polarity, the flame current was constant before precursor introduction, however, a value of ~5 μA was recorded. As the flow of precursor was introduced, the current immediately dropped to near zero values. As the flow of precursor was stopped, the measured current values were doubled compared to pre-precursor measurements.

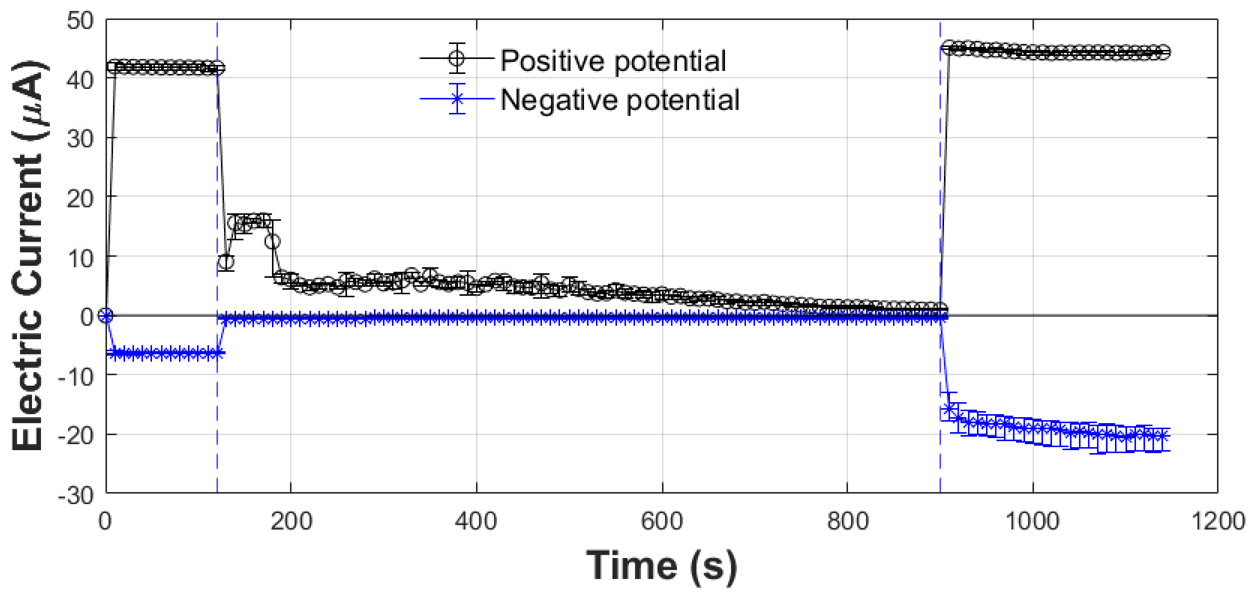

Figure 3.7. Time-resolved flame current measurement at φ = 0.9 and v = 8 cm/s at +3 kV and -3 kV for 1140 s.

Figure 3.8 shows the time-resolved flame current measurement for the same flame conditions in Figure 3.7, with a difference in deposition/coating times. The study had the same procedure with a precursor flow time of 180 s instead of 780 s. The flame current was measured in 10-s intervals. The trend followed by the second study resembled the first study. For the positive 3 kV test, there is a characteristic saturation of current for the first 120 s, followed by a sharp decrease. The flame current then increases due to the high collection efficiency of the clean electrode and subsequently reduces to approximately 10 μA. The current then slowly decreases to zero. As the precursor flow is terminated the current increases to a value higher than the pristine flame current under an uncoated electrode. The measured current in the negative polarity followed the same trend as the 1140 s test. It was observed that the measured flame current for the pristine flame under a coated electrode for the 420 seconds case is lower than the 1140 s test. This is a result of the thickness of the silica nanoparticle layer on the electrode surface.

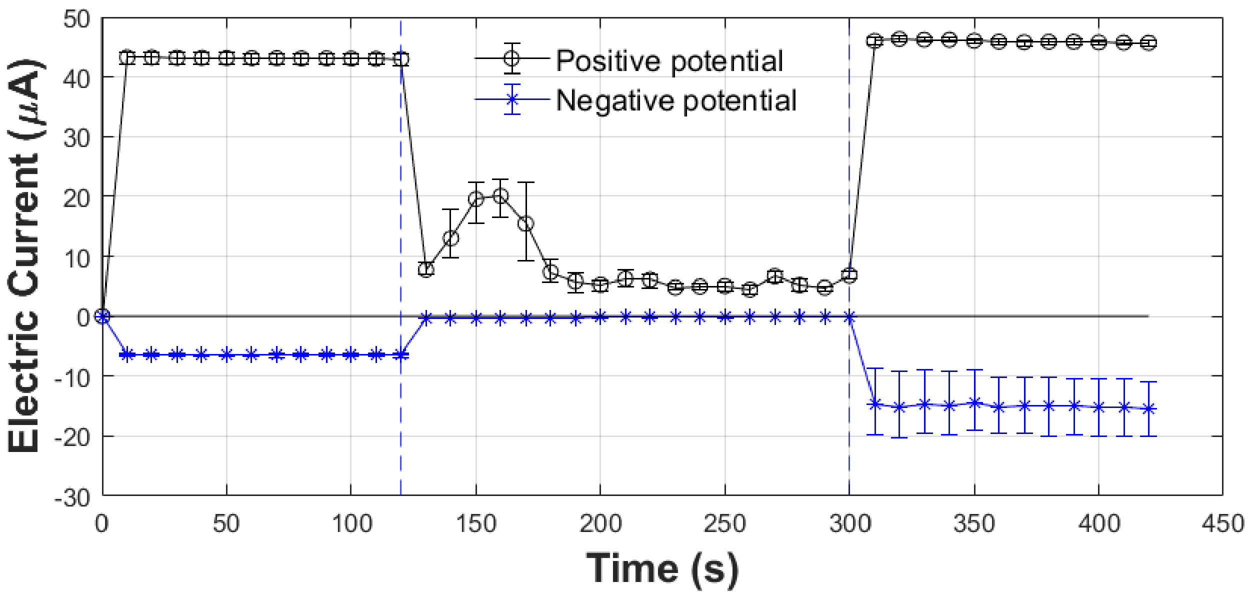

Figure 3.8. Time-resolved flame current measurement at φ = 0.9 and v = 8 cm/s at +3 kV and -3 kV for 420 s.

The particles moving downstream of the flame deposit on the electrode's surface. This results in the formation of a high-resistivity layer on the surface of the electrode. The further build-up of particles holding charge carriers on the surface results in an increased voltage drop across the layer. This voltage drop reduces the electric field in the flame volume resulting in the lowering of flame current. As the voltage drop within the particle layer increases, local breakdown occurs at multiple sites forming positive and negative charges near the electrode surface as shown in Figure 3.9. For positive polarity, the electrons travel to the electrode through the layer and the ions move towards the burner. These additional charges increase the current by ~3 μA. The presence of excess charges causes the breakdown between the electrode and burner. Conversely, with a negative voltage, electrons traverse the space between the electrode and burner initiating secondary ionization by an electron impact. This causes the current to increase exponentially, as shown in

Figures 3.5 and 3.6. The mechanism of breakdown in the particle layer is similar to the back corona discharge occurring when high-resistivity particles are captured using electrostatic precipitators (Mizuno, 2000).

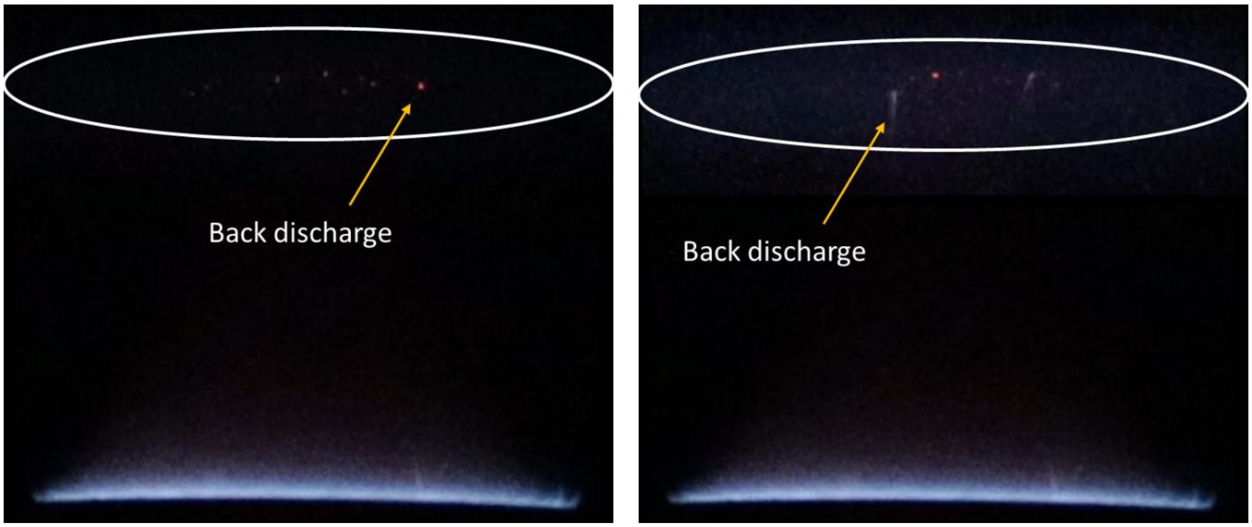

Figure 3.9. Local breakdown at the high-resistivity particle layer on the electrode surface at φ = 0.9 and v = 8 cm/s (a) -8 kV, (b) +5 kV.

3.3.1 VCC of pristine flame in the presence of a coated electrode

The VCC is measured for pristine flames in the presence of coated electrodes to understand the effect of the particle layer on the flame current. Figure 3.10 shows the effect of the particle layer on the flame current of a pristine flame in the presence of an electrode coated for 1 minute under the influence of a +3 kV voltage from the DC power supply. The velocity of the reactive gas mixture is kept constant at v = 8 cm/s and the equivalence ratio is varied between φ = 0.7 to 0.9. The plots show a comparison between the VCC of the pristine flames in the presence of an uncoated and coated electrode.

When a positive polarity is applied to the coated electrode, the flame current increases sharply in the sub-saturation region. The current slowly increases instead of reaching a saturation value until it reaches the super-saturation region. The major distinguishing factor is the absence of the saturation region. As the polarity is switched to negative, the current is observed to increase exponentially. Unlike the case for the uncoated electrode, there is no distinct saturation region or super-saturation region. The decrease in equivalence ratio has a similar effect of lowering the measured flame current due to the reduction in radicals formed due to chemi-ionization.

Figure 3.11 shows the VCC at the constant equivalence ratio $\varphi = 0.9$, and varying reaction gas mixture velocity v = 9 cm/s to 7 cm/s. Similar to the variation in equivalence ratio the decrease in velocity results in a lower flame current due to the reduction in radical formation by chemi-ionization. Therefore, the equivalence ratio and velocity of the reactive gas mixture influence the VCC of the flame in the presence of a coated electrode.

Figure 3.12 shows the VCC at a constant equivalence ratio of $\varphi = 0.9$, velocity. v = 8 cm/s, and varying deposition times of 1, 2, and 4 minutes at +3 kV electrical potential applied to the semi-permeable electrode. The precursor flow rate during the deposition is constant at 0.03 g/min. As observed in Figures 3.10 and 3.11, the application of a positive electric potential on the semi-permeable electrode did not result in a saturation current. The flame current displayed a shallow rise with increasing voltage until the breakdown.

As a negative potential is applied, the flame current increases sharply with the application of higher voltages. The increase in particle film deposition time resulted in a thicker coat on the surface of the electrode. A rise in particle layer thickness increased flame current as observed in Figure 3.12. The increase in current is due to the formation of secondary charge carriers due to back discharge. The higher thickness resulted in a larger voltage drop across the particle layer that led to the increased production of secondary charge carriers. As these charge carriers move toward their respective electrodes, they increase the measured flame current.

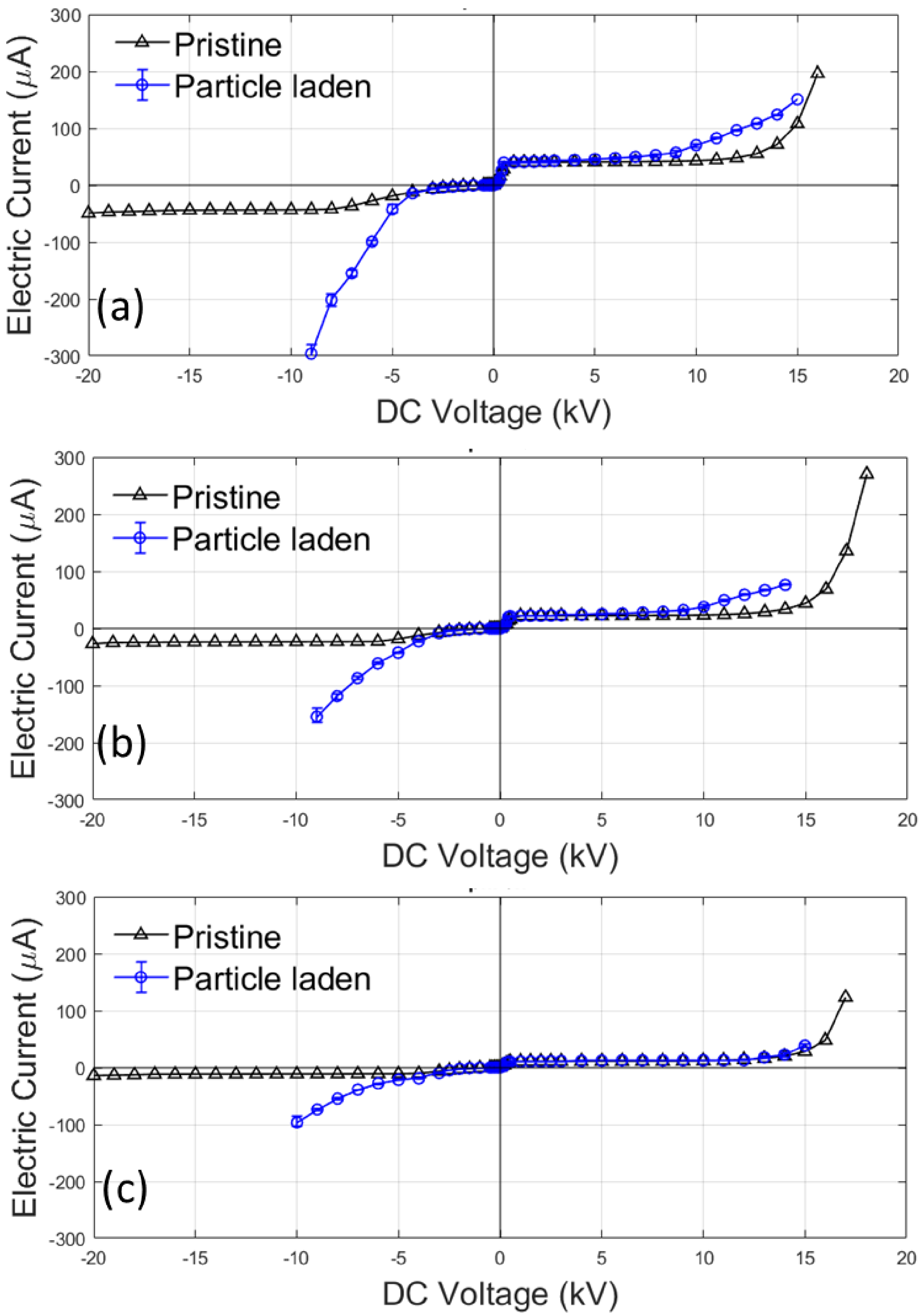

Figure 3.10. Comparison of VCC of pristine and particle-laden electrode coated for 1 minute at constant velocity v = 8cm/s and varied Equivalence ratio (a) 0.9, (b) 0.8, (c) 0.7.

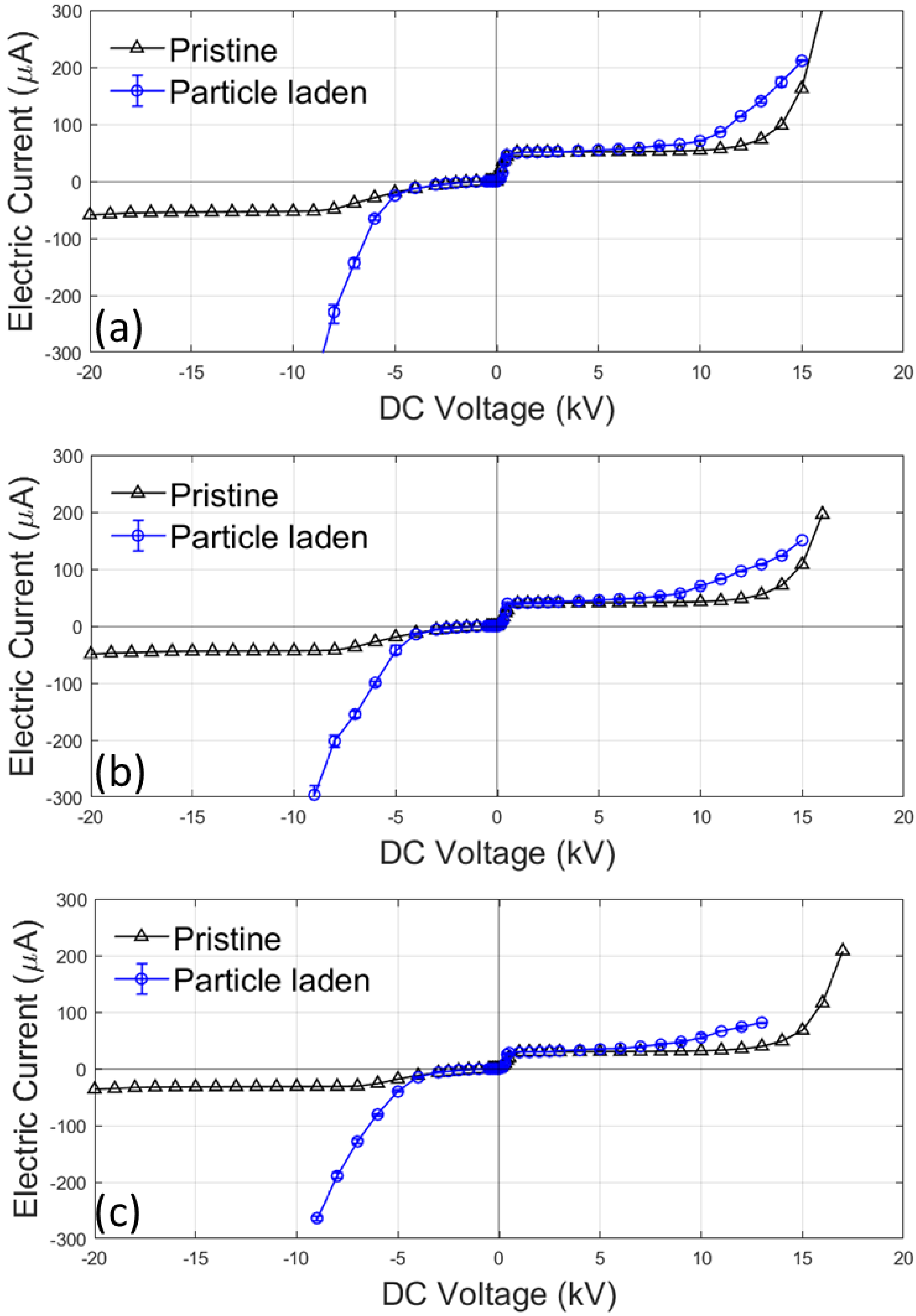

Figure 3.11. Comparison of VCC of pristine and particle-laden electrode coated for 1 minute at constant φ = 0.9 and varied velocity (a) 9 cm/s, (b) 8 cm/s, (c) 7 cm/s.

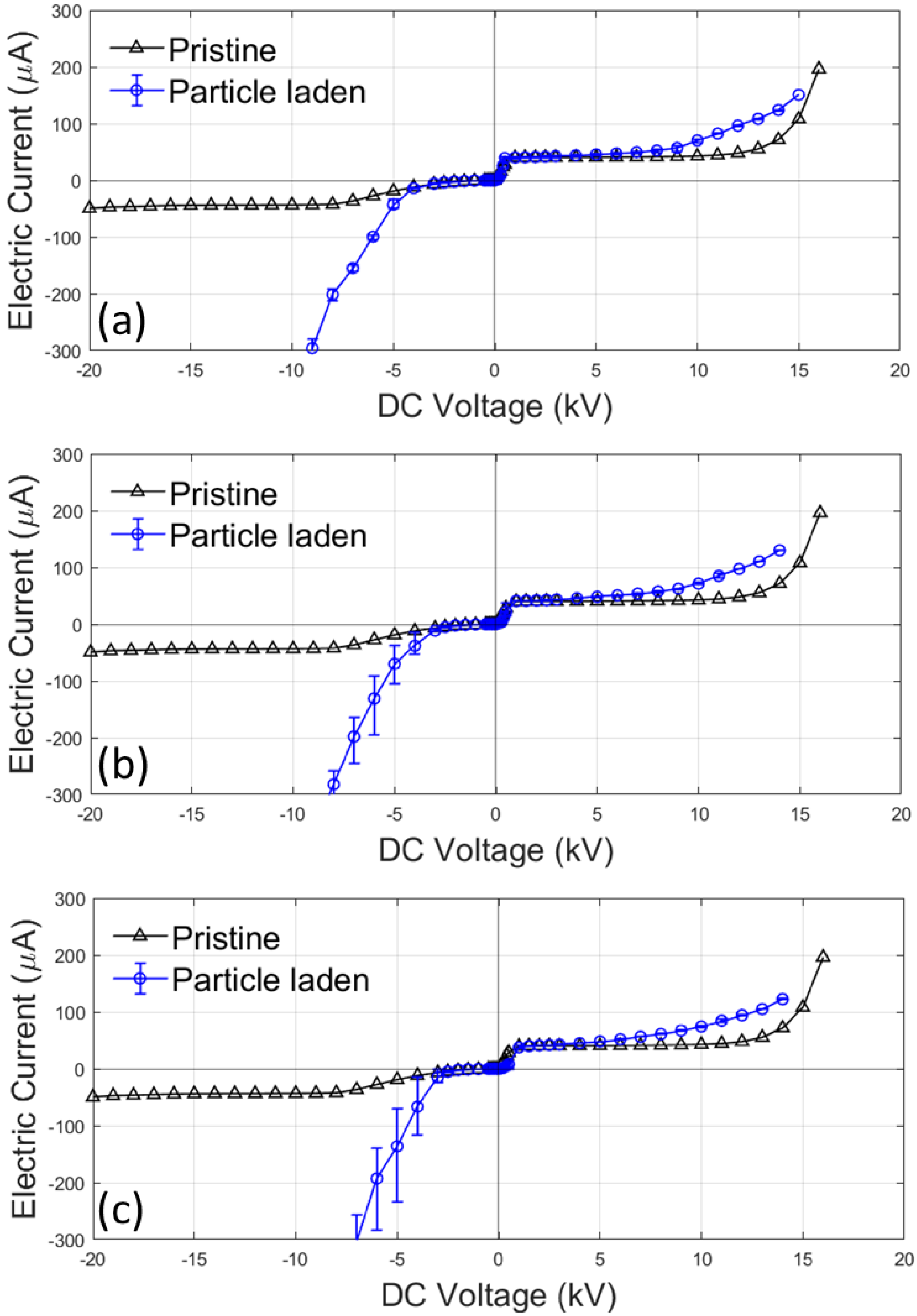

Figure 3.12. Comparison of VCC of pristine and particle-laden coated at constant φ = 0.9 and velocity = 8 cm/s at varied deposition time (a) 1 min, (b) 2 min, (c) 4 min at +3 kV.

3.4 Effect of precursor flow rate on the VCC of particle-laden flame

The VCC of an unseeded flame at an equivalence ratio of $\varphi = 0.9$ and velocity of $v = 8$cm/s is compared to a seeded flame with varying precursor flow rates 0.03 g/min to 0.09 g/min Figure 3.12. When a positive voltage is applied to the electrode the characteristic peak at ~2 kV is observed to be present at all precursor flow rates. The peak current is observed to be reduced by 10-20 % with the increase in precursor flow rate. The flame current of the particle-laden flame is reduced due to the higher concentration of particles in the flame volume.

A negative polarity shows a similar trend where the flame current reduces as the precursor's flow rate increases. As the applied potential approaches the saturation voltage, there is an exponential increase of measured flame current at 0.03 g/min compared to the shallow increase in current for 0.06 g/min and 0.09 g/min precursor flow rate. The increase in flame current for the 0.09 g/min is shallower compared to 0.06 g/min. Hence, the change in precursor flow rates affects the VCC of the particle-laden flame. This stems from the increased concentration of flame-synthesized particles in the flame volume that capture the charges and limit the number of charge carriers impinging on their respective electrodes.

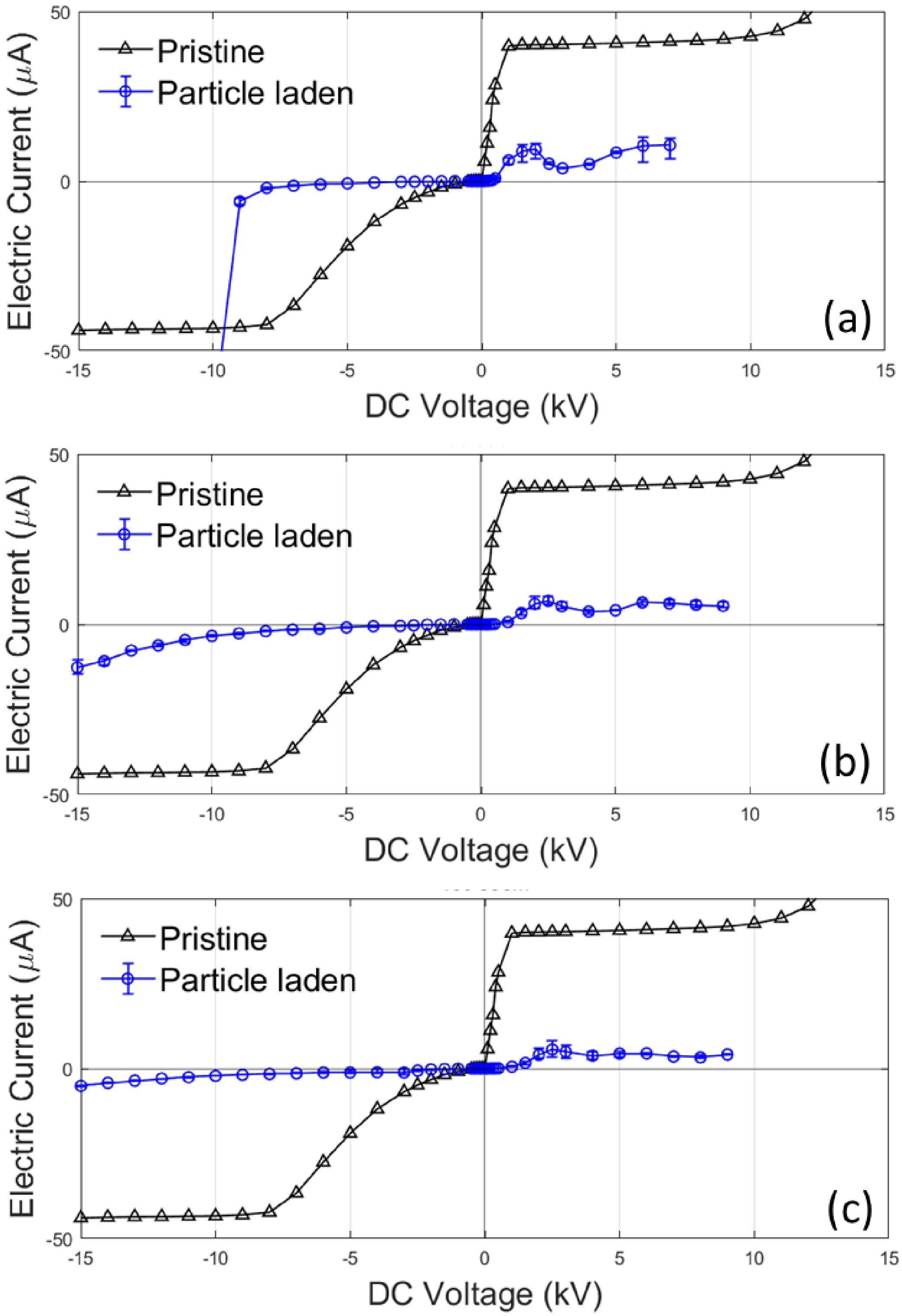

Figure 3.13. VCC at constant φ = 0.9 and velocity = 8 cm/s at varied precursor flow rate (a) 0.03 g/min, (b) 0.06 g/min, (c) 0.09 g/min.

Chapter 4: Yield of particles collected on the semi-permeable electrode

One of the main objectives of the current study is the direct deposition of particles produced in the gas phase onto the solid semipermeable substrate acting as the electrode. The most common method of deposition of particles on solid substrates is by using a liquid suspension (Tsougeni et al., 2010). However, the liquid deposition technique used is a time-consuming method spanning several minutes to hours. Which in turn makes it expensive and cumbersome.

Gas-phase synthesis and direct deposition onto the substrates is an alternative that is receiving a lot of attention as it reduces the steps and time required to produce the nanoparticle films (Strobel et al., 2007). The use of direct deposition also reduces the cost and time for the production of the end product (Pratsinis, 2010; Rudin et al., 2012). Reactive Spray Deposition Technology (RSDT) is another method that combines nanoparticle synthesis in the gas phase and thin film deposition in one step (Ouimet et al., 2021; Roller et al, 2017; Roller et al., 2015). In RSDT, the precursor is atomized and sprayed directly into a high-temperature flame volume instead of mixing with the reaction mixture before combustion. As the droplets pass through the flame, they decompose into gas-phase species, leading to the formation of nanoparticles. The nanoparticles grow while they travel through the flame volume. The deposition of particles in the former cases is through thermophoresis, i.e. through the thermophoretic forces induced by temperature gradients between the combustion gases and the substrate.

In the current study, the precursor solute is atomized and mixed with the fuel and air to produce a premixed mixture. The premixed gas is then ignited at the burner lip for the production of nanoparticles. The particles produced impact the semipermeable substrate and are deposited on it due to thermophoresis and electrostatic forces. A DC electric potential is applied to the substrate to augment the particle collection or film coating through electrostatic precipitation.

4.1 Experimental procedure

Experiments are conducted to analyse the nanoparticle film coating on the semi-permeable wire mesh electrode. A wire mesh disc of diameter 25 mm is mounted on the semi-permeable substrate used as the electrode. The electrode is maintained at a predetermined polarity and voltage throughout the test duration. The wire mesh disc is coated with silica particles for 180 seconds at an equivalence ratio φ = 0.9, and velocity v=8 cm/s for voltages from -7 kV to 7 kV in 1 kV increment. The disc is weighed before and after collection to measure the weight of the particle coating. A Mettler Toledo AB 135-S scale with a resolution of 0.01 mg is used.

4.2 Effect of DC polarity and voltage on film coating

Figure 4.1 shows the weight of the collected particles on the 25 mm diameter wire mesh. Applying a positive polarity results in a rapid increase in the weight of the film coating. The rise in the measured weight reaches its local maxima at approximately 2 kV. As the voltage increases the particle yield gradually drops until it reaches 6mg at 7 kV. The increase in the measured weight of the film coating is a result of the improved collection efficiency of the electrode due to electrostatic precipitation. As the voltage is increased further the measured weight begins to drop. The drop is a result of the reduction in charge carrier concentration. A voltage higher than 4 kV provides enough energy to the charge carriers to move toward the electrode without charging the nanoparticles. This is observed in Figure 4.1 where the measured weight drops and in Figure 3.5 where the measured flame current rises. For the negative polarity, the weight remains relatively low in the range of 1~2 mg.

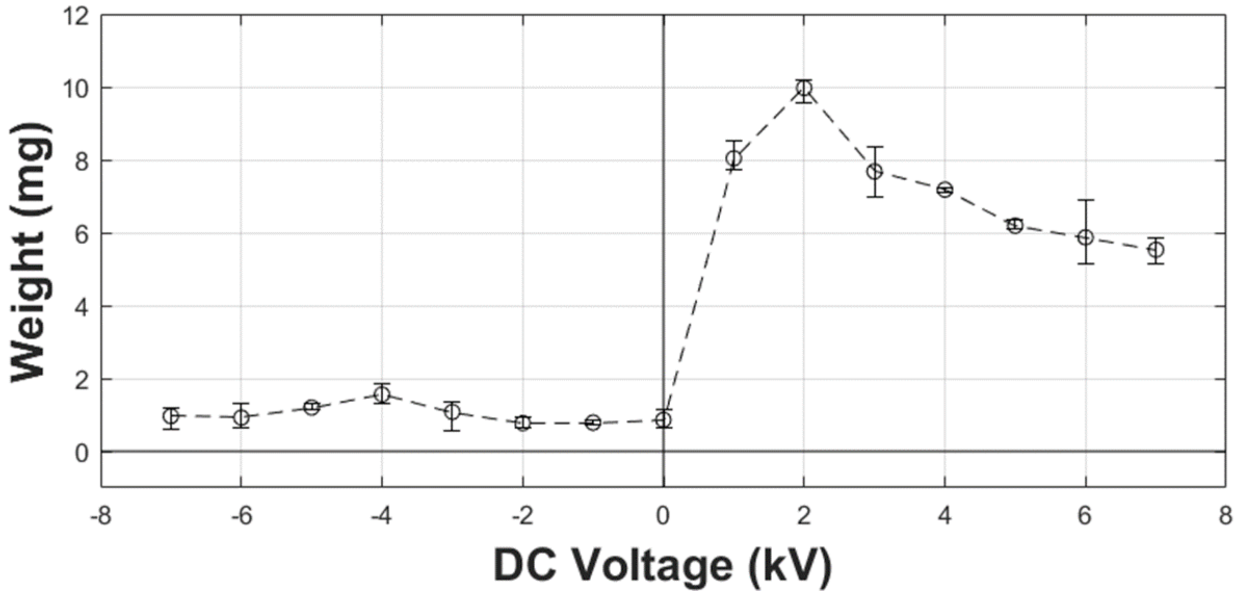

Figure 4.1. Weight of the particles collected at φ = 0.9, and velocity v=8 cm/s for voltages from -7 kV to 7 kV.

4.2.1 Effect of electric field on the yield of the particles

The yield of silica nanoparticles is calculated based on the measured weight of the collected particles and the precursor flow rate. The theoretical value of silica particle production from hexamethyldisiloxane precursor is calculated. A global two-step reaction scheme for HMDSO is used to calculate the yield of the film coating (Feroughi et al., 2017).

$$HMDSO + OH \rightarrow 2\ SiO + 6\ CH_3 + H \qquad \text{(R 4.1)}$$

$$SiO + H_2O \rightarrow SiO_2(g) + H_2 \qquad \text{(R 4.2)}$$

Figure 4.2 shows the yield of the particles collected at φ = 0.9, and velocity v=8 cm/s for voltages from -7 kV to 7 kV. The variation of the yield follows the same trend as the weight of the particles collected at the same flame conditions. Application of a positive voltage results in the initial increase of the yield to 70%, followed by a decrease due to the reduction in charge carrier concentration. For the 0 kV case and negative polarity, the yield remains at around 7-8%. The yield increases tenfold with the application of a positive 2 kV voltage due to the increase in the collection efficiency of the electrode.

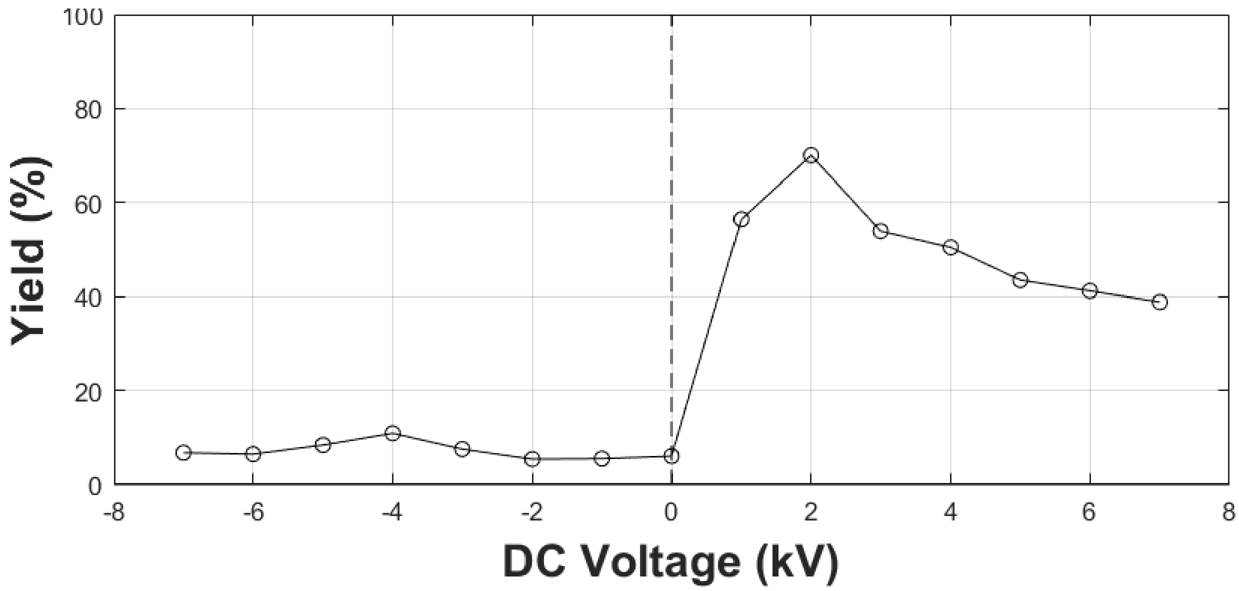

Figure 4.2. Yield of the particles collected at φ = 0.9, and velocity v=8 cm/s for voltages from -7 kV to 7 kV.

4.2.2 Particle yield and flame current superimposed

The application of a positive DC potential on the semi-permeable electrode reveals a characteristic peak as the voltage is increased on the yield of the particles (Figures 4.2), and VCC of particle-laden flame (Figure 3.5). To investigate the coincidence in the measurements the yield of particles (Figure 4.2) is superimposed on the measured VCC (Figure 3.5) at the same flame conditions in Figure 4.3. It is observed that the initial peak at ~2 kV for the flame current measurement corresponds with the peak of the yield of the particles. This indicates that the peak in current is due to the transfer of charges from the particles deposited on the electrode. An increased voltage of ~3-4 kV, provides enough energy to the charge carriers to move toward the electrode without charging the nanoparticles. This results in the charge carriers moving to the electrodes without charging the flame-synthesized particles. As the voltage is increased further the current increases due to the rise in concentration of pristine charges correlating with a decrease in yield. Therefore, current increases at higher voltages due to the increase in charge mobility and reduction of charging efficiency. The breakdown occurs much earlier at ~8 kV and ~-9 kV for the positive and negative potential, respectively, for the particle-laden flame.

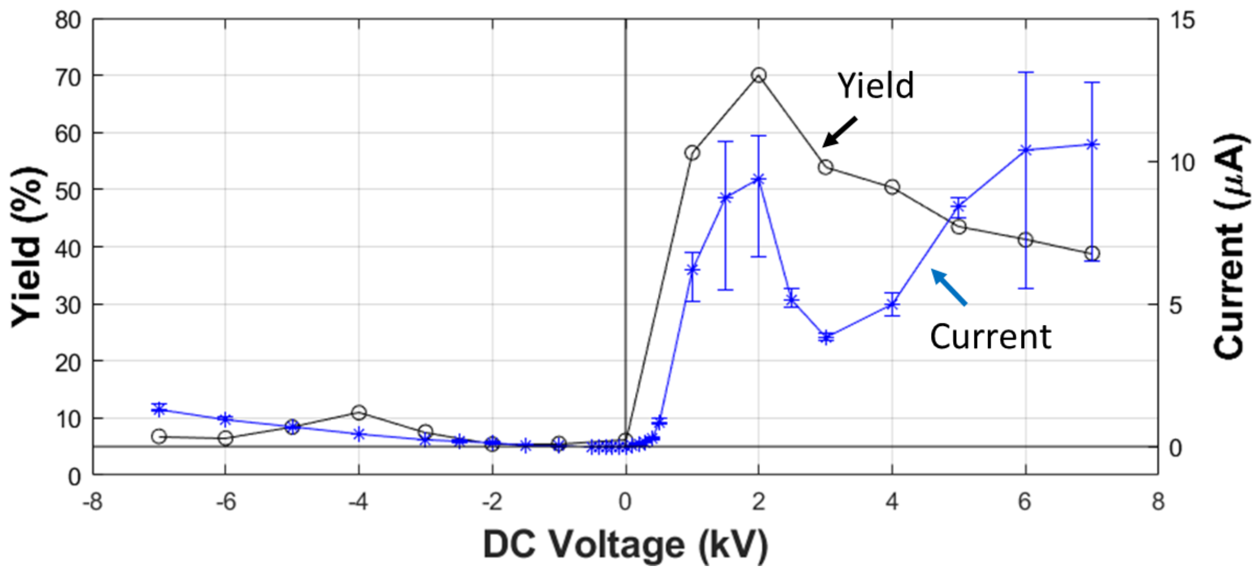

Figure 4.3. The current and yield of the collected particles are superimposed at an equivalence ratio of φ = 0.9, and velocity v=8 cm/s for voltages from -7 kV to 7 kV.

4.3 Effect of deposition time on the weight of collected particle

The time-resolved weight measurements are plotted in Figure 4.4 to show the effect of the thickness of particle build-up on the collection efficiency of the semi-permeable electrode over time. The particle film coating is collected on the 25 mm diameter wire mesh and weighed using the Mettler Toledo AB 135-S scale with a resolution of 0.01 mg at each time step. A flame at an equivalence ratio of φ = 0.9, and velocity v=8 cm/s with a precursor flow rate of 0.03 g/min is studied. A +3 kV potential is applied for the positive electric potential case and a -3 kV for the negative case. The weight of the particles is measured at one, two, four, eight, and, twelve minutes for both cases. The weights are measured thrice and averaged to obtain the mean value at each time step. The plot depicts the weights normalized to one minute of collection for each case. The purpose of the study is to understand the effect of particle build-up on the collection efficiency of the semi-permeable electrode.

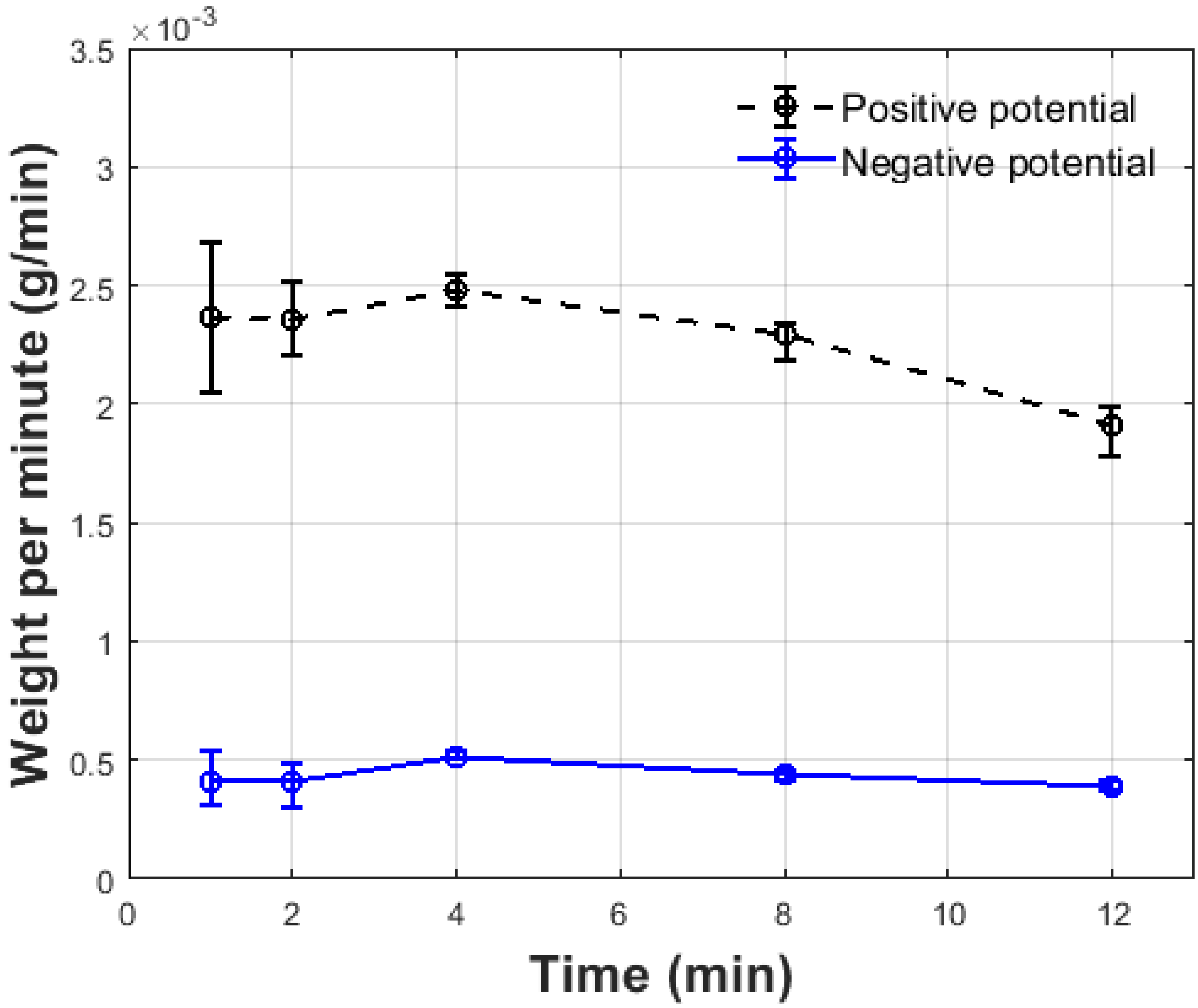

Figure 4.4. Time-resolved weight measurement at φ = 0.9, and velocity v = 8 cm/s for -3 kV and 3 kV voltages.

It is observed that the build-up of particles over time did not have a significant effect on the particle collection efficiency of the DC-powered electrode. This can be observed for both the positive and negative cases. The variation for the positive potential case is approximately 2 – 2.5 mg, while the variation for the negative cases is between approximately 0.4 – 0.6 mg.

As a positive potential is applied to the electrode, a steep initial peak is observed at 1 minute followed by a minor decrease at the 2-minute time step. A secondary peak is then observed as the time of collection is increased to 4 minutes, after which the weight of the particles collected decreases with a shallower slope. A similar trend is observed when a negative potential is applied to the semi-permeable electrode. A build-up of particles on the surface of the electrode does not affect the electric field applied between the semi-permeable electrode and the grounded burner. Hence, the particle film coating does not decrease the collection efficiency of the semi-permeable electrode despite producing a layer of high-resistivity silica nanoparticles on its surface.

Chapter 5: Electron microscopy imaging

To characterize the particle surface structure, particle diameter, size distribution and the composition, the samples are collected and analysed under SEM, TEM and EDS. Information about the samples' surface and composition can be extracted using SEM, and sample structure and morphology data can be obtained through TEM. Multiple studies have used SEM and TEM to characterize silica nanoparticles (Chung et al., 2024; Florek et al., 2017; Huseynov et al., 2016). The flame-generated particles collected on the electrode are characterized under SEM, TEM, and Energy-Dispersive X-ray Spectroscopy (EDS).

5.1 Experimental procedure

The flame conditions throughout the experiment are maintained at an equivalence ratio $\varphi = 0.9$ and velocity $v = 8$cm/s. To collect silica particles to be placed under the SEM a strip of bare metal wire of diameter 0.5 mm (0.02 in.) is attached to the electrode. The electrode is maintained at a predetermined voltage spanning between +3 kV to -3 kV for the duration of the test. The purpose of the initial sample collection was to determine the coating time required to obtain a high enough density for adequate image quality of silica particles. The samples are collected for a duration of 15, 30, and 60 s. The coated wire was then removed from the electrode and placed on a 25.4 mm pin stub using carbon tape. The samples were then taken to the Analytical Instrumentation Facility for analysis under the Hitachi SU8700 SEM in the high-resolution and variable pressure mode for electrically stable and unstable samples respectively. The images obtained for the variation in electric potential and time tests are in the high-resolution mode of the SEM, as these samples were electrically stable under the electron beam, this would result in the SEM being shut down and de-energized before imaging could resume.

Similarly, to collect samples for TEM and EDS, a bare metal wire of a diameter of 0.02 inch is attached to the electrode to collect the flame-generated particles. The electrode is maintained at a constant voltage spanning between -7 kV to +7 kV for 180 s. The coated wire is then removed from the electrode and cut into 1-inch strips. The strips are placed in a 6 ml solution of methanol and sonicated. The solution with the particles is then metered onto TEM carbon film 300 mesh using 6 ml pipettes. The samples are imaged in the Talos F 200X at AIF. The images are processed using ImageJ and MATLAB.

5.2 Scanning electron microscopy images

Figure 5.1 shows the surface structures imaged using SEM for samples collected at -3 kV, 0 kV, and +3 kV for 30 s duration. The coating on the wire is visible to the naked eye as a fuzzy layer with branches in the case of +3 kV and as a white coating for the 0 kV and -3 kV tests. As the application of electric potential improves collection efficiency, the flame-generated particles coated the entire surface area of the wire. This results from the wrap-around phenomenon, where the electrostatic force from the energized electrode directs charged particles to coat any free conductive surface. However, the coating on the surface facing the flame is denser compared to the sides of the wire. Figures 5.1 (a- c) show the bush-like structure on the surface of the wire. The coating of the flame-generated particles depicts a dendritic structure with branches protruding outward. The application of an electric potential increased the density of the coating, with +3 kV having the highest density followed by -3 kV and then 0 kV. The visualization of the higher density at a positive potential is in accordance with the yield of particles in Chapter 4. Due to the difference in mobility between charge carriers, the negative charge carriers (electrons) have a higher particle charging efficiency. As a result, the negatively charged particles yield a higher-density coating under SEM. As the images are captured using the SEM, the branches appeared to sway due to the application of the electron beam from the SEM's probe.

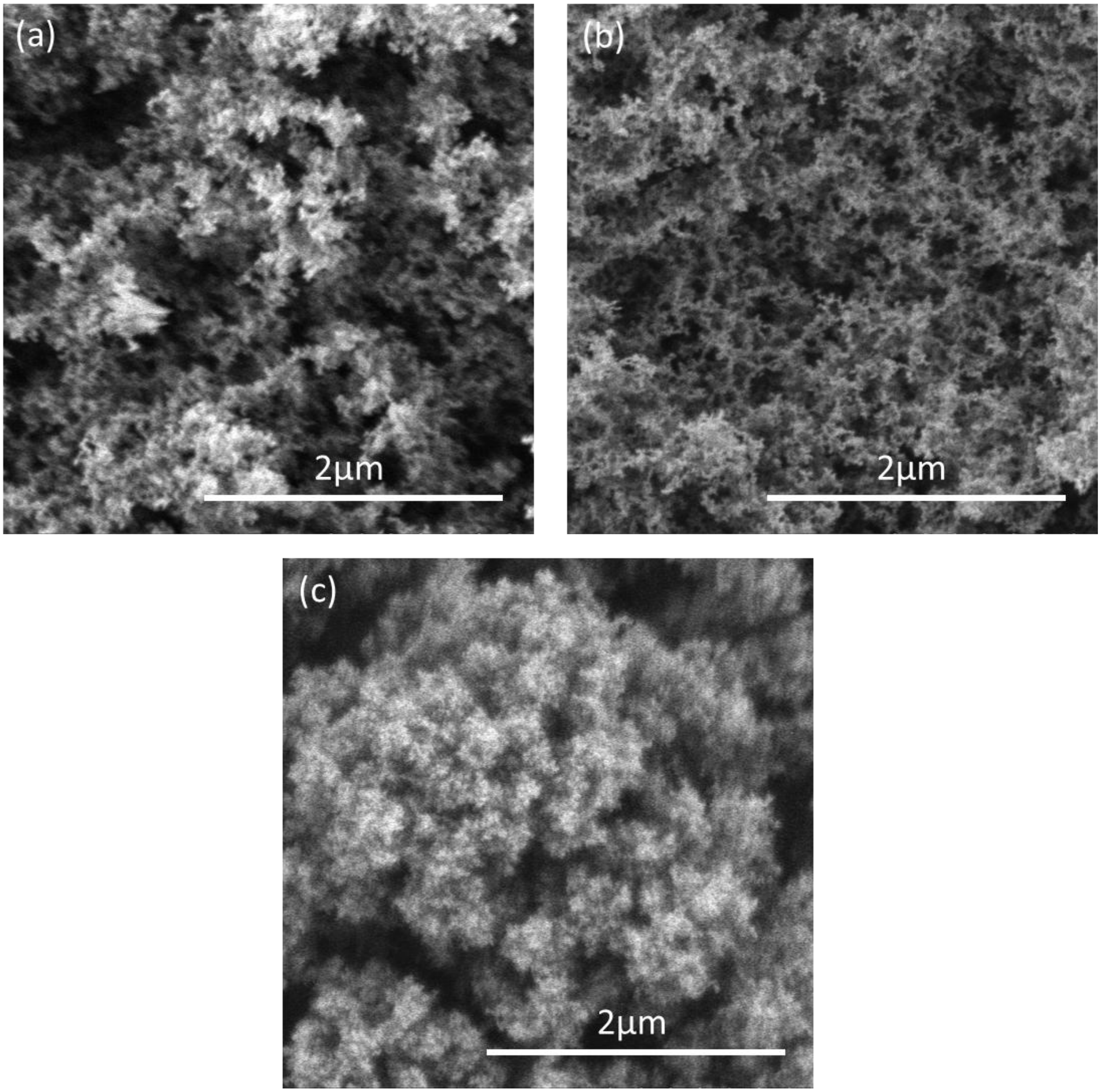

Figure 5.1. SEM images at equivalence ratio φ = 0.9 and velocity v = 8cm/s, for 30 s (a) -3 kV, (b) 0 kV, and (c) +3 kV.

5.2.1 SEM images based on time of coating

Figure 5.2 shows the images depicting the variation in density with respect to time. The samples are collected at an electrode potential of -3 kV. As the particle yield suggested a low yield at negative potentials of the electrode, the value of -3 kV is chosen to optimize the process of sample collection. The collection duration is varied from 0 s to 30 s with a time step of 15 seconds.

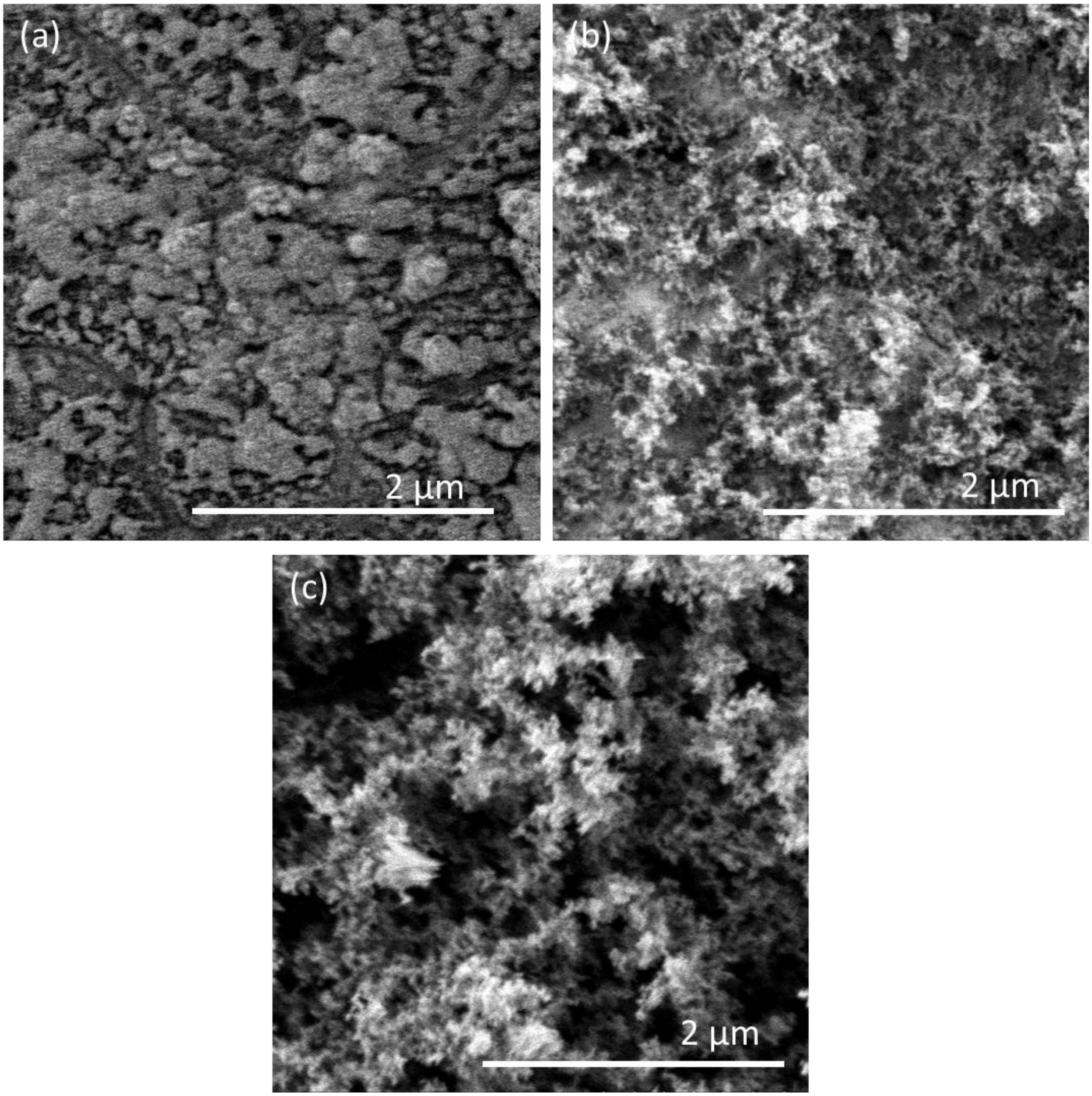

Figure 5.2. SEM images at equivalence ratio φ = 0.9 and velocity v = 8cm/s, for a duration of (a) 0 s, (b) 15 s, and (c) 30 s at -3 kV.

The flame-generated particle coating was visible to the naked eye for the 30-s test. Figure 5.2 (a) shows the SEM image of the bare wire that is exposed to the high temperatures of the reactive gases flowing downstream of the flame. As the duration of the collection is increased to 15 s, minute dendritic structures are observed, as shown in Figure 5.2 (b). However, the density of the coating is not high enough to be visible to the naked eye as the structure barely extends beyond the surface of the wire. Further increase in coating time showcased the densest coating of particles with protruding branches from the dendritic structures shown in Figure 5.2 (c).

5.2.2 Coating layer thickness

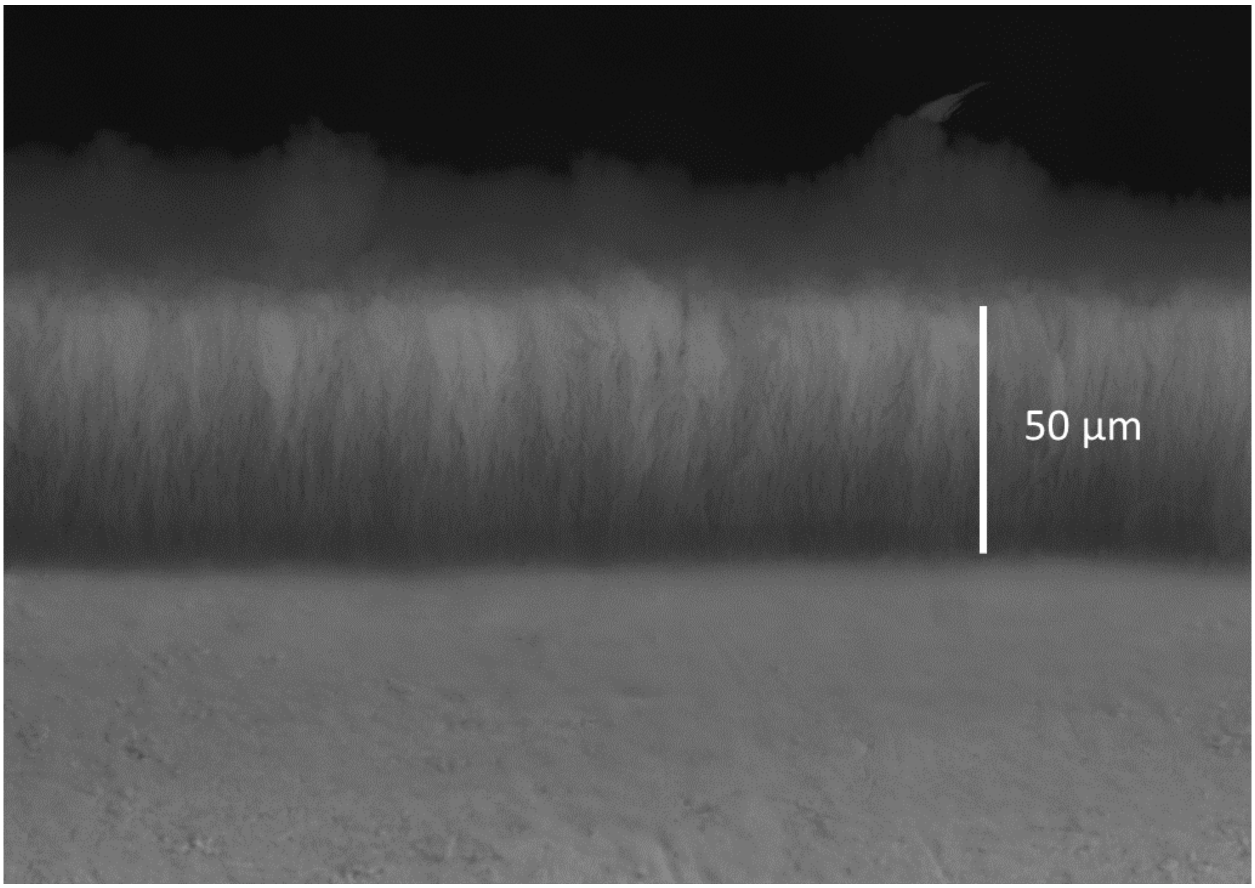

Figure 5.3. SEM image (PDBSE 20 kV) measuring the thickness of the flame-generated particle coating at an equivalence ratio φ = 0.9, velocity v = 8cm/s, and duration of 60 seconds.

Figure 5.3 shows the thickness of the flame-generated particle coating at equivalence ratio φ = 0.9, velocity v = 8cm/s, electric potential of +3 kV, and a collection duration of 60 seconds. A thickness of 53 µm is measured from the base of the coating at the wire to the top of the dendritic structures. The image appears as a dense forest with tall trees. Image is obtained using SU8700 Hitachi SEM's variable pressure mode as the sample was electrically unstable and created an arc. Figure 5.3 shows a gradient in the grayscale imaging with a brighter and darker region at the top and bottom of the particle layer, respectively.

This is directly related to the backscattered electron emission coefficient from the silica nanoparticles and the packing density of the layer deposited on the metal wire. The back scattered electron emission coefficient is proportional to the packing density . As the particle layer mainly consists of SiO_2 particles the increased brightness in the image is a direct result of an increased packing density in the upper region as compared to the lower region.

As a result of SEM imaging the surface structure of directly coated silica nanoparticles is visualized. The particles were found to be on the nanometer scale, making high-resolution imaging under an SEM challenging. Therefore, SEM images are used to characterize the surface structures of the samples, while TEM images are used to characterize the size and size distributions of the silica nanoparticles.

5.3 Transmission electron microscopy images

The flame-generated particles are also imaged under a TEM to obtain information about the particle diameter and size distributions. Figures 5.4 and 5.5 show the TEM images, the size distribution, at an equivalence ratio $\varphi = 0.9$, velocity $v = 8$ cm/s, and electric potentials spanning from -7 kV to +7 kV. The images obtained show agglomerates of spherical particles forming fractal structures. The diameter of individual particles is measured using Fiji ImageJ. The diameter of the particles from the TEM images is processed using MATLAB to obtain the size distributions. The particles are characterized in ranges of 2 nm as shown in Figure 5.5. Table 1.1 shows the size distribution at electric potentials spanning between -7 kV to +7 kV.

The average particle diameter is 11 nm under the influence of an electric field of any potential. Figure 5.5. shows 80% and 60% of the particles fall within the size range of 8-12 nm for both the positive and negative potential of the electrode. However, it is observed that the application of positive electric potential results in a narrower size distribution, where the majority of particles fall within the 8-12 nm range with the exception being the +7 kV test. The application of a negative potential broadens the size distribution with 85% of the particles within the 8-14 nm range.

Table 5.1. Percentage of the number of particles within a size range.

Voltage, kV	Total	Particle diameter (nm)				
		6-8	8-10	10-12	12-14	14-16
-7	57	1.75%	24.56%	33.33%	36.84%	0.00%
-5	58	1.72%	18.97%	48.28%	29.31%	1.72%
-3	50	0.00%	26.00%	42.00%	26.00%	4.00%
-1	81	1.23%	18.52%	33.33%	20.99%	18.52%
0	33	6.06%	21.21%	36.36%	18.18%	18.18%
1	70	8.57%	40.00%	42.86%	8.57%	0.00%
3	60	8.33%	30.00%	43.33%	13.33%	1.67%
5	76	6.58%	36.84%	42.11%	13.16%	1.32%
7	71	8.45%	38.03%	29.58%	18.31%	2.82%

As the electric field is applied, a region of space charge is created between the flame front and the wire mesh electrode. The space charge holds the opposite polarity to that of the electrode due to the movement of charge carriers through the flame volume. Silica particles are charged to the same polarity as the space charge as they pass through. As the particles are charged to the same polarity, electrostatic repulsion sets in, resulting in a repulsive force. Owing to the repulsion, the size of the particles is reduced. The outlier (+7 kV) in the positive potential tests is a result of the strong electric field, resulting in a lower charging efficiency. This is attributed to the strong electrostatic effects forcing the charge carriers to move to the electrode without charging the flame-generated particles.

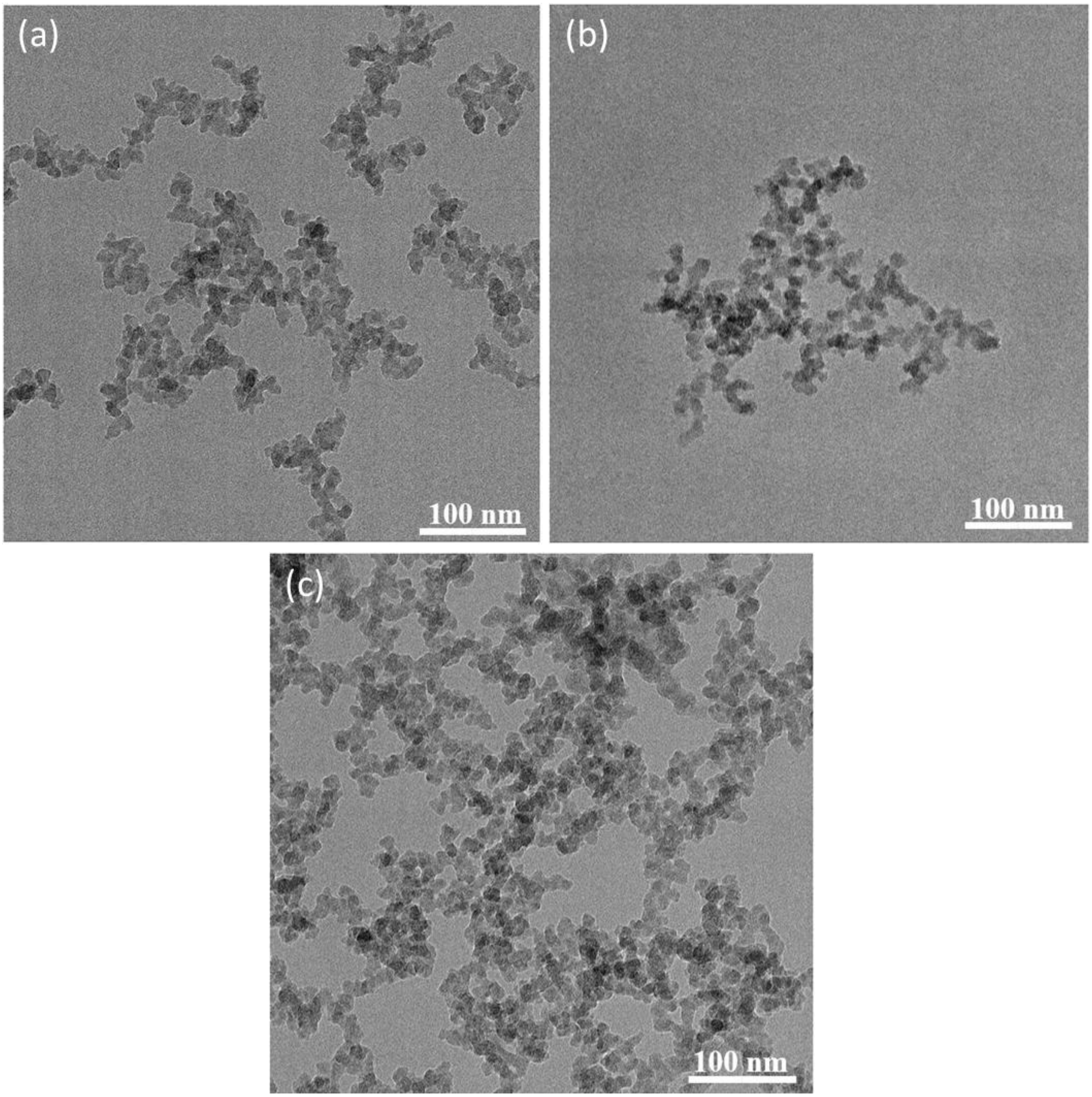

Figure 5.4. TEM images at (a) -3 kV, (b) 0 kV, and (c) +3 kV.

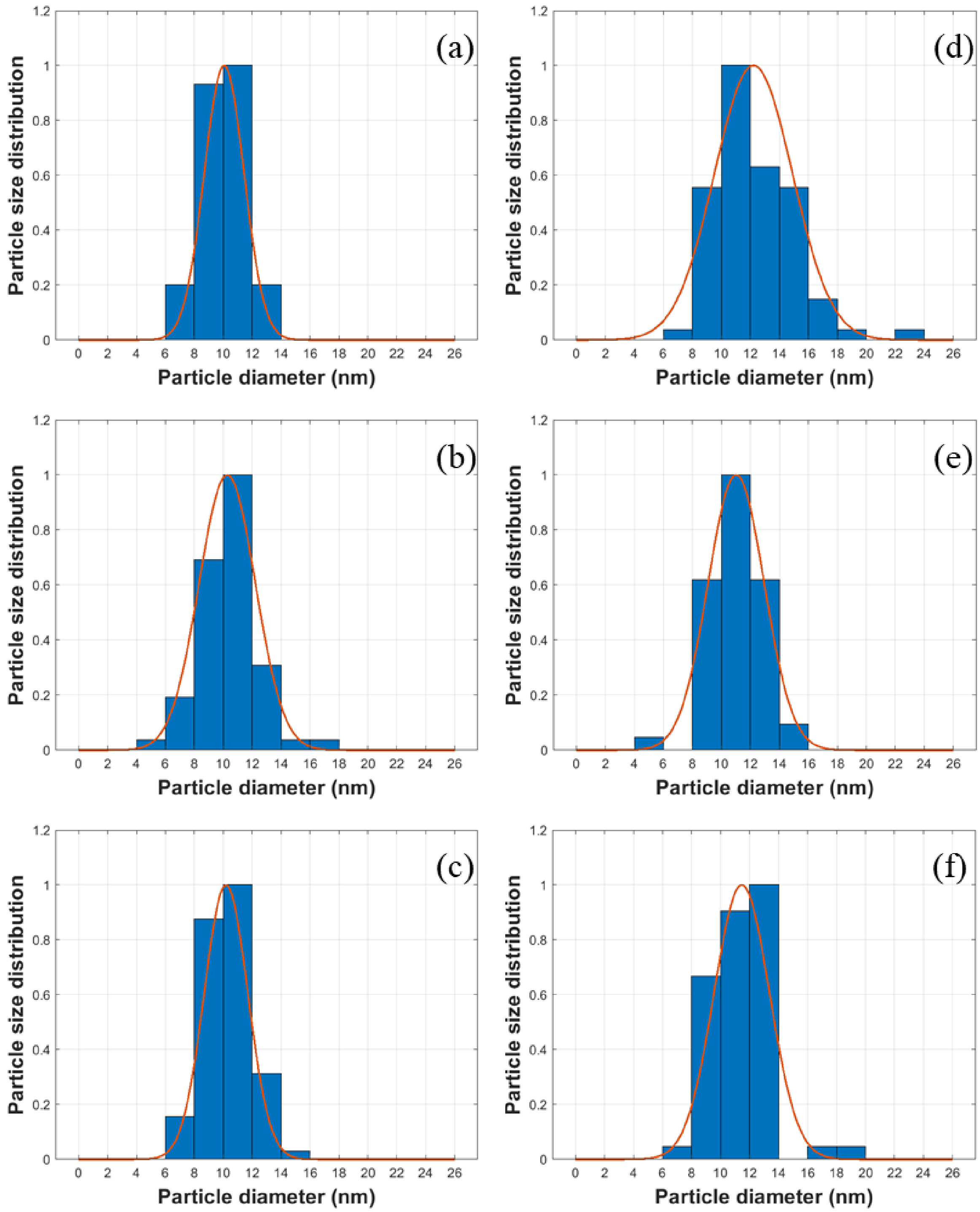

Figure 5.5. Particle size distribution from TEM at an equivalence ratio of φ = 0.9, and velocity of v=8 cm/s under electrode electric potentials of (a) +1 kV, (b) +3 kV, (c) +5 kV, (d) -1 kV, (e) -3 kV, (f) -5 kV.

The mobility of electrons is significantly higher than positive ions, resulting in high particle charging efficiency. This results in the negative electric field or positive electrode potential marginally narrowing the size distribution of the particles. The effect of the electric potential is significant with a change in electrode configuration (Vemury et. al., 1995) The study showed an increase in the specific area and a decrease in the particle size due to the application of electric fields across the flame. The specific area measured was significantly higher when a negative electric field was applied as opposed to a positive electric field. The major difference between previous studies and the current study is the configuration of the electrode. Previous studies placed the electrodes parallel to the flow (perpendicular to the burner surface), whereas the current study has the electrode parallel to the burner face and perpendicular to the flow of gases.

5.4 Energy dispersive X-ray spectroscopy

Energy dispersive X-ray spectroscopy (EDS) images are obtained to understand the material composition of the samples. Figure 5.6 shows the qualitative EDS images at electric field potentials of -3 kV, 0 kV, and -3 kV. It is observed that the sample composition contained Si and O as depicted by the peaks in the EDS spectra images. Along with the peaks for Si and O, peaks are observed for the elements of carbon (C), and copper (Cu). This is attributed to the TEM grid used, which has a composition of copper and carbon. The copper makes the mesh that supports the samples and is coated with a thin layer of carbon, providing a platform for the placement of samples during TEM and EDS analysis.

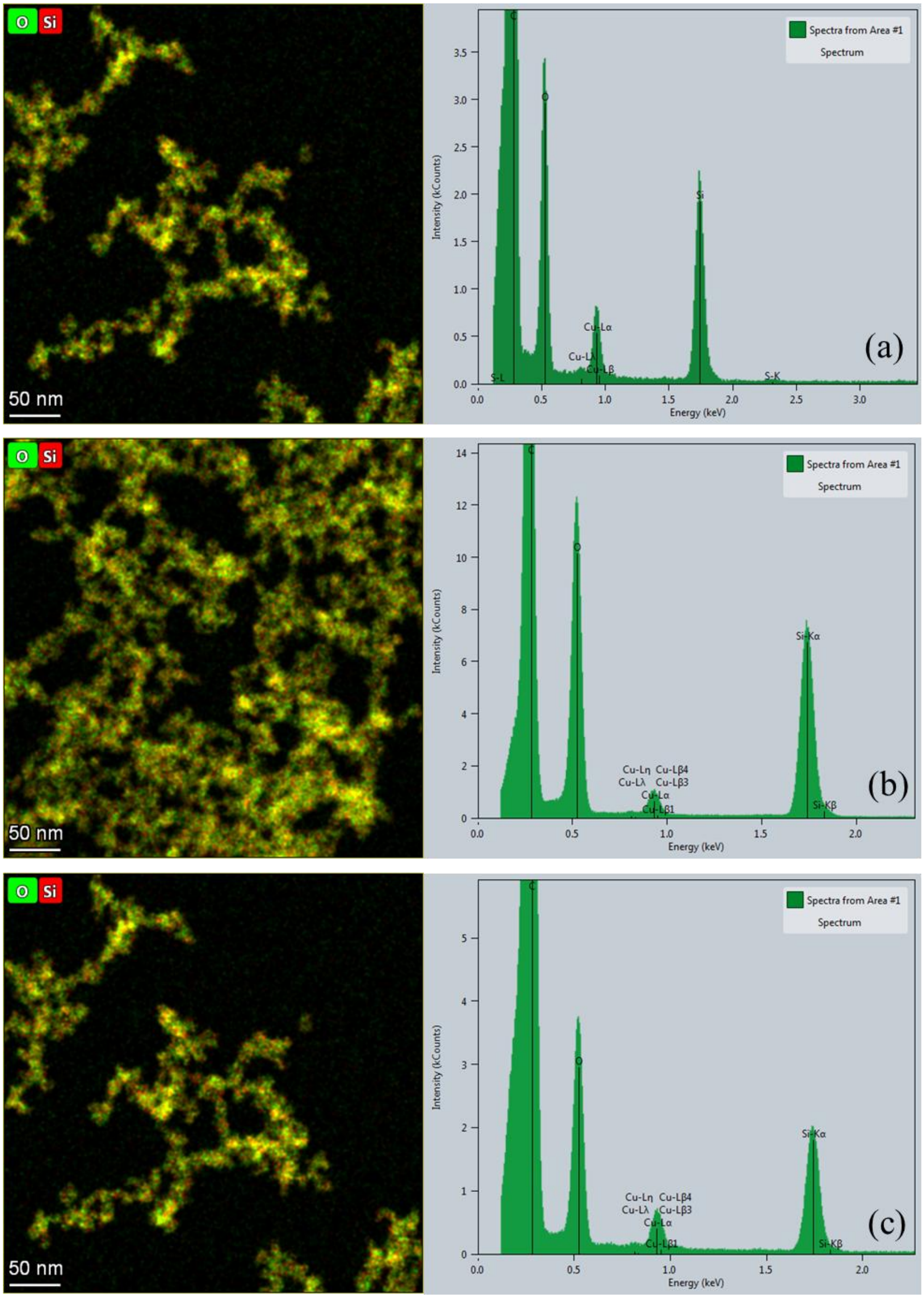

Figure 5.6. Energy Dispersive Spectroscopy of Silica nanoparticles at an equivalence ratio of 0.9 and velocity v=8 cm/s, under the influence of external electric field (a) -3 kV, (b) 0 kV, and (c) +3 kV.

To quantitatively measure the composition of nanoparticle samples, methods such as inductively coupled plasma mass spectrometry/optical emission spectroscopy (ICP-MS/ICP-OES)could be used. ICP-MS ionizes elements in plasma and utilizes mass spectroscopy to measure the ions. ICP-OES analyzes the light emitted from excited atoms in the plasma to determine the concentration of elements. Both ICP-MS and ICP-OES require the destruction of the samples.

X-ray diffraction and high-resolution TEM imaging can also be used to analyze the crystal structures of nanoparticle samples collected at varying electric potentials.

Therefore, TEM imaging is used to obtain the particle diameter and size distribution under the influence of external electric fields. High-resolution imaging showed the application of a positive potential resulted in a marginally smaller particle diameter and narrower size distribution owing to the high charging efficiency of negative charge carriers. TEM images showcased a highly agglomerated structure that could not be directly attributed to the coated layer due to the TEM sample processing. To further understand the composition of the samples EDS is performed. A Si:O ratio of 1:2 is observed suggesting that the particles coated on the electrode are SiO_2.

Chapter 6: Rayleigh scattering

Laser-based imaging such as Rayleigh, and Raman are useful tools for the diagnostics of gases and combustion-formed nanoparticles. Measurements are made with high-power lasers with microsecond durations that can freeze the density field in time and measure complex structures. Rayleigh scattering refers to the elastic scattering of the incident light by the molecular species present in the scattering volume (Havener et al., 2011; Santra et al, 2017). Scattering is in the Rayleigh regime when the scattering molecules or particles are smaller than the wavelength of the incident light. For a mixture of gases, the intensity of Rayleigh light scattering is (Pitts et al., 1983),

$$I(90^o) = N\left[\sum_{j=1}^{m} \sigma_j (90^o) X_j\right] I_o \tag{6.1}$$

Where,

— N is the total number density of molecules,

— σ_j is the Rayleigh scattering cross-section,

— X_j is the mole fraction of species j, and

— I_o is the incident light irradiance (W. M. Pitts, 1995) which is 90^o to the detector.

Laser diagnostic techniques have been used to characterize combustion-formed particles. Laser Light Scattering (LS) and Laser-Induced Incandescence (LII) are proven techniques used in flame studies (Li et al., 2016; Liu et al., 2017; Michelsen, 2017; Sipkens et al., 2022). Elastic LS is divided into two categories based on the wavelength of the incident light and the size of the scattering particles. Rayleigh scattering ($\lambda >> d$) and Mie-scattering ($\lambda << d$). Rayleigh scattering has been widely used for in-flame nanoparticle size measurement (Di Stasio, 2000; Lu et al., 1994; Sipkens et al., 2022; Sorensen, 2001). Studies investigating the morphological changes of Al_2O_3 particles due to aggregation and sintering processes in a counterflow flame have been performed (Xing et al., 1999). The volume fraction occupied by particles in the aerosol gas mixture and the sizes of nanoparticles from laminar diffusion flames were studied (D'Anna et al., 2005). Production of titania particles in a premixed flame via the oxidation of titanium isopropoxide was studied and compared to TEM measurements (Yang et al., 1997). Scattering from very small particles falls into the Rayleigh range and dominates the scattering if the particle density is high (Miles et al., 2001).

$$I(90^o) = N\left[\sum_{j=1}^{m}\sigma_j(90^o)X_j\right]I_o + N_p\sigma_p(90^o)I_o \qquad (6.2)$$

Where,

— N_p is the total number density of particles,

— σ_p is the Rayleigh scattering cross-section.

The intensity signal of Rayleigh scattering is directly proportional to the number concentration of species and cross-section of the gas mixture and nanoparticles. If the cross-section of the particles is constant then,

$$I \propto N_p \qquad (6.3)$$

In the current study, the angles of incidence and detection are kept constant. The particle diameter and composition of the gas mixture downstream of the flame are assumed to be constant as all measurements are performed at an equivalence ratio ϕ =0.9, velocity v = 8 cm/s, and a precursor flow rate of 0.03 g/min. Therefore, the intensity of Rayleigh scattering is directly proportional to the number density of the particles in the gas mixture.

6.1 Experimental procedure

The electric potential applied to the semi-permeable wire mesh electrode varies between -7 kV to +7 kV. Figure 6.1 shows a Photonics Industries DM30-527 dual head high pulse energy Nd: YLF Laser is used to illuminate the particles downstream of the flame. Collimating and diverging lenses are placed in line with the laser beam to obtain a laser sheet above the burner. The laser is used to illuminate a region spanning from the burner surface to an inch above the electrode.

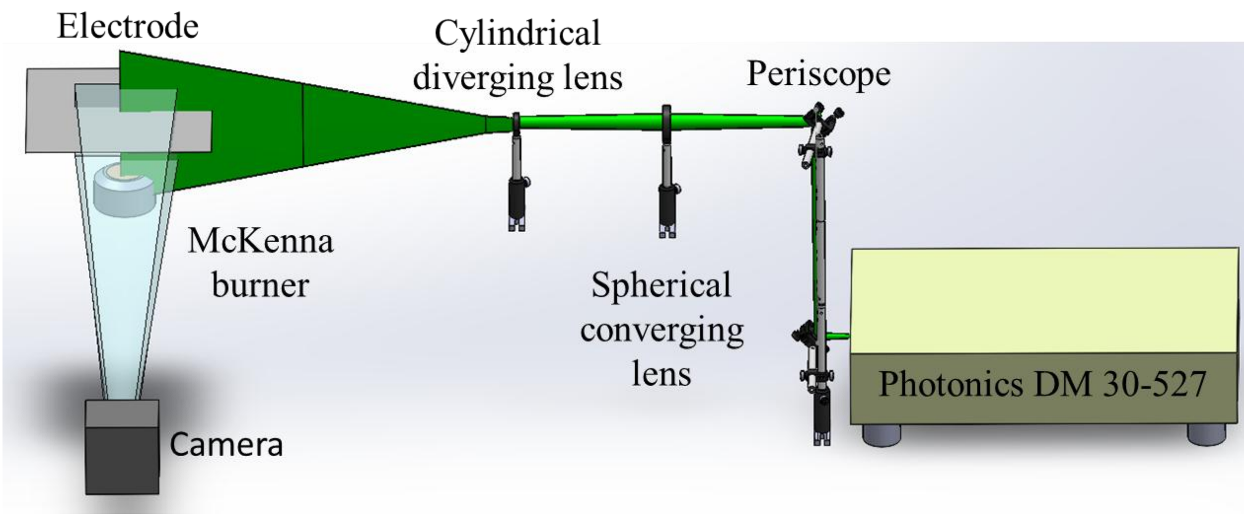

Figure 6.1. Schematic of the laser imaging setup.

A Canon EOS 90D camera is used to capture videos to study the effect of the application of electric potential on the intensity of the scattered light. The test section is manually focused using an EF-S 18-55 mm f/3.5-5.6 lens. Andover Corporation 532 FSX10-50 532nm wavelength filter captures the green laser light. The laser beam creates a 1-D sheet of light that is focused to illuminate the test section, i.e. from the burner surface to an inch above the electrode. The beam is structured to illuminate the flow of the products both upstream and downstream of the electrode to visualize the effect of the applied electric potential. The camera settings are as follows: Shutter speed 1/30, ISO 3200, and F 5.6. The images are captured at 30 frames per second in 4K resolution. The captured images are processed using MATLAB and ImageJ to extract the intensity information. The flame parameters, camera settings, and the position of the laser source and lenses are constant for all the tests.

6.2 Rayleigh scattering of flame-generated particles

The applied electric potential is changed (-7 kV to +7 kV) while keeping flame and imaging conditions constant. The laser scattered light is captured using the camera placed at 90^{o} to the incident light and processed using MATLAB to obtain the average intensity. The averaged images showing the test section with no particle generation (background) are subtracted from the images with particles. This results in an image with the particle density downstream of the flame.

6.2.1 Time-averaged imaging

Figure 6.2 shows the reaction zone illuminated by the high-power laser when an electric potential of 0 kV is applied to the semi-permeable electrode. The lower intensity above the electrode is due to the reduced temperature further from the flame front. The intensity of scattered light is inversely proportional to the temperature of the particles. The particles as they approach the electrode tend to spread to the sides and move through the electrode which decreases the intensity above the electrode.

Figure 6.3 shows the images of the time-averaged flame-generated particle cloud upstream and downstream of the semi-permeable electrode as the electric potential is varied between -7 kV to +7 kV. It is observed that the flame-generated particle cloud downstream of the electrode is relatively denser for the negative and no potential tests as compared to the positive potential tests. The higher concentration of particles downstream of the electrode translates to a lower concentration of particles collected. This corresponds to the particle yield results obtained depicting the higher yield at the electrode as a positive potential is used as depicted in Chapter 4.

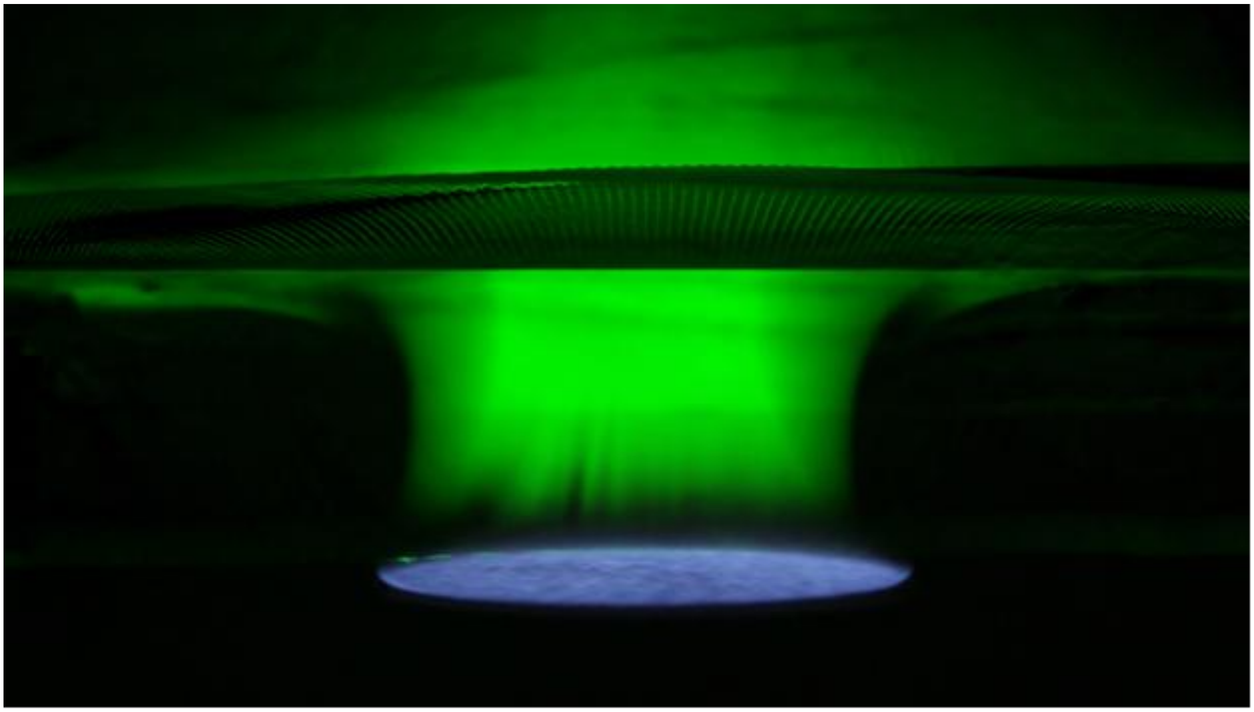

Figure 6.2. The time-averaged flame-generated particle cloud concentration upstream and downstream of the semi-permeable electrode is maintained at 0 kV.

A wrap-around effect on the charged particles is observed due to the applied electric field (Bailey, 1998). The wrap-around effect in electrostatics refers to how charged particles are attracted and adhere to surfaces even on regions not directly facing the particle source. This phenomenon occurs due to the electrostatic charge applied to the particles and the conductive properties of the object being coated. Figures 6.3 (-6 kV - -2 kV and +2 kV - +6 kV) illustrate a higher concentration of particles close to the upper surface of the charged electrode. When a positive potential is applied, negatively charged particles are electrostatically precipitated onto the bottom surface of the electrode. The density of electrons in the upper region of the electrode is relatively low, owing to their significantly smaller mass—five orders of magnitude lower than that of positive ions—thereby reducing the force required by the electric potential to capture the particles. Negatively charged particles that escape the wire- mesh experience the wrap-around effect, where electrostatic forces guide their deposition onto the top surface of the electrode.

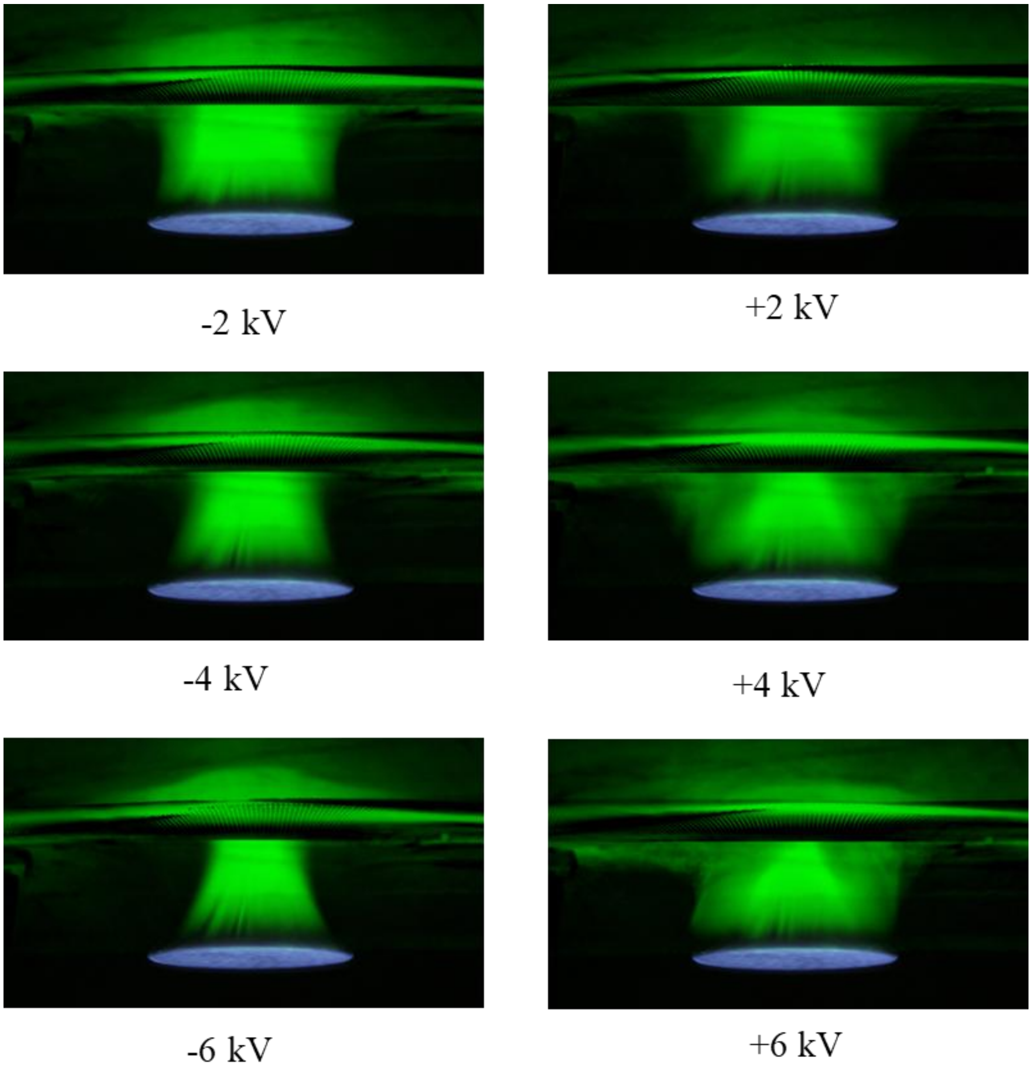

Figure 6.3. Time-averaged laser scattering at positive and negative potentials shows a distinct concentration of particles near the vicinity of the electrode.

In contrast, the positively charged species (ions), being heavier, contribute to an increase in the overall mass of the particles and agglomerates moving toward the negatively charged electrode. The excess momentum of the particles prevents a significant portion from depositing on the bottom surface and escaping through the pores of the electrode. However, due to the wrap-around effect, the particles' velocity decreases as they move across the electrode, resulting in a high-density cloud of particles lingering in close vicinity to the electrode's top surface.

As a result of particle charging by charged species in the presence of an external electric field, a wrap-around effect is observed. The effect is profound in the negative potential regime as a result of a higher concentration of particles escaping through the wire mesh electrode. Using a three-dimensional (3D) substrate may enhance particle collection efficiency when a negative potential is applied, providing improved surface interaction for particle capture.

6.2.2 Time-averaged intensity upstream of the electrode

Figures 6.4 and 6.5 show the mean scattering intensity of the flame-generated particle cloud upstream and downstream of the semi-permeable electrode respectively. The mean intensity of the scattered light by the flame-generated particle cloud upstream of the electrode shows a relatively uniform trend. The maximum variation across the range of electric potentials is 6 - 8 % from the average mean intensity. Since the scattering intensity shows little variation, the temperature and particle concentration profiles throughout the voltage range remain stable. It is seen that the application of the electric field and the formation of space charge within the flame volume does not affect the chemical kinetics at the flame front. As a result of the uniform particle concentration profile upstream of the electrode, the variations in the mean intensity downstream depend directly on the reduction in particle density due to the coating of the electrode.

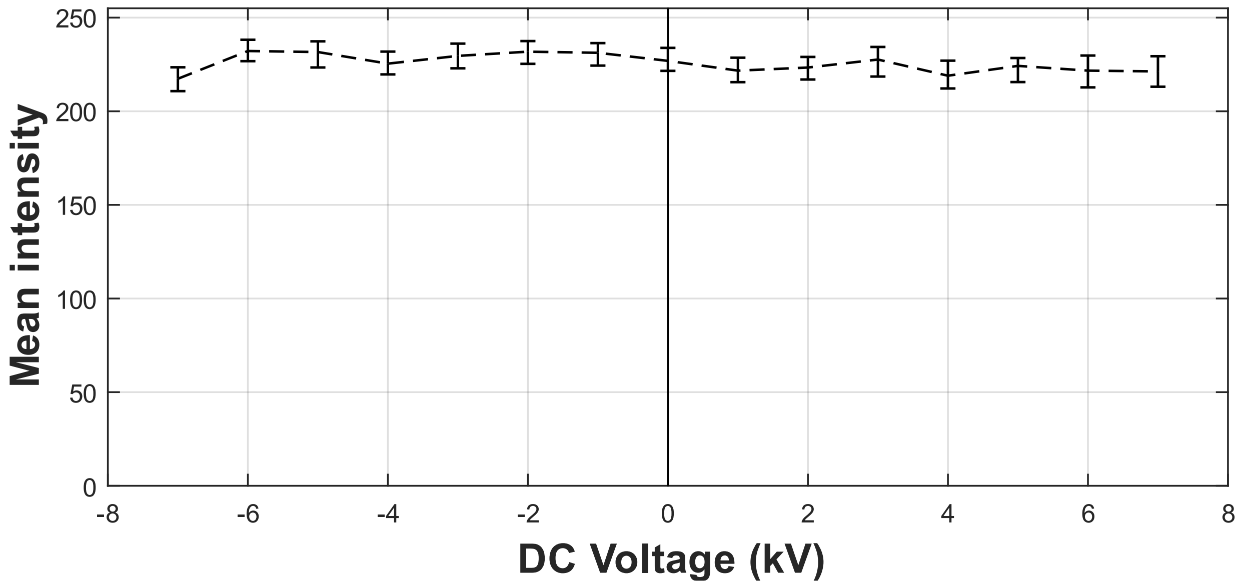

Figure 6.4. Mean intensity of the light scattered by the flame-generated particle cloud (upstream of the semi-permeable electrode).

6.2.3 Time-averaged intensity downstream of the electrode

Figure 6.5 shows the normalized mean intensity for the light scattered by the flame-generated particles downstream of the electrode under the influence of an external electric field. The mean intensity of the scattered light in the presence of flame-generated particles is normalized by the mean intensity measured in the absence of the particles in the test section. The measurement of scattered light intensity downstream of the electrode shows a sharp decrease in mean intensity as the polarity of the electrode is changed from negative to positive. The decrease in mean intensity is a result of the improved collection efficiency of the electrode as discussed in Chapters 3 and 4. The increase in collection efficiency results in the reduction of the particle concentration downstream of the electrode. A decrease in particle cloud density leads to a reduction in measured intensity value. Figure 6.5 follows a normalized intensity trend that is opposite to that of the yield of the particles. There is a 5-to-6-fold increase in the mean intensity for the negative potential compared to the positive potential. This observation directly relates to the 5-to-6-fold increase in yield for the positive potential compared to the negative potential.

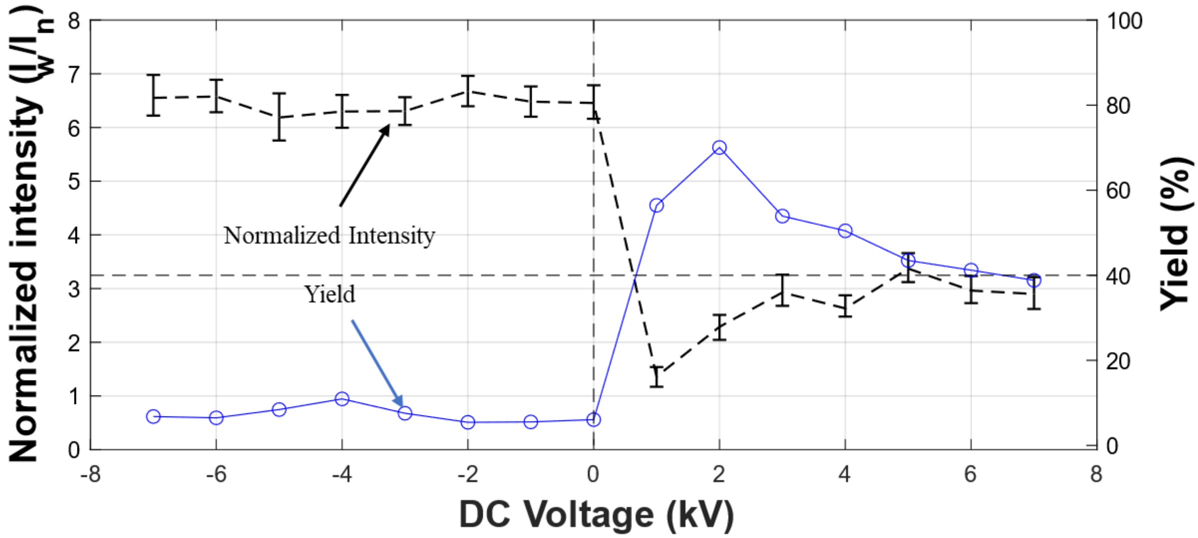

Figure 6.5. Normalized mean intensity of the light scattered by the flame-generated particle cloud downstream of the semi-permeable electrode superimposed on the yield of particles.

The charging of flame-generated particles within the flame volume, influenced by an external electric field, impacts their deposition on the electrode. Due to the higher charging efficiency of the negative charge carriers, there is a decrease in the particle density downstream of the electrode under the influence of a positive potential compared to a negative potential. This is inversely related to the yield of the particles calculated in Chapter 4. A wrap-around effect is observed due to the electrostatic force applied to the charged particles by the electrode. As a result, a high-density particle cloud is present in the downstream vicinity of the electrode.

Chapter 7: Numerical modeling of 1-dimensional premixed burner stabilized flame

To understand the effects of flame conditions on the electrical characteristics of the flame, experimental measurements of the positive and negative charge carrier concentration were performed using Langmuir probes (Calcote, 1957, 1961; Calcote et al., 1955). Following this, multiple studies formulated chemical pathways for the formation of charge carriers (Semenov et al, 1970). The rate constants, reaction mechanisms, and concentration of charged species in premixed methane flames at fuel-rich and lean conditions were studied (Goodings et al., 1979a, 1979b). As a result, the predictions of positive and negative charge carriers were performed by solving the governing, and transport equations (Pedersen et al., 1993; Speelman, de Goey, et al., 2015; Speelman et al., 2015).

Hexamethyldisiloxane (HMDSO) is used in the current study as the precursor for the formation of silica nanoparticles. Multiple experimental studies have been performed on the decomposition of HMDSO to SiO_2 (Li et al., 2016; Moussawi et al., 2021; Pfuch et al., 2006; Wegner et al., 2004; Yue et al., 2013). Initially, a 12-reaction mechanism was proposed and later a reduced 8-reaction scheme was studied (Chagger et al., 1996; Yeh et al., 2001b). The pyrolysis of HMDSO was investigated to understand the most probable paths for the decomposition (Almond et al., 2009). Studies were also conducted to understand the decomposition of HMDSO and the formation of silica through sub-mechanisms (Chrystie et al., 2019; Feroughi et al., 2017). In the current study, the HMDSO decomposition along with charged species reaction mechanism is added to the GRI-Mech 3.0 reaction mechanism to understand the gas phase formation and consumption of the Si major species before the nucleation of nanoparticles in the methane-air flame (Chrystie et al., 2019; Janbazi et al., 2019; Smith et al., 1999). The updated mechanism is used to understand the effects of flame conditions on the temperature, flame velocity, and concentration of charged species of the premixed burner stabilized flames.

7.1 Flame model

Cantera, an open-source software is employed to model the 1-D burner stabilized flame on the Python platform. The program solved a system of governing equations to predict the temperature, flame velocity, and density of the neutral and charged species.

7.1.1 Precursor and Ion Reaction Mechanisms

The reactions used in the current model consist of the chemistries of both neutral and charged species. The current study adopted the HMDSO decomposition mechanism from (Chrystie et al., 2019; Janbazi et al., 2019). As HMDSO contains carbon, the decomposition of the precursor was integrated into the GRI-Mech reaction mechanism. The ion and electron reactions are then added to the mechanism to predict the ion concentrations in the flame. The overall combustion of carbon-containing silica precursor is based on the Si-O-H sub-mechanism (Miller et al., 2012). The overall reaction mechanism is shown in Figure 7.1.

Table 7.1. List of HMDSO decomposition reactions. Units of $k_f = AT^b exp(-E_a/RT)$ are cm, s, mol, and cal.

Nr.	Reactions	A	b	E_a
1	HMDSO → $(CH_3)_3SiO + Si(CH_3)_3$	9.60×10^{07}	0	18,500
2	HMDSO → $(CH_3)_3SiOSi(CH_3)_2 + (CH_3)$	9.60×10^{05}	0	9800
3	$(CH_3)_3SiOSi(CH_3)_2$ + HMDSO → $(CH_3)_3SiOSi(CH_3)_2OSi(CH_3)_3 + Si(CH_3)_3$	3.60×10^{14}	0	9000
4	$(CH_3)_3SiOSi(CH_3)_2OSi(CH_3)_3 \rightarrow 2\ (CH_3)_3SiO + Si(CH_3)_2$	9.60×10^{12}	0	10,000
5	HMDSO + OH→ 2 $(CH_3)_3SiO$ + H	9.30×10^{08}	0	10,000
6	HMDSO + O_2 → 2 $(CH_3)_3SiO$ + O	8.60×10^{08}	0	10,000
7	HMDSO + HO_2 → 2 $(CH_3)_3SiO$ + OH	9.80×10^{08}	0	10,000
8	$(CH_3)_3SiOSi(CH_3)_2 + (CH_3)_3SiO \rightarrow (CH_3)_3SiOSi(CH_3)_2OSi(CH_3)_3$	3.60×10^{08}	0	10,000
9	$(CH_3)_3SiOSi(CH_3)_2 \rightarrow (CH_3)_2SiO + Si(CH_3)_3$	3.60×10^{06}	0	23,650
10	$(CH_3)_3SiOSi(CH_3)_2 + CH_3 \rightarrow Si(CH_3)_2OH + (CH_3)_3SiCH_2$	3.60×10^{14}	0	10,000

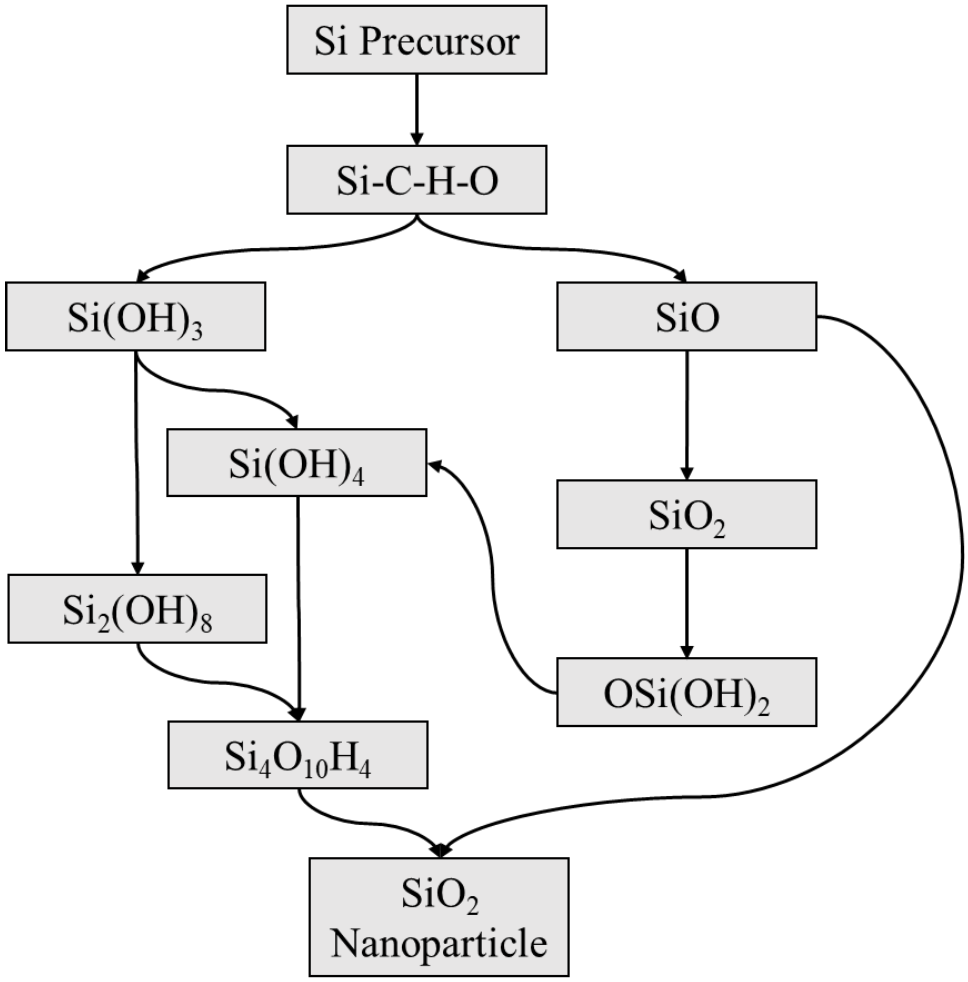

Figure 7.1. The proposed pathways for the reduced reaction mechanism illustrate the formation of intermediate SiO clusters and the formation of SiO_2 nanoparticles. Si-C-H-O and Si-O-H indicates the sub-mechanisms involved (Chrystie et al., 2019; Janbazi et al., 2019).

Table 7.2. List of charge carrier reactions. Units of $k_f = AT^b exp(-E_a/RT)$ are cm, s, mol, and cal.

Nr.	Reactions	A	b	Ea
1	$CH + O \Rightarrow HCO^+ + E$	2.51E+11	0	1700
2	$HCO^+ + H_2O \Rightarrow H_3O^+ + CO$	1.51E+15	0	0
3	$H_3O^+ + E \Rightarrow H_2O + H$	2.29E+18	-0.5	0
4	$H_3O^+ + E \Rightarrow OH + H + H$	7.95E+21	-1.4	0
5	$H_3O^+ + E \Rightarrow H_2 + OH$	1.25E+19	-0.5	0
6	$H3O^+ + E \Rightarrow O + H_2 + H$	6.00E+17	-0.3	0

This initiates the secondary charge transfer and recombination reactions leading to the formation of charged species in the flame (Prager, Riedel, & Warnatz, 2007). The ion transport mechanisms were studied by (Han, Belhi, Bisetti, & Sarathy, 2015).

7.2 Flame model validation

The model is validated with the Wortberg flame condition (Wortberg, 1965), where the concentration of ions and temperature are measured. A distance of 0.02 m was chosen as the height above the burner. The inlet flame temperature is set as 600 K, and the methane-air equivalence ratio is set at ϕ = 0.513. The grid points are spaced finely closer to the reaction zone and coarser as they move closer to the outlet. The inlet velocity is set to 10 cm/s.

The model predicts a maximum flame temperature of 1490 K as shown in Figure 7.1. The modeled value matches well with the temperature estimated by the Wortberg's flame of 1500 K. Figure 7.1 shows the temperature and the number density profiles of CH. The peak value of CH is considered as the location of the flame front. A dashed line is used to indicate the location of the CH peak or the flame front. Figure 7.2 shows the concentration of the major charged species (H_3O^+ and electrons). A peak in the number density is observed at the location of the flame front corresponding to the region of chemical reactions. The HCO^+ concentration is smaller than the H_3O^+ and electron concentration by three orders of magnitude at the flame front.

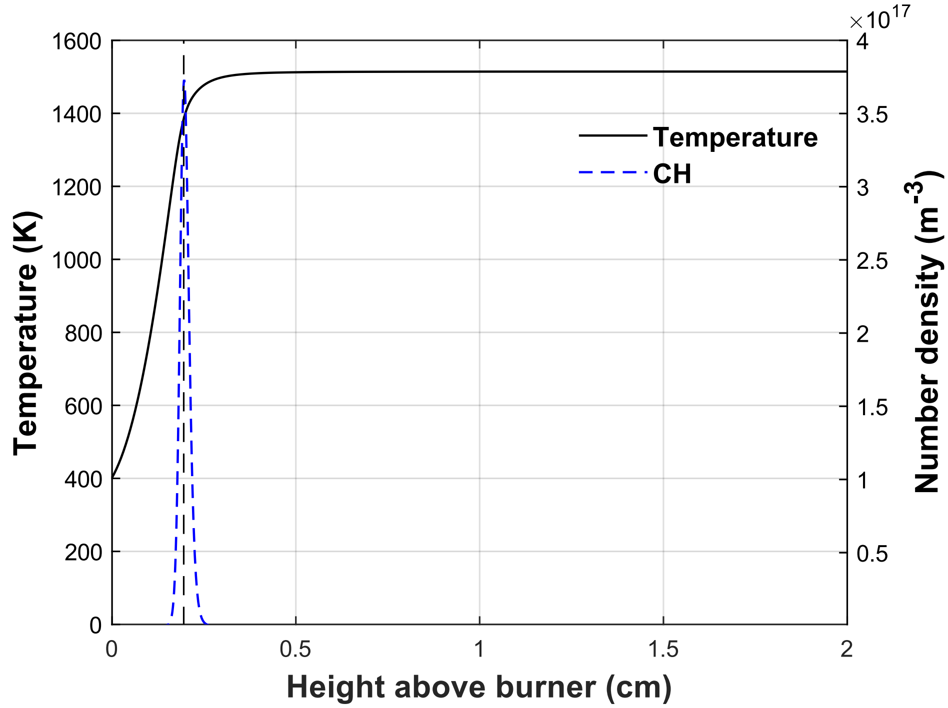

Figure 7.2. Temperature and CH profiles of the validation model based on the Wortberg's flame condition of ϕ = 0.513.

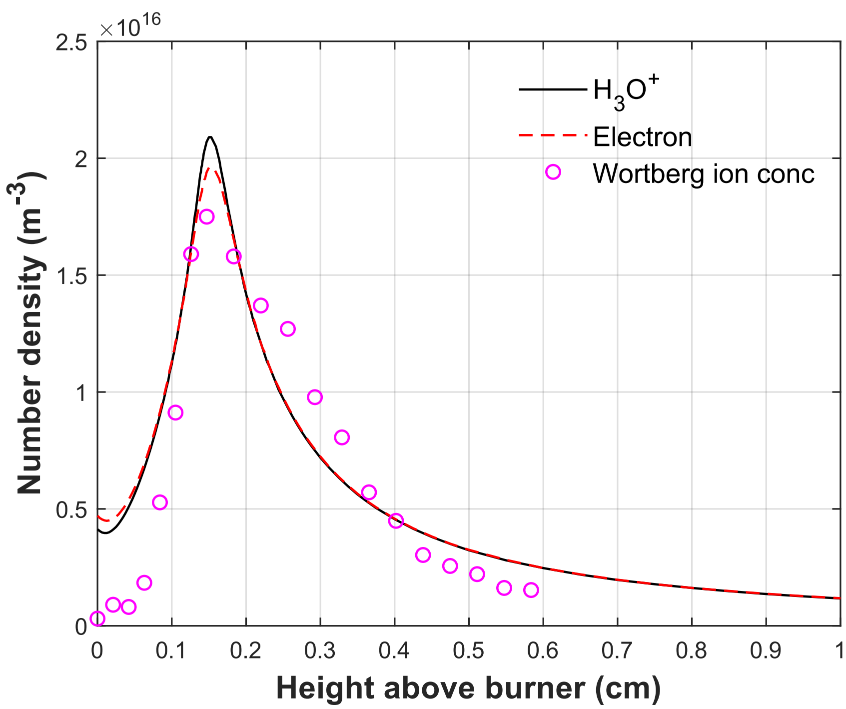

Figure 7.3. Comparison of charged species concentration estimated by the 1-D flame model and Wortberg's flame condition ϕ = 0.513.

7.3 Effect of inlet conditions on unseeded and seeded flame characteristics

The variation in the flame temperature, the concentration of positive and negative charge carriers, and the mole fraction of major species involved in HMDSO breakdown are studied here. The velocity of the premixed reaction mixture is adjusted within the range of 7 to 9 cm/s. The flame equivalence ratio is set between 0.7 and 0.9. The distance between the burner surface to the outlet is set at 3.5 cm (width = 0.035 m). Cantera determines the optimal number of grid points based on the specified width. The created mesh is finer near the burner surface and reaction zone and grows coarser as the solution approaches the outlet region. The velocity of the reactive gas mixture and its equivalence ratio are varied. The first part of the study involved changing the flame conditions to observe its effect on the temperature and charge carrier concentration in an unseeded flame, i.e. the precursor flow rate is set to zero. The second part of the study involves the introduction of precursor flow into the reactive gas mixture. The variations in temperature and charge carrier concentrations are studied at constant flame conditions of equivalence ratio $\phi = 0.9$ and gas mixture velocity v= 8 cm/s. Variation in mole fractions of major species of the HMDSO decomposition are observed by changing the precursor flow rate between 0.03 g/min to 0.09 g/min. The temperature and CH mole fraction profiles are shown in Figure 7.4. The peak of the CH profile is the location of the flame front.

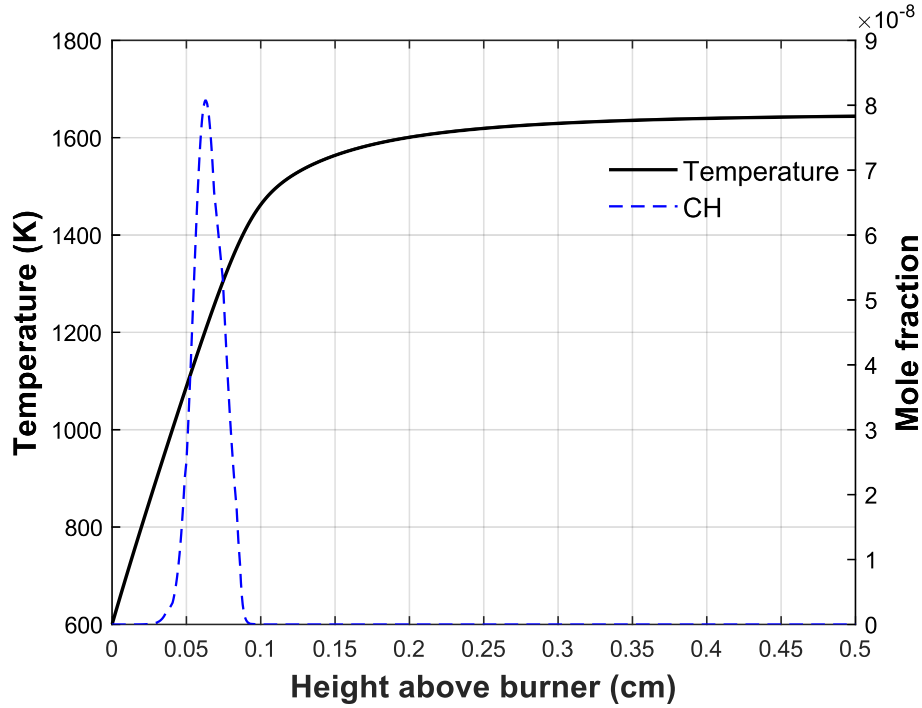

Figure 7.4. Temperature and CH profiles at an equivalence ratio of ϕ = 0.9 and velocity of 8 cm/s.

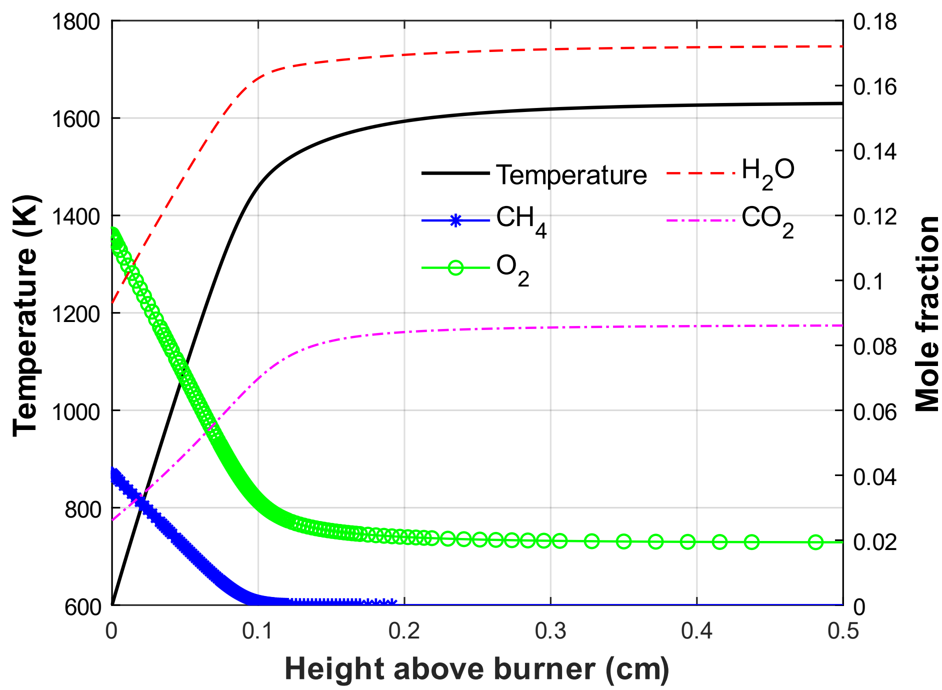

Figure 7.5. Temperature and major species mole fraction at a constant velocity of 8 cm/s and equivalence ratios ϕ = 0.9.

7.3.1 Unseeded flame

Figure 7.5 shows the temperature and the mole fractions of the major reactants and products for an unseeded flame at equivalence ratio $\phi = 0.9$ and gas mixture velocity v = 8 cm/s.

7.3.1.1 Flame temperature

Figure 7.6 shows the comparison of temperature at a constant velocity v = 8 cm/s with varied equivalence ratios of 0.7, 0.8, and 0.9. It is observed that an increase in the equivalence ratio increased the temperature of the flame. The temperature rise is attributed to the increase in the fuel-to-air ratio in the premixed gas mixture. A higher flow rate of fuel results in a higher energy release in the form of heat which increases the temperature. Similarly, an increase in the velocity of the premixed gases gives rise to higher temperatures. This is attributed to the higher flow rates of fuel resulting in a reaction releasing higher energy (Figure 7.7).

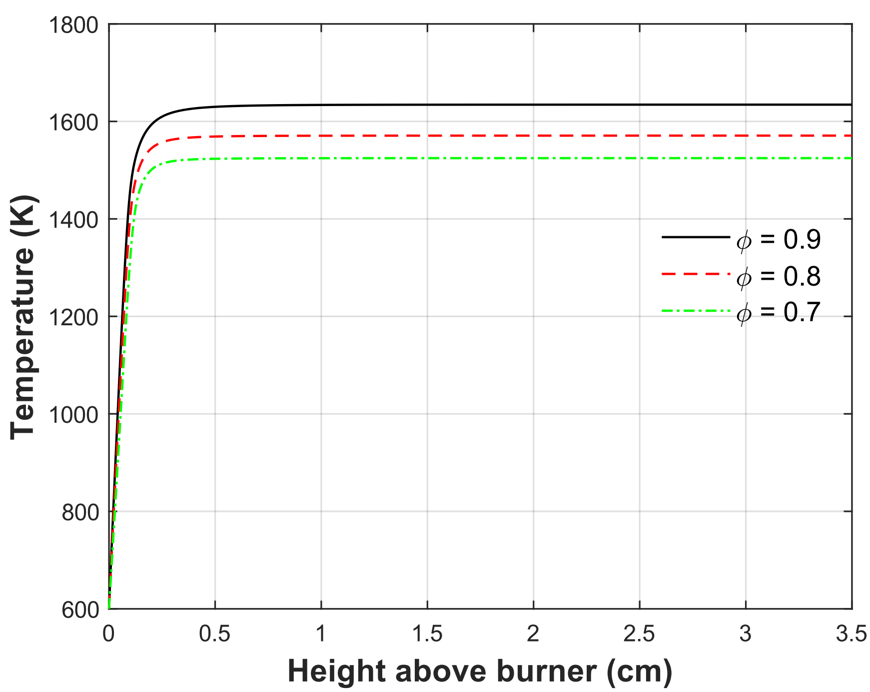

Figure 7.6. Comparison of temperature at a constant velocity of 8 cm/s with varying equivalence ratios.

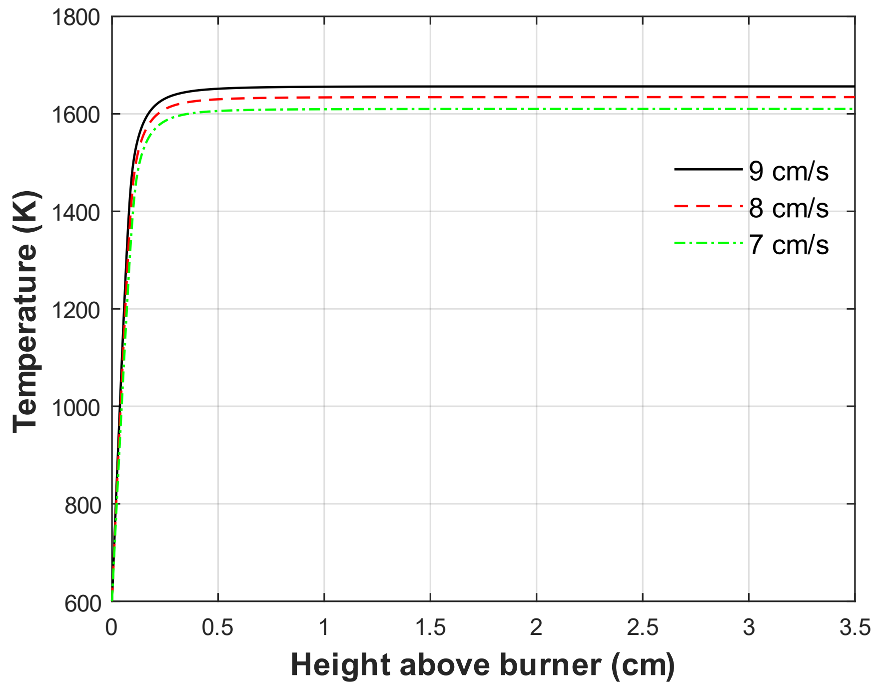

Figure 7.7. Comparison of temperature at a constant equivalence ratio $\phi = 0.9$ with varying velocity.

7.3.1.2 Charge carrier concentration

The concentration of positive and negative charge carriers for a premixed burner stabilized flat flame is plotted in Figures 7.8 and 7.10 for different equivalence ratios at a constant velocity of 8 cm/s. It is observed that an increase in the equivalence ratio from 0.7 to 0.9 results in an increase of the ion concertation. The increase in concentration is attributed to the increase in the production of the radicals in the flame front. Due to higher fuel and airflow rates, there is an increase in the concentration of charge carriers formed by chem-ionization mechanism.

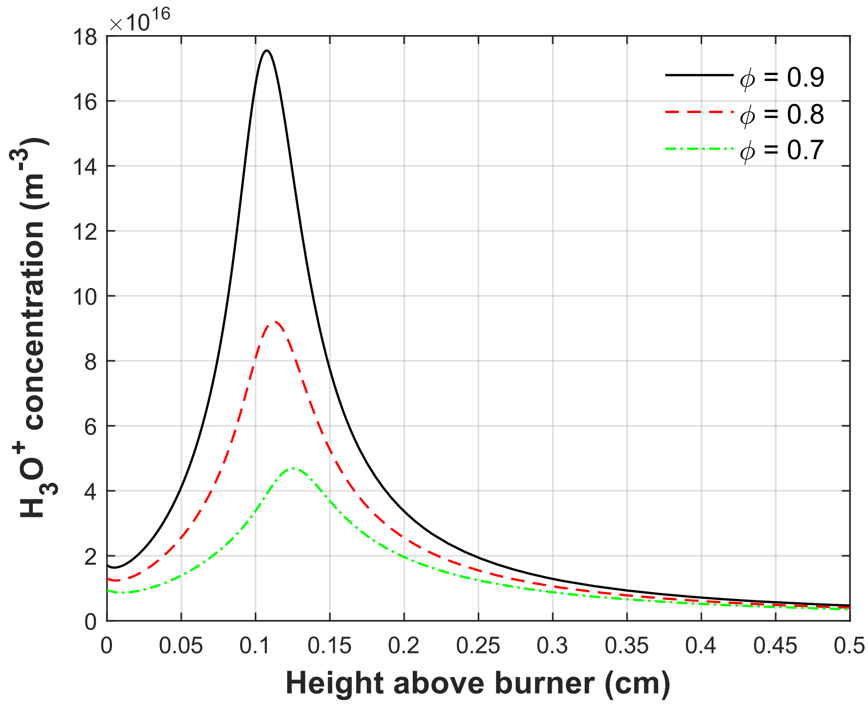

Figure 7.8. Comparison of H_3O^+ concentration at a constant velocity of 8 cm/s with varying equivalence ratios.

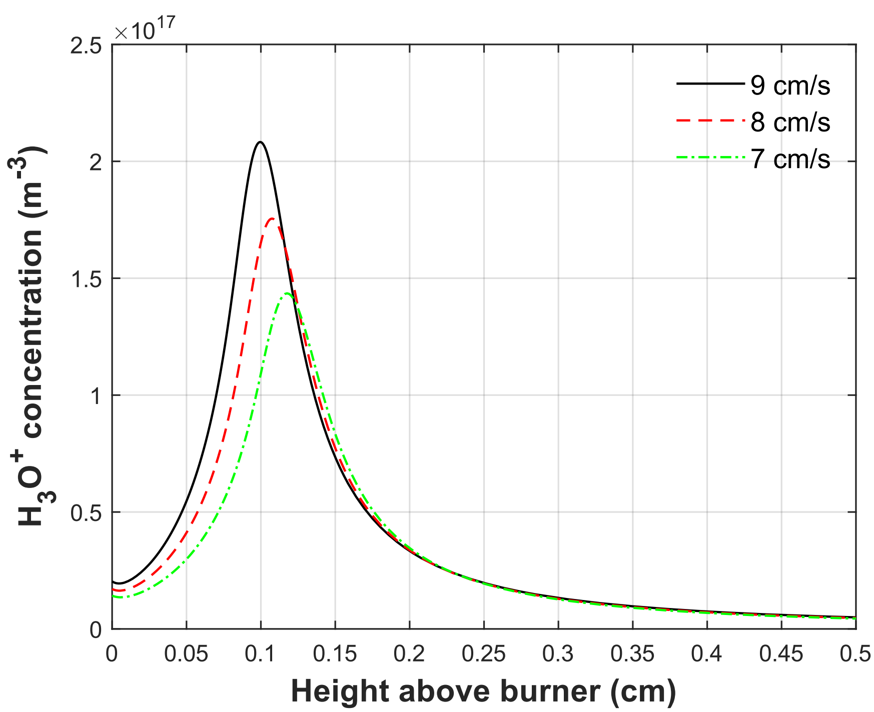

Figure 7.9. Comparison of H_3O^+ concentration at a constant equivalence ratio ϕ = 0.9 with varying velocity.

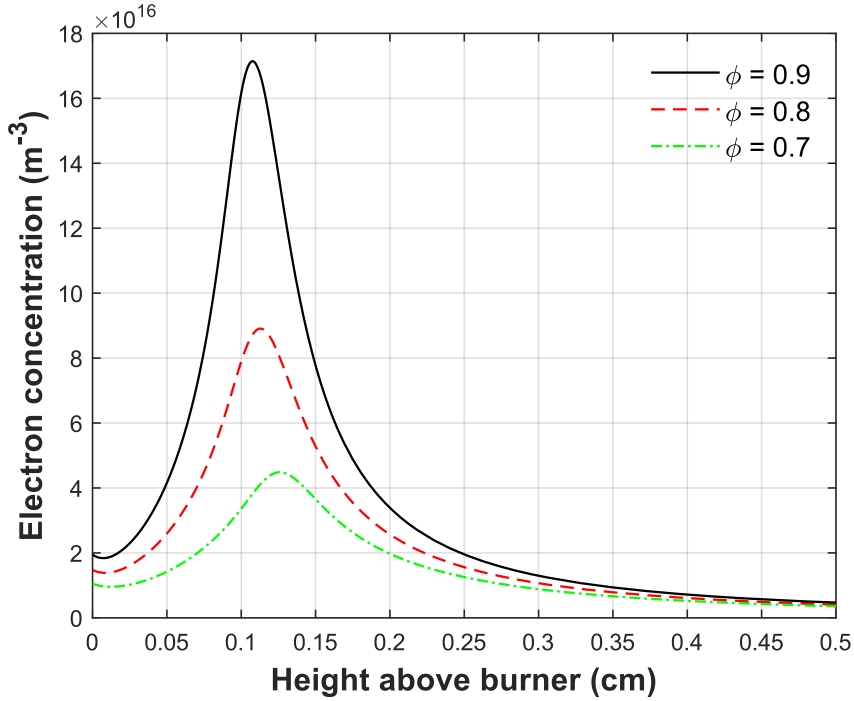

Figure 7.10. Comparison of electron concentration at a constant velocity of 8 cm/s with varying equivalence ratios.

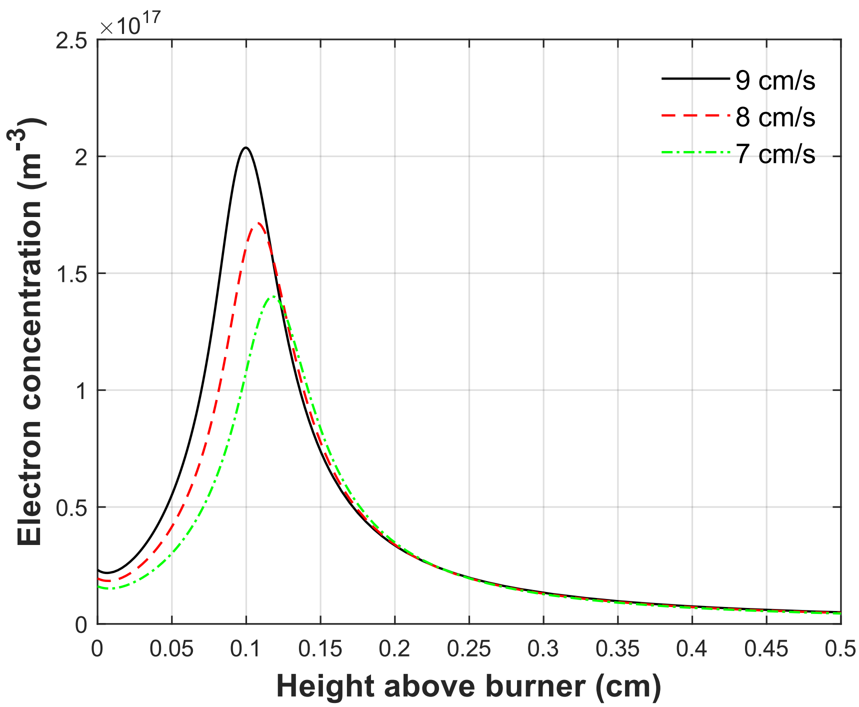

Figure 7.11. Comparison of electron concentration at a constant equivalence ratio ϕ = 0.9 with varying velocity.

Similar to the effect of the equivalence ratio, a change in reactive mixture flow velocity also affects the positive and negative charge carrier concentrations (Figures 7.9, and 7.11). When the velocity of the premixed reactive mixture is increased the rate of chemi-ionization increases. The increase in chemi-ionization rate results in the increase in new radical formation leading to higher concentrations of positive and electrons.

The rise in the concentration of charge carriers due to the increase in equivalence ratio or velocity results in higher saturation currents, as discussed in Chapter 3. This gives rise to the higher measured current in both the unseeded and flame-generated particle-seeded flames. The greater the number of charged carriers, the higher the measured current.

7.3.2 Effect of precursor on flame characteristics

The inlet conditions are set at a constant equivalence ratio $\phi = 0.9$ and gas mixture velocity v= 8 cm/s. The variation in temperature, velocity and ion concentration is predicted by introducing a precursor flow rate of 0.03g/min. The change in mole fractions of the major species is also analyzed by increasing the flow rates to 0.06 g/min and 0.09 g/min.

7.3.2.1 Flame temperature and velocity

Figure 7.12 shows the difference in temperature for seeded and unseeded flames. The decomposition of HMDSO ($C_6H_{18}OSi_2$) is an exothermic process due to the formation of hydrocarbons such as CH_3 and CH_4 (Chen et al., 2020). The enthalpy of formation for the major species involved in the breakdown of Si-precursors suggests an overall exothermic process (Janbazi et al., 2019). Due to the exothermic decomposition reactions of HMDSO in seeded flames, the temperature is observed to be higher when compared to the unseeded flames. Since the precursor constitutes only 4–5% of the fuel mass, it does not cause a significant temperature increase (20-30 K). Figure 7.13 shows the change in velocity due to the introduction of precursor flow into the reaction mixture. The additional mass of the precursor results in a minor increase in the overall volume flow of the reaction mixture gases resulting in a minor increase in product gas velocity as observed.

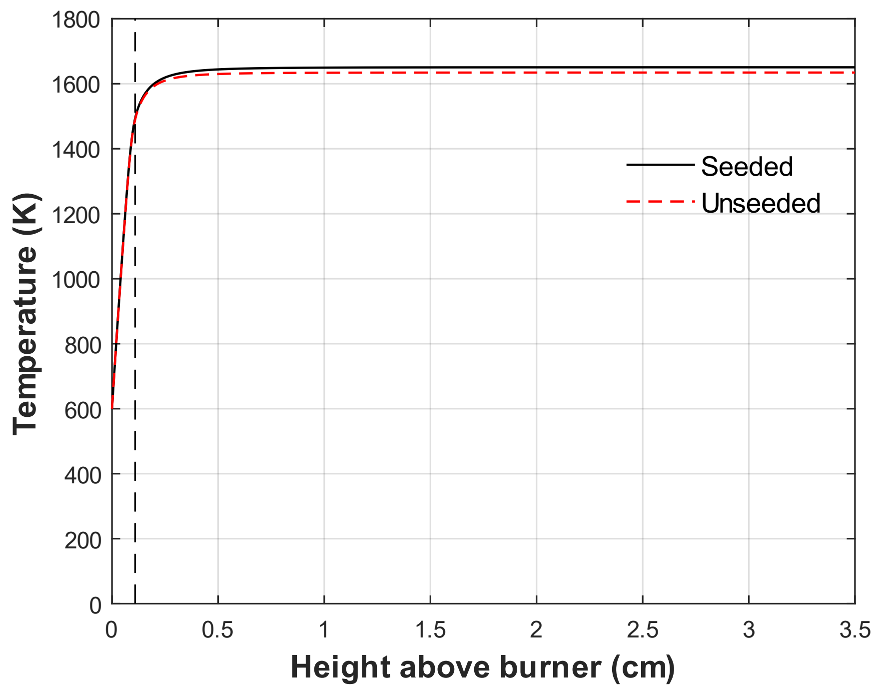

Figure 7.12. Comparison of temperature for a seeded and an unseeded burner stabilized flame at a constant equivalence ratio ϕ = 0.9 and gas mixture velocity v= 8 cm/s.

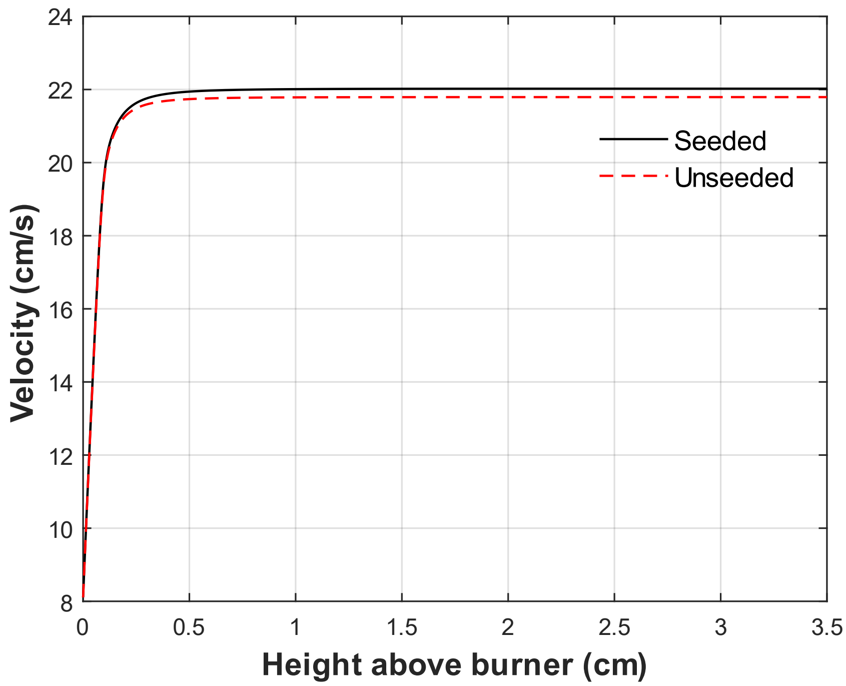

Figure 7.13. Comparison of velocity for a seeded and an unseeded burner stabilized flame at a constant equivalence ratio ϕ = 0.9 and gas mixture velocity v= 8 cm/s.

Therefore, it is observed that the addition of a precursor to the reaction mixture does not significantly increase the flame temperature or velocity. This suggests that the precursor flow does not affect the flame characteristics when compared to an unseeded flame with the same conditions.

7.3.2.2 Charge carrier concentration

The GRI-Ion reaction mechanism is added to the existing HMDSO kinetics to evaluate the concentration of charge carriers. Figures 7.14 and 7.15 show the ion and electron concentration of unseeded and seeded burner stabilized flames at a constant equivalence ratio ϕ = 0.9 and gas mixture velocity v= 8 cm/s. The charge carrier concentration increases with the introduction of a precursor into the reaction gas mixture. The major elements responsible for the production of charge carriers in the flame front are C, H, O, and e^- in the form of HCO^+, H_3O^+, and free electrons. The introduction of HMDSO marginally increases the mole/mass fractions of these elements in the reaction mixture, which results in a slight increase in the concentration of charge carriers in the product gases.

Figures 7.14 and 7.15 show the addition of precursor to the reaction mixture does not increase the charge carrier number density significantly. Thus, the electrical characteristic of the seeded flame is marginally varied compared to the unseeded flame.

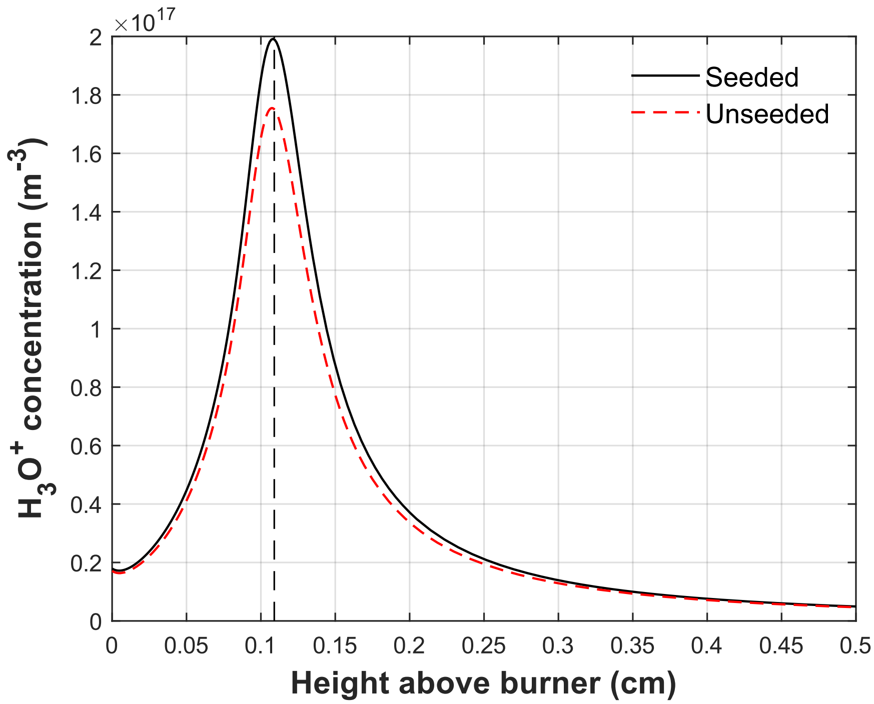

Figure 7.14. Comparison of H_3O^+ concentration for a seeded and an unseeded burner stabilized flame at a constant equivalence ratio ϕ = 0.9 and gas mixture velocity v= 8 cm/s.

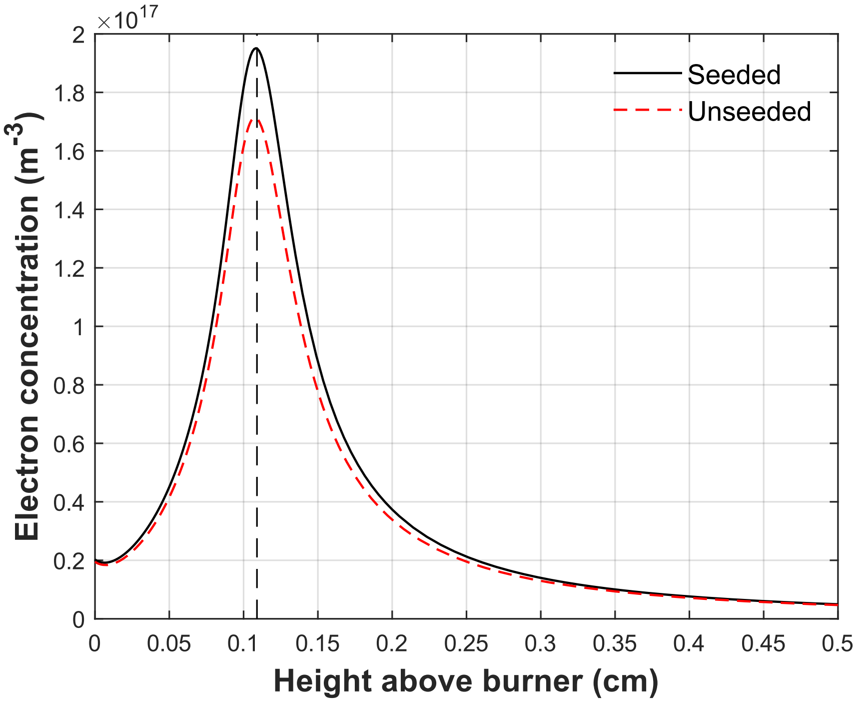

Figure 7.15. Comparison of electron concentration for a seeded and an unseeded burner stabilized flame at a constant equivalence ratio ϕ = 0.9 and gas mixture velocity v= 8 cm/s.

7.3.3 Formation of nanoparticles

The HMDSO mechanism focuses on the chemical kinetics of the gas phase formation and consumption of major species that occur well before nanoparticle nucleation in the flame. The major species are SiO_2 (g), $Si(OH)_4$, and $Si_4O_{10}H_4$. The formation and subsequent consumption of $Si(OH)_4$, and the formation of $Si_4O_{10}H_4$ clusters are hypothesized as the primary pathways in the silica nanoparticle synthesis (Janbazi et al., 2019). Figure 7.1 shows the breakdown pathway for a Si-precursor undergoing flame synthesis.

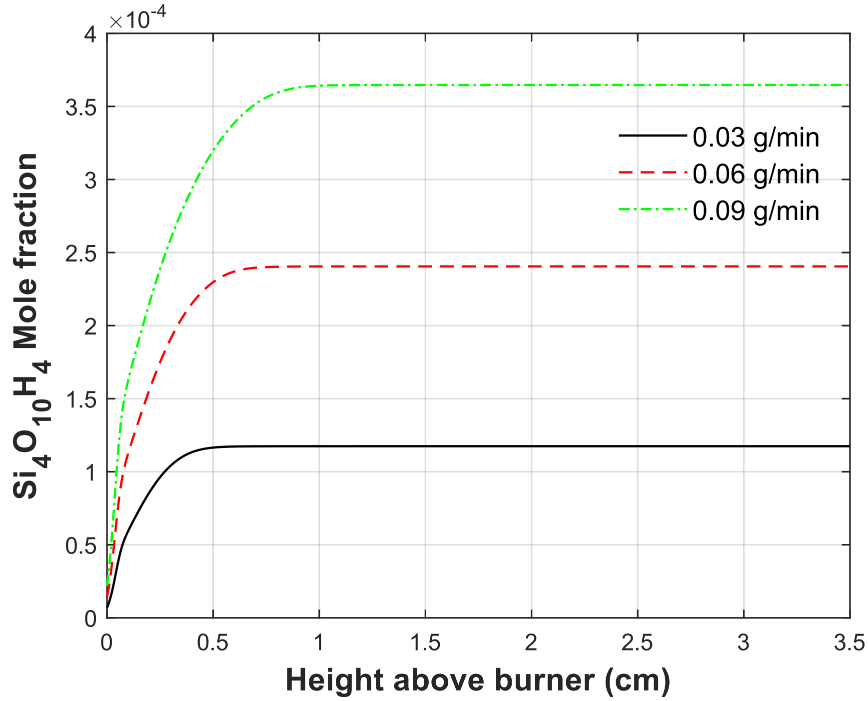

Figure 7.16. Comparison of $Si_4O_{10}H_4$ concentration at a constant equivalence ratio φ = 0.9 and gas mixture velocity v= 8 cm/s with varying precursor flow rate.

The variation in $Si_4O_{10}H_4$ mole fractions concerning the increase in precursor flow rate (0.03 g/min to 0.09 g/min) is shown in Figure 7.16. The increase in the mole fraction of the precursor led to the rise in the mole fractions of the major Si-species leading to the formation of SiO_2 nanoparticles. An increase in the mole fraction of $Si_4O_{10}H_4$ which is the forerunner to the formation of SiO_2 nanoparticles, results in an improved production rate of SiO_2 nanoparticles. This is attributed to a higher concentration of SiO_2 vapor (supersaturation) in and downstream of the flame front. Figures 7.17 show the mole fractions of SiO_2 (g), $Si(OH)_4$, and $Si_4O_{10}H_4$ and their interaction with the formation of charged species at a burner stabilized flame condition of equivalence ratio $\phi = 0.9$, gas mixture velocity v= 8 cm/s. The plot visualizes the formation of the major species involved in the nucleation of SiO_2 nanoparticles. SiO_2 (g) and $Si(OH)_4$ are observed to peak at the flame front, after which they are consumed to form $Si_4O_{10}H_4$. $Si_4O_{10}H_4$ peaks at approximately 0.4 cm from the burner surface, that is $Si_4O_{10}H_4$ continues to be produced beyond the flame front.

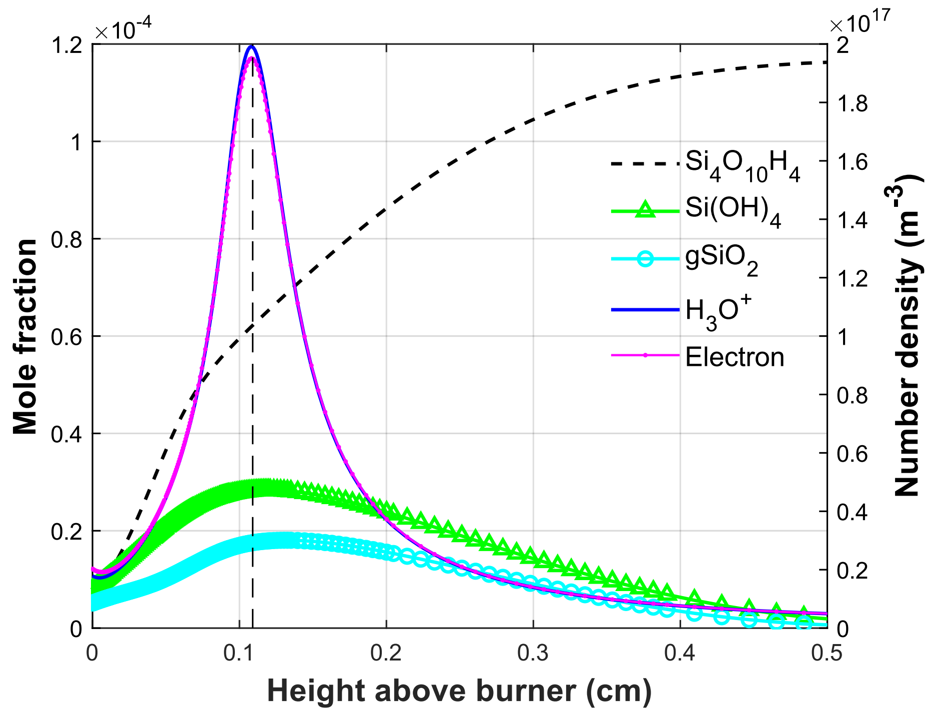

Figure 7.17. Profiles of mole fractions of charged and neutral Si species.

Figure 7.17 also shows the formation and consumption of charged species in the flame front, with their peak coinciding with the flame front. The charged species in the absence of an external electric field undergo recombination leading to deteriorating concentrations. The location of the peaks of charged species and $Si_4O_{10}H_4$ suggests that their respective formation and eventual consumption do not affect each other. This, suggests that the chemistry of HMDSO decomposition and formation of SiO_2 are not affected by the presence of charged species in the flame volume, and the application of external electric fields affects the charging of the nucleated particles.

Chapter 8: Conclusions and Future Work

8.1 Conclusions

The influence of external electric fields on flame synthesis of silica nanoparticles using flat, burner-stabilized, premixed flames was studied experimentally and numerically.

1. A significant decrease in current values was observed in seeded flames. For positive polarity, monotonic growth and saturation of the current were replaced by a complex pattern with a characteristic peak. For negative polarity, the current reduced to zero and then demonstrated exponential growth as voltage was reduced further. In the studied configuration the characteristic peak under the influence of a positive electric field appeared at +2 kV (+0.6 kV/cm). For the negative potential the exponential increase in current was observed at -8 kV (-2.3 kV/cm).
2. In seeded flames, the particle build-up on the electrode surface caused a gradual reduction of the current with respect to time ultimately reaching zero. In the experimentally studied configuration the current reached a value of zero at approximately 1000 s at 3 kV (0.85 kV/cm).
3. The phenomenon of the back discharge was observed. The discharge was initiated and sustained by the flame current accumulating on the surface of the high-resistivity SiO_2 layer deposited on the electrode.
4. In unseeded flames, the back discharge on the coated electrode caused a slight increase in current for the positive polarity and a multifold increase in current for the negative polarity. Increase in equivalence ratio, velocity, and deposition time led to an increase in flame current.
5. For positive polarity, the silica nanoparticle yields increased multifold compared to negative and zero polarity. In the studied configuration a 7 to 10 times increase in the yield

was observed. At a constant voltage the weight of particles collected per minute remained relatively constant

6. TEM images showed similar average particle diameter across the entire electric potential range. Application of a positive polarity resulted in the narrowing of the size-distribution, attributed to electrostatic repulsion of negatively charged particles. An average particle diameter of 11 nm is measured for the current configuration. Size-distributions showed 80% of the particles within 8 and 12 nm for the positive polarity and 85% within 8 and 14 nm for the negative polarity.
7. Rayleigh scattering imaging showed a uniform intensity upstream of the electrode. For positive polarity downstream of the electrode, the intensity decreased compared to zero and negative polarity. Scattering intensity measurements followed a similar trend to that of the yield. For the experimentally studied conditions the measured intensity downstream of electrode decreased 7-fold for positive polarity compared to zero and negative polarity.
8. The predicted profiles of charged species and $Si_4O_{10}H_4$ suggested that charged species formation in the flame front was not affected by the silica particle formation downstream. The application of external electric fields affected the transport of ions and electrons and charging of the formed nanoparticles.
9. Overall, it was shown that electric fields can be used for efficient control of particle deposition rate and optimization of particle yield of the deposited layers.

8.2 Future work

A comprehensive investigation into the influence of solid substrate structure and material on the yield and collection efficiency of flame-generated particles is necessary. Wire mesh electrodes with wire diameters of 0.12" and 0.09" were employed to evaluate the impact of reduced porosity on collection efficiency. However, the electrode's wire size led to significant thermal expansion, causing a reduction in the height above the burner (HAB) and introducing non-uniformities in the electric field across the flame volume. To mitigate these issues, alternative materials with lower thermal expansion coefficients should be explored for use in the current setup. Additionally, Investigation into the effect of electrode's structure on the wraparound behavior of charged particles is required. Moreover, the reaction mechanism involving HMDSO, and ions requires optimization to improve computational efficiency and address issues with non-converging solutions.

REFERENCES

A. Mizuno. (2000). Electrostatic precipitation - Dielectrics and Electrical Insulation. *IEEE Transactions on Dielectrics and Electrical Insulation*, *7*(5).

Adachi, M., Kousaka, Y., & Okuyama, K. (1985). Unipolar and bipolar diffusion charging of ultrafine aerosol particles. *Journal of Aerosol Science*, *16*(2), 109–123. https://doi.org/10.1016/0021-8502(85)90079-5

Aiping, Y., Victor, C., & Jiujun, Z. (2013). *Electrochemical Supercapacitors for Energy Storage and Delivery*. Taylor & Francis.

Akhtar, M. K., Vemury, S., & Pratsinis, S. E. (1994). The role of electrolytes during aerosol synthesis of TiO2. *Nanostructured Materials*, *4*(5), 537–544. https://doi.org/10.1016/0965-9773(94)90061-2

Almond, M. J., Becerra, R., Bowes, S. J., Cannady, J. P., Ogden, J. S., Young, N. A., & Walsh, R. (2009). A mechanistic study of the low pressure pyrolysis of linear siloxanes. *Physical Chemistry Chemical Physics*, *11*(40), 9259–9267. https://doi.org/10.1039/b910549b

Altendorfner, F., Beyrau, F., Leipertz, A., Hammer, T., Most, D., Lins, G., & Branston, D. W. (2010). Technical feasibility of electric field control for turbulent premixed flames. *Chemical Engineering and Technology*, *33*(4), 647–653. https://doi.org/10.1002/ceat.200900625

Andres, R. P., Averb, R. S., Brown, W. L., Brus, L. E., Goddard, W. A., Arthur Amos, I., … Brus R W Siegel, L. E. (1989). *Research opportunities on clusters and cluster-assembled matenals-A Department of Energy, Council on Materials Science Panel Report*. J. Mater. Res* (Vol. 4).

Aruna, S. T., & Mukasyan, A. S. (2008). Combustion synthesis and nanomaterials. *Current Opinion in Solid State and Materials Science*, *12*(3–4), 44–50. https://doi.org/10.1016/j.cossms.2008.12.002

Bailey, A. G. (1998). The science and technology of electrostatic powder spraying, transport and coating. *Journal of Electrostatics*, *45*(2), 85–120. https://doi.org/10.1016/S0304-3886(98)00049-7

Bautista, J. ., & Atkins, R. . (1991). THE FORMATION AND DEPOSITION OF SiO2 AEROSOLS OPTICAL FIBER MANUFACTURING TORCHES. *Microscope*, *22*(5), 667–675.

Bielański, A., Dereń, J., & Haber, J. (1957). Electric conductivity and catalytic activity of semiconducting oxide catalysts. *Nature*, *179*(4561), 668–669. https://doi.org/10.1038/179668a0

Bonnemain, B. (1998). Superparamagnetic agents in magnetic resonance imaging: Physicochemical characteristics and clinical applications. A review. *Journal of Drug Targeting*, *6*(3), 167–174. https://doi.org/10.3109/10611869808997890

Bradley, D., & Jamel, M. A. M. (1984). Attachment of flame chemielectrons to inert, fine particles. *Combustion and Flame*, *58*(2), 115–124. https://doi.org/10.1016/0010-2180(84)90087-7

Brande, W. T. (1814). The Bakerian Lecture : On Some New Electro-Chemical Phenomena. *Philosophical Transactions of the Royal Society of London*, *1*(104), 51–61.

Brown, R. C., & Eraslan, A. N. (1988). Simulation of ionic structure in lean and close-to-stoichiometric acetylene flames. *Combustion and Flame*, *73*(1), 1–21. https://doi.org/10.1016/0010-2180(88)90050-8

Calcote, H. F. (1957). Mechanisms for the formation of ions in flames. *Combustion and Flame*, *1*(4), 385–403. https://doi.org/10.1016/0010-2180(57)90001-9

Calcote, H. F. (1961). Ion production and recombination in flames. *Symposium (International) on Combustion*, *8*(1), 184–199. https://doi.org/10.1016/S0082-0784(06)80502-3

Calcote, H. F., & King, I. R. (1955). Studies of ionization in flames by means of langmuir probes. *Symposium (International) on Combustion*, *5*(1), 423–434. https://doi.org/10.1016/S0082-0784(55)80056-2

Calcote, Hartwell F, & Pease, R. N. (1951). Burner Flames in Longitudinal Electric Fields. *Industrial and Engineering Chemistry*, *43*(12), 12.

Chadha, U., Hafiz, M., Bhardwaj, P., Padmanaban, S., Sinha, S., Hariharan, S., … R, V. (2022). Theoretical progresses in silicon anode substitutes for Lithium-ion batteries. *Journal of Energy Storage*, *55*(PA), 105352. https://doi.org/10.1016/j.est.2022.105352

Chagger, H. K., Hainsworth, D., Patterson, P. M., Pourkashanian, M., & Williams, A. (1996). The formation of SiO2 from hexamethyldisiloxane combustion in counterflow methane-air flames. *Symposium (International) on Combustion*, *26*(2), 1859–1865. https://doi.org/10.1016/S0082-0784(96)80007-5

Changhui, YE Shulin, J. (2008). Synthesis, growth mechanism, and application of zinc oxide nanomaterials. Journal of material Science & Technology.

Chen, Q., Yan, L., Zhang, H., & Li, G. (2016). Electrical Characteristics, Electrode Sheath and Contamination Layer Behavior of a Meso-Scale Premixed Methane-Air Flame under AC/DC Electric Fields. *Plasma Science and Technology*, *18*(5), 569–576. https://doi.org/10.1088/1009-0630/18/5/21

Chen, Yugong, Huang, Y., & Zhou, M. (2020). Identification of decomposition reactions for HMDSO organosilicon using quantum chemical calculations, (February), 1–8. https://doi.org/10.1002/qua.26415

Chen, Yuping, Yang, G., Zhang, Z., Yang, X., Hou, W., & Zhu, J. J. (2010). Polyaniline-intercalated layered vanadium oxide nanocomposites - One-pot hydrothermal synthesis and application in lithium battery. *Nanoscale*, *2*(10), 2131–2138. https://doi.org/10.1039/c0nr00246a

Chrystie, R. S. M., Janbazi, H., Dreier, T., Wiggers, H., Wlokas, I., & Schulz, C. (2019). Comparative study of flame-based SiO2 nanoparticle synthesis from TMS and HMDSO: SiO-LIF concentration measurement and detailed simulation. *Proceedings of the Combustion Institute*, *37*(1), 1221–1229. https://doi.org/10.1016/j.proci.2018.07.024

Chung, S. L., Lim, W. M., Leong, C. O., & Yee, M. S. L. (2024). Optimisation Studies of Mesoporous Silica Nanoparticle as a Drug Carrier for Gemcitabine: Enhancing Therapeutic Effectiveness in Pancreatic Cancer. *Key Engineering Materials*, *977*, 155–162. https://doi.org/10.4028/p-pdci7g

D'Anna, A., Rolando, A., Allouis, C., Minutolo, P., & D'Alessio, A. (2005). Nano-organic carbon and soot particle measurements in a laminar ethylene diffusion flame. *Proceedings of the Combustion Institute*, *30*(1), 1449–1456. https://doi.org/10.1016/j.proci.2004.08.276

Di Stasio, S. (2000). Feasibility of an optical experimental method for the sizing of primary spherules in sub-micron agglomerates by polarized light scattering. *Applied Physics B: Lasers and Optics*, *70*(4), 635–643. https://doi.org/10.1007/s003400050872

Donald Arthur Becker. (1970). *Chemical interference and ionization in high temperature flames*.

Duan, H., Wu, X., Sun, T., Liu, B., Fang, J., Li, C., & Gao, Z. (2015). Effects of electric field intensity and distribution on flame propagation speed of CH4/O2/N2 flames. *Fuel*, *158*,

807–815. https://doi.org/10.1016/j.fuel.2015.05.065
Eraslan, A. N., & Brown, R. C. (1988). Chemiionization and ion-molecule reactions in fuel-rich acetylene flames. *Combustion and Flame*, *74*(1), 19–37. https://doi.org/10.1016/0010-2180(88)90084-3
Feng, A Munir, Z. A. (1995). The Effect of an Electric Field on Self-Sustaining Combustion Synthesis" Part I1. Field-Assisted Synthesis of Beta-SIC, *26*(June), 587–593.
Feroughi, O. M., Deng, L., Kluge, S., Dreier, T., Wiggers, H., Wlokas, I., & Schulz, C. (2017). Experimental and numerical study of a HMDSO-seeded premixed laminar low-pressure flame for SiO2 nanoparticle synthesis. *Proceedings of the Combustion Institute*, *36*(1), 1045–1053. https://doi.org/10.1016/j.proci.2016.07.131
Fialkov, A. B., & Fiaklov, B. S. (1985). Ion content of propane-butane-air flames at reduced pressure. *Combustion, Explosion, and Shock Waves*, *21*(3), 299–307. https://doi.org/10.1007/BF01463845
Fialkov, Alexander B. (1997). Investigation on ions in flames. *Pro& Energy Combusr. Ser*, *23*, 399–528.
Florek, J., Caillard, R., & Kleitz, F. (2017). Evaluation of mesoporous silica nanoparticles for oral drug delivery-current status and perspective of MSNs drug carriers. *Nanoscale*, *9*(40), 15252–15277. https://doi.org/10.1039/c7nr05762h
Friedlander, S. . (2000). *Fundamentals of Aerosol Behavior*. *Oxford university press* (Vol. 10). New York. https://doi.org/10.1089/jam.1997.10.369
Fujimoto, T., Kuga, Y., Pratsinis, S. E., & Okuyama, K. (2003). Unipolar ion charging and coagulation during aerosol formation by chemical reaction. *Powder Technology*, *135–136*, 321–335. https://doi.org/10.1016/S0032-5910(03)00166-9
Garanin, A. F., Tret'Yakov, P. K., & Tupikin, A. V. (2008). Effect of constant and pulsed-periodic electric fields on combustion of a propane-air mixture. *Combustion, Explosion and Shock Waves*, *44*(1), 18–21. https://doi.org/10.1007/s10573-008-0003-3
Goodings, J. M., Bohme, D. K., & Ng, C. W. (1979a). Detailed ion chemistry in methaneoxygen flames. I. Positive ions. *Combustion and Flame*, *36*(C), 27–43. https://doi.org/10.1016/0010-2180(79)90044-0
Goodings, J. M., Bohme, D. K., & Ng, C. W. (1979b). Detailed ion chemistry in methaneoxygen flames. II. Negative ions. *Combustion and Flame*, *36*(C), 45–62. https://doi.org/10.1016/0010-2180(79)90045-2
Granqvist, C. G., & Buhrman, R. A. (1976). Ultrafine metal particles. *Journal of Applied Physics*, *47*(5), 2200–2219. https://doi.org/10.1063/1.322870
Greene, S. . (1963). *A literature survey of ions in flames*. *Defense technical information center*.
Gupta, A. K., & Gupta, M. (2005). Synthesis and surface engineering of iron oxide nanoparticles for biomedical applications. *Biomaterials*, *26*(18), 3995–4021. https://doi.org/10.1016/j.biomaterials.2004.10.012
Halavaara, J., Tervahartiala, P., Isoniemi, H., & Hockerstedt, K. (2002). Efficacy of sequential use of superparamagnetic iron oxide and gadolinium in liver MR imaging. *Acta Radiologica*, *43*(2), 180–185. https://doi.org/10.1034/j.1600-0455.2002.430216.x
Han, J., Belhi, M., Bisetti, F., & Sarathy, S. M. (2015). Numerical modelling of ion transport in flames. *Combustion Theory and Modeliing*, *19*(6), 744–772. https://doi.org/https://doi.org/10.1080/13647830.2015.1090018
Han, J., Belhi, M., Casey, T. A., Bisetti, F., Im, H. G., & Chen, J. Y. (2017). The i-V curve characteristics of burner-stabilized premixed flames: Detailed and reduced models.

Proceedings of the Combustion Institute, *36*(1), 1241–1250. https://doi.org/10.1016/j.proci.2016.05.056

Hansen, J. P., Jensen, J. R., Livbjerg, H., & Johannessen, T. (2001). Synthesis of ZnO particles in a quench-cooled flame reactor. *AIChE Journal*, *47*(11), 2413–2418. https://doi.org/10.1002/aic.690471105

Hardesty, D. R., & Weinberg, F. J. (1973). Electrical control of particulate pollutants from flames. *Symposium (International) on Combustion*, *14*(1), 907–918. https://doi.org/10.1016/S0082-0784(73)80083-9

Havener, R. W., Tsen, A. W., Choi, H. C., & Park, J. (2011). Laser-based imaging of individual carbon nanostructures. *NPG Asia Materials*, *3*(10), 91–99. https://doi.org/10.1038/asiamat.2011.145

Haynes, B. S., Jander, H., & Wagner, H. G. (1979). The effect of metal additives on the formation of soot in premixed flames. *Symposium (International) on Combustion*, *17*(1), 1365–1374. https://doi.org/10.1016/S0082-0784(79)80128-9

Hinds, W. . (1982). *Aerosol Technology Properties, Behavior, and Measurement of Airborne Particles*. *Wiley* (Vol. 31). New York.

Huang, Y., Li, P., Zhao, R., Zhao, L., Liu, J., Peng, S., … Zhang, Z. (2022). Silica nanoparticles: Biomedical applications and toxicity. *Biomedicine and Pharmacotherapy*, *151*(April), 113053. https://doi.org/10.1016/j.biopha.2022.113053

Huseynov, E., Garibov, A., & Mehdiyeva, R. (2016). TEM and SEM study of nano SiO2 particles exposed to influence of neutron flux. *Journal of Materials Research and Technology*, *5*(3), 213–218. https://doi.org/10.1016/j.jmrt.2015.11.001

Janbazi, H., Karakaya, Y., Kasper, T., Schulz, C., Wlokas, I., & Peukert, S. (2019). Development and evaluation of a chemical kinetics reaction mechanism for tetramethylsilane-doped flames. *Chemical Engineering Science*, *209*, 115209. https://doi.org/10.1016/j.ces.2019.115209

Jiang, J., Hogan, C. J., Chen, D. R., & Biswas, P. (2007). Aerosol charging and capture in the nanoparticle size range (6-15 nm) by direct photoionization and diffusion mechanisms. *Journal of Applied Physics*, *102*(3). https://doi.org/10.1063/1.2768061

Kammler, H. K., & Pratsinis, S. E. (2000). Electrically-assisted flame aerosol synthesis of fumed silica at high production rates. *Chemical Engineering and Processing: Process Intensification*, *39*(3), 219–227. https://doi.org/10.1016/S0255-2701(99)00082-3

Kammler, H. K., Pratsinis, S. E., Morrison, P. W., & Hemmerling, B. (2002). Flame temperature measurements during electrically assisted aerosol synthesis of nanoparticles. *Combustion and Flame*, *128*(4), 369–381. https://doi.org/10.1016/S0010-2180(01)00357-1

Katz, J. L., & Hung, C. H. (1991). Initial studies of electric field effects on ceramic powder formation in flames. *Symposium (International) on Combustion*, *23*(1), 1733–1738. https://doi.org/10.1016/S0082-0784(06)80450-9

Kee, R. J., Coltrin, M., & Glarborg, P. (2003). Chemically reacting flow: theory and practice. *Choice Reviews Online*, *41*(01), 41-0330-41–0330. https://doi.org/10.5860/choice.41-0330

Kim, M. K., Chung, S. H., & Kim, H. H. (2012). Effect of electric fields on the stabilization of premixed laminar bunsen flames at low AC frequency: Bi-ionic wind effect. *Combustion and Flame*, *159*(3), 1151–1159. https://doi.org/10.1016/j.combustflame.2011.10.018

Kumfer, B. M., Shinoda, K., Jeyadevan, B., & Kennedy, I. M. (2010). Gas-phase flame synthesis and properties of magnetic iron oxide nanoparticles with reduced oxidation state. *Journal of Aerosol Science*, *41*(3), 257–265. https://doi.org/10.1016/j.jaerosci.2010.01.003

Kusters, K. A., & Pratsinis, S. E. (1995). Strategies for control of ceramic powder synthesis by gas-to-particle conversion. *Powder Technology*, *82*(1), 79–91. https://doi.org/10.1016/0032-5910(94)02892-R

Laskowski, Ł., Laskowska, M., Vila, N., Schabikowski, M., & Walcarius, A. (2019). Mesoporous silica-based materials for electronics-oriented applications. *Molecules*, *24*(13), 1–31. https://doi.org/10.3390/molecules24132395

Lawton, J., & Wienberg, F. . (1963). Maximum ion currents from flames and the maximum practical effects of applied electric fields. In *Proceedings of the Royal Society of London* (pp. 468–497). The Royal Society.

Li, S., Ren, Y., Biswas, P., & Tse, S. D. (2016). Flame aerosol synthesis of nanostructured materials and functional devices: Processing, modeling, and diagnostics. *Progress in Energy and Combustion Science*, *55*, 1–59. https://doi.org/10.1016/j.pecs.2016.04.002

Liu, C., Li, S., Zong, Y., Yao, Q., & Tse, S. D. (2017). Laser-based investigation of the transition from droplets to nanoparticles in flame-assisted spray synthesis of functional nanoparticles. *Proceedings of the Combustion Institute*, *36*(1), 1109–1117. https://doi.org/10.1016/j.proci.2016.06.166

Liu, J. L., Liu, T., Pan, J., Liu, S., & Max Lu, G. Q. (2018). Advances in multicompartment mesoporous silica micro/nanoparticles or theranostic applications. *Annual Review of Chemical and Biomolecular Engineering*, *9*, 389–411. https://doi.org/10.1146/annurev-chembioeng-060817-084225

Liu, X., Ding, J., & Wang, J. (1999). α-Fe2O3 powder of nanosized particles via precursor dispersion. *Journal of Materials Research*, *14*(8), 3355–3362. https://doi.org/10.1557/JMR.1999.0454

Lu, N., & Sorensen, C. M. (1994). Depolarized light scattering from fractal soot aggregates. *Physical Review E*, *50*(4), 3109–3115.

Marcum, S. D., & Ganguly, B. N. (2005). Electric-field-induced flame speed modification. *Combustion and Flame*, *143*(1–2), 27–36. https://doi.org/10.1016/j.combustflame.2005.04.008

Merchan-Merchan, W., Saveliev, A. V., & Taylor, A. M. (2008). High rate flame synthesis of highly crystalline iron oxide nanorods. *Nanotechnology*, *19*(12). https://doi.org/10.1088/0957-4484/19/12/125605

Merchan-Merchan, Wilson, Saveliev, A. V., & Kennedy, L. A. (2004). High-rate flame synthesis of vertically aligned carbon nanotubes using electric field control. *Carbon*, *42*(3), 599–608. https://doi.org/10.1016/j.carbon.2003.12.086

Michelsen, H. A. (2017). Probing soot formation, chemical and physical evolution, and oxidation: A review of in situ diagnostic techniques and needs. *Proceedings of the Combustion Institute*, *36*(1), 717–735. https://doi.org/10.1016/j.proci.2016.08.027

Miles, R. B., Lempert, W. R., & Forkey, J. N. (2001). Laser Rayleigh scattering. *Measurement Science and Technology*, *12*(5). https://doi.org/10.1088/0957-0233/12/5/201

Miller, T. A., Wooldridge, M. S., & Bozzelli, J. W. (2004). Computational modeling of the SiH 3 + O 2 reaction and silane combustion, *137*, 73–92. https://doi.org/10.1016/j.combustflame.2003.12.012

Morrison, P. W., Raghavan, R., Timpone, A. J., Artelt, C. P., & Pratsinis, S. E. (1997). In Situ Fourier Transform Infrared Characterization of the Effect of Electrical Fields on the Flame Synthesis of TiO2 Particles. *Chemistry of Materials*, *9*(12), 2702–2708. https://doi.org/10.1021/cm960508u

Morsi, K. (2017). Combustion synthesis and the electric field: A review. *International Journal of Self-Propagating High-Temperature Synthesis*, *26*(3), 199–209. https://doi.org/10.3103/S1061386217030037

Moses John Christy Appolo, P. I. (n.d.). *E-Field Interactions with Weakly and Strongly Ionized Flames*. North Carolina State University.

Moussawi, A. El, Endres, T., Peukert, S., Zabeti, S., Dreier, T., Fikri, M., & Schulz, C. (2021). Multi-line SiO fluorescence imaging in the flame synthesis of silica nanoparticles from SiCl4. *Combustion and Flame*, *224*, 260–272. https://doi.org/10.1016/j.combustflame.2020.12.020

Ouimet, R. J., Gado, A. M., Bliznakov, S., Bonville, L. J., & Maric, R. (2021). Advanced electrodes for electrochemical energy storage and conversion devices fabricated by reactive spray deposition technology. *Electrochemistry Communications*, *133*(November), 107162. https://doi.org/10.1016/j.elecom.2021.107162

Park, D. G., Chung, S. H., & Cha, M. S. (2016). Bidirectional ionic wind in nonpremixed counterflow flames with DC electric fields. *Combustion and Flame*, *168*, 138–146. https://doi.org/10.1016/j.combustflame.2016.03.025

Pedersen, T., & Brown, R. C. (1993). Pedersen 93 - Simulation of E field effects in premixed methane flame.pdf, *448*, 433–448.

Pfuch, A., Heft, A., Weidl, R., & Lang, K. (2006). Characterization of SiO2 thin films prepared by plasma-activated chemical vapour deposition. *Surface and Coatings Technology*, *201*(1–2), 189–196. https://doi.org/10.1016/j.surfcoat.2005.11.110

Pitts, W., & Kashiwagi, T. (1983). Application of laser-induced Rayleigh light scattering to the study of turbulent mixing., *141*.

Pitts, W. M. (1995). Rayleigh light scattering for concentration measurements in turbulent flows. In *Rayleigh Scattering Diagnostics Workshop*. Gaithersburg: NASA Conference Publication.

Prager, J., Riedel, U., & Warnatz, J. (2007). Modeling ion chemistry and charged species diffusion in lean methane-oxygen flames. *Proceedings of the Combustion Institute*, *31 I*(1), 1129–1137. https://doi.org/10.1016/j.proci.2006.07.141

Pratsinis, E. (1996). Charging and Coagulation During Flame Synthesis of Silica. *J. Aerosol. Sci.*, *27*(6), 951–966.

Pratsinis, E. (1998). Flame aerosol synthesis of ceramic powders. *Fuel and Energy Abstracts*, *39*(5), 384. https://doi.org/10.1016/s0140-6701(98)94112-1

Pratsinis, S. E. (2010). Aerosol-based technologies in nanoscale manufacturing from functional materials to devices through core chemical engineering. *AIChE Journal*, *56*(12).

Rao, P. M., & Zheng, X. (2011). Flame synthesis of tungsten oxide nanostructures on diverse substrates. *Proceedings of the Combustion Institute*, *33*(2), 1891–1898. https://doi.org/10.1016/j.proci.2010.06.071

Ren, Y., Cui, W., & Li, S. (2018). Electrohydrodynamic instability of premixed flames under manipulations of dc electric fields. *Physical Review E*, *97*(1), 1–8. https://doi.org/10.1103/PhysRevE.97.013103

Ren, Y., Li, S., Cui, W., Zhang, Y., & Ma, L. (2017). Low-frequency AC electric field induced thermoacoustic oscillation of a premixed stagnation flame. *Combustion and Flame*, *176*, 479–488. https://doi.org/10.1016/j.combustflame.2016.11.013

Rodrigues, F. S. C., Campos, A., Martins, J., Ambrósio, A. F., & Campos, E. J. (2020). Emerging Trends in Nanomedicine for Improving Ocular Drug Delivery: Light-Responsive

Nanoparticles, Mesoporous Silica Nanoparticles, and Contact Lenses. *ACS Biomaterials Science and Engineering*, *6*(12), 6587–6597. https://doi.org/10.1021/acsbiomaterials.0c01347

Roller, J. M., Kim, S., Kwak, T., Yu, H., & Maric, R. (2017). A study on the effect of selected process parameters in a jet diffusion flame for Pt nanoparticle formation. *Journal of Materials Science*, *52*(16), 9391–9409. https://doi.org/10.1007/s10853-017-1101-y

Roller, J. M., & Maric, R. (2015). A Study on Reactive Spray Deposition Technology Processing Parameters in the Context of Pt Nanoparticle Formation. *Journal of Thermal Spray Technology*, *24*(8), 1529–1541. https://doi.org/10.1007/s11666-015-0322-3

Rudin, T., Tsougeni, K., Gogolides, E., & Pratsinis, S. E. (2012). Flame aerosol deposition of TiO 2 nanoparticle films on polymers and polymeric microfluidic devices for on-chip phosphopeptide enrichment. *Microelectronic Engineering*, *97*, 341–344. https://doi.org/10.1016/j.mee.2012.04.016

Santra, B., Shneider, M. N., & Car, R. (2017). In situ characterization of nanoparticles using rayleigh scattering. *Scientific Reports*, *7*(January), 1–10. https://doi.org/10.1038/srep40230

Schmidt, J., & Ganguly, B. (2013). Effect of pulsed, sub-breakdown applied electric field on propane/air flame through simultaneous OH/acetone PLIF. *Combustion and Flame*, *160*(12), 2820–2826. https://doi.org/10.1016/j.combustflame.2013.06.031

Schulz, H., Mädler, L., Strobel, R., Jossen, R., Pratsinis, S. E., & Johannessen, T. (2005). Independent control of metal cluster and ceramic particle characteristics during one-step synthesis of Pt/TiO2. *Journal of Materials Research*, *20*(9), 2568–2577. https://doi.org/10.1557/JMR.2005.0319

Semenov, E. S., & Sokolik, A. S. (1970). Thermal and chemical ionization in flames. *Combustion, Explosion, and Shock Waves*, *6*(1), 33–43. https://doi.org/10.1007/BF02044894

Serrano-Bayona, R., Chu, C., Liu, P., & Roberts, W. L. (2023). Flame Synthesis of Carbon and Metal-Oxide Nanoparticles: Flame Types, Effects of Combustion Parameters on Properties and Measurement Methods. *Materials*, *16*(3). https://doi.org/10.3390/ma16031192

Shekar, S., Sander, M., Riehl, R. C., Smith, A. J., Braumann, A., & Ã, M. K. (2012). Modelling the flame synthesis of silica nanoparticles from tetraethoxysilane. *Chemical Engineering Science*, *70*, 54–66. https://doi.org/10.1016/j.ces.2011.06.010

Siegel, R. ., & Eastman, J. A. (1989). Synthesis, Characterization, and properties of ananophase ceramics. In *Multicomponent ultrafine microstructures, Material research society*.

Siegel, R. ., Ramasamy, S., Hahn, H., Zongquan, L., Ting, L., & Gronsky, R. (1988). Synthesis, characterization, and properties of nanophase TiO2. *Journal of Materials Research*, *3*(6), 1367–1372.

Sipkens, T. A., Menser, J., Dreier, T., Schulz, C., Smallwood, G. J., & Daun, K. J. (2022). *Laser-induced incandescence for non-soot nanoparticles: recent trends and current challenges*. *Applied Physics B: Lasers and Optics* (Vol. 128). Springer Berlin Heidelberg. https://doi.org/10.1007/s00340-022-07769-z

Smith, G. P., Golden, David M, Frenklach, M., Moriarty, N. W., Eitneer, B., Goldenberg, M., Thomas Bowman, C., … Qin, Z. (1999). GRI-Mech.

Sorensen, C. M. (2001). *Light scattering by fractal aggregates: A review*. *Aerosol Science and Technology* (Vol. 35). https://doi.org/10.1080/02786820117868

Speelman, N., de Goey, L. P. H., & van Oijen, J. A. (2015). Development of a numerical model for the electric current in burner-stabilised methane–air flames. *Combustion Theory and*

Modelling, *19*(2), 159–187. https://doi.org/10.1080/13647830.2014.998712
Speelman, N., Kiefer, M., Markus, D., Maas, U., De Goey, L. P. H., & Van Oijen, J. A. (2015). Validation of a novel numerical model for the electric currents in burner-stabilized methane-air flames. *Proceedings of the Combustion Institute*, *35*(1), 847–854. https://doi.org/10.1016/j.proci.2014.05.067
Srinivas, V., & Pratsinis, S. E. (1995). Corona - assisted flame synthesis of ultrafine titania particles. *Applied Physics Letters*, *3277*(June 1995), 3275–3277. https://doi.org/https://doi.org/10.1063/1.113402
Stamatakis, P., Natalie, C. A., Palmer, B. R., & Yuill, W. A. (1991). Research needs in aerosol processing. *Aerosol Science and Technology*, *14*(3), 316–321. https://doi.org/10.1080/02786829108959493
Starikowskii, A., Skoblin, M., & Hammer, T. (2008). Influence of weak electric fields on flame structure. In *17th Int'l Conf Gas Discharges and Their Applications* (Vol. 19, pp. 629–632).
Strobel, R., Baiker, A., & Pratsinis, S. E. (2006). Aerosol flame synthesis of catalysts. *Advanced Powder Technology*, *17*(5), 457–480. https://doi.org/10.1163/156855206778440525
Strobel, R., & Pratsinis, S. E. (2007). Flame aerosol synthesis of smart nanostructured materials. *Journal of Materials Chemistry*, *17*(45), 4743–4756. https://doi.org/10.1039/b711652g
Styrikovich, M. A., & Mostinskii, I. L. (1977). A Study of the Processes Resulting from the use of Alkaline Seed in Natural Gas Fired MHD Facilities.
Sutton, G., Levick, A., Edwards, G., & Greenhalgh, D. (2006). A combustion temperature and species standard for the calibration of laser diagnostic techniques. *Combustion and Flame*, *147*(1–2), 39–48. https://doi.org/10.1016/j.combustflame.2006.07.013
Tsougeni, K., Papageorgiou, D., Tserepi, A., & Gogolides, E. (2010). "Smart" polymeric microfluidics fabricated by plasma processing: Controlled wetting, capillary filling and hydrophobic valving. *Lab on a Chip*, *10*(4), 462–469. https://doi.org/10.1039/b916566e
Tüncel, Ö., Kahraman, E., Bağci, G., Atabey, N., & Özçelik, S. (2021). Engineered silica nanoparticles are biologically safe vehicles to deliver drugs or genes to liver cells. *Materials Science and Engineering C*, *119*(September 2020), 111585. https://doi.org/10.1016/j.msec.2020.111585
Ulrich, G. D. (1984). Flame synthesis of fine particles. *Chemical & Engineering News Archive*, *62*(32), 22–29. Retrieved from http://pubs.acs.org/doi/abs/10.1021/cen-v062n032.p022%0Ahttp://dx.doi.org/10.1021/cen-v062n032.p022
Vemury, S. (1996). *Flame Synthesis of Nanoparticles - Effect of Charging*. *Dissertation*.
Vemury, Srinivas, Pratsinis, S. E., & Kibbey, L. (1997). Electrically controlled flame synthesis of nanophase TiO2, SiO2, and SnO2 powders. *Journal of Materials Research*, *12*(4), 1031–1042. https://doi.org/10.1557/JMR.1997.0144
Vercoulen, P. H. W., Vemury, S., Pratsinis, S. E., & Marijnissen, J. C. M. (1994). 25.P.39 The effect of electrical charging and dispersion on aerosol coagulation. *Journal of Aerosol Science*, *25*(SUPPL. 1), 427–428. https://doi.org/10.1016/0021-8502(94)90443-X
Vijayakumar, R., & Whitby, K. T. (1984). Flat flame ultrafine aerosol generator. *Aerosol Science and Technology*, *3*(1), 17–24. https://doi.org/10.1080/02786828408958989
Vinogradov, J., Sher, E., Rutkevich, I., & Mond, M. (2001). Voltage-current characteristics of a flame-assisted unipolar corona. *Combustion and Flame*, *127*(1–2), 2041–2050. https://doi.org/10.1016/S0010-2180(01)00305-4
Wang, Y., Sharma, G., Koh, C., Kumar, V., Chakrabarty, R., & Biswas, P. (2017). Influence of flame-generated ions on the simultaneous charging and coagulation of nanoparticles during

combustion. *Aerosol Science and Technology*, *51*(7), 833–844. https://doi.org/10.1080/02786826.2017.1304635

Wegner, K., & Pratsinis, S. E. (2003). Nozzle-quenching process for controlled flame synthesis of titania nanoparticles. *AIChE Journal*, *49*(7), 1667–1675. https://doi.org/10.1002/aic.690490707

Wegner, K., & Pratsinis, S. E. (2004). Flame synthesis of nanoparticles. *Chimica Oggi*, *22*(9), 27–29. https://doi.org/10.1205/cerd.82.11.1444.52025

Wiedensohler, A. (1988). An approximation of the bipolar charge distribution for particles in the submicron size range. *Journal of Aerosol Science*, *19*(3), 387–389. https://doi.org/10.1016/0021-8502(88)90278-9

Wisman, D. L., Marcum, S. D., & Ganguly, B. N. (2008). Chemi-ion-current-induced dissociative recombination in premixed hydrocarbon/air flames. *Journal of Propulsion and Power*, *24*(5), 1079–1084. https://doi.org/10.2514/1.31823

Wortberg, G. (1965). Ion-concentration measurements in a flat flame at atmospheric pressure. *Symposium (International) on Combustion*, *10*(1), 651–655. https://doi.org/10.1016/S0082-0784(65)80210-7

Wu, C. Y. (2005). Nanoparticles and the environment. *Journal of the Air and Waste Management Association*, *55*(6), 708–746. https://doi.org/10.1080/10473289.2005.10464656

Wu, M. ., Windeler, C., Steiner, R., & Bors, T. (1993). Controlled synthesis of nanosized particles by aerosol processes. *Aerosol Science and Technology*, *19*(4), 527–548.

Xing, Y., Koylu, U. O., & Rosner, D. E. (1999). In situ light-scattering measurements of morphologicaliy evolving flame-synthesized oxide nanoaggregates. *Applied Optics*, *38/12*, 2686–2697.

Xiong, G., Kulkarni, A., Dong, Z., Li, S., & Tse, S. D. (2017). Electric-field-assisted stagnation-swirl-flame synthesis of porous nanostructured titanium-dioxide films. *Proceedings of the Combustion Institute*, *36*(1), 1065–1075. https://doi.org/10.1016/j.proci.2016.08.079

Xiong, Y., Pratsinis, S. E., & Mastrangelo, S. V. R. (1992). The effect of ionic additives on aerosol coagulation. *Journal of Colloid And Interface Science*, *153*(1), 106–117. https://doi.org/10.1016/0021-9797(92)90301-2

Xu, F., Liu, X., Tse, S. D., Cosandey, F., & Kear, B. H. (2007). Flame synthesis of zinc oxide nanowires. *Chemical Physics Letters*, *449*(1–3), 175–181. https://doi.org/10.1016/j.cplett.2007.10.045

Xu, F., Zhao, H., & Tse, S. D. (2007). Carbon nanotube synthesis on catalytic metal alloys in methane/air counterflow diffusion flames. *Proceedings of the Combustion Institute*, *31 II*, 1839–1847. https://doi.org/10.1016/j.proci.2006.08.062

Yagodnikov, D. A., & Voronetskii, A. V. (1994). Effect of an external electrical field on ignition and combustion processes. *Combustion, Explosion, and Shock Waves*, *30*(3), 261–268. https://doi.org/10.1007/BF00789414

Yang, G., & Biswas, P. (1997). Study of the sintering of nanosized titania agglomerates in flames using in situ light scattering measurements. *Aerosol Science and Technology*, *27*(4), 507–521. https://doi.org/10.1080/02786829708965491

Yeh, C. L., Zhao, E., & Ma, H. K. (2001a). An experimental investigation of combustion synthesis of silicon dioxide (SiO2) particles in premixed flames. *Combustion Science and Technology*, *173*(1), 25–46. https://doi.org/10.1080/00102200108935843

Yeh, C. L., Zhao, E., & Ma, H. K. (2001b). Combustion synthesis of SiO2 on the aluminum

plate. *Journal of Thermal Science*, *10*(1), 1–5. https://doi.org/10.1007/s11630-001-0017-6
Yu Ting, S. Z. (2008). Metal Oxide Nanostructures from simple metal-oxygen reaction in air. Journal of Materials Science & Technology.
Yue, R., Meng, D., Ni, Y., Jia, Y., Liu, G., Yang, J., … Chen, Y. (2013). One-step flame synthesis of hydrophobic silica nanoparticles. *Powder Technology*, *235*, 909–913. https://doi.org/10.1016/j.powtec.2012.10.021
Zhang, Y., Li, S., Yan, W., Yao, Q., & Tse, S. D. (2011). Role of dipole-dipole interaction on enhancing Brownian coagulation of charge-neutral nanoparticles in the free molecular regime. *Journal of Chemical Physics*, *134*(8). https://doi.org/10.1063/1.3555633
Zhao, H., Liu, X., & Tse, S. D. (2008). Control of nanoparticle size and agglomeration through electric-field- enhanced flame synthesis. *Journal of Nanoparticle Research*, *10*(6), 907–923. https://doi.org/10.1007/s11051-007-9330-7
Zhou, N., Yang, R., & Zhai, T. (2019). Two-dimensional non-layered materials. *Materials Today Nano*, *8*, 100051. https://doi.org/10.1016/j.mtnano.2019.100051

APPENDICES

Appendix A: Calculation of particle yield

The particle yield is calculated as the ratio of weight measured to the theoretical maximum weight possible from complete conversion of HMDSO to SiO_2.

Global two-step reaction scheme for Hexamethyldisiloxane (HMDSO) ($C_6H_{18}OSi_2$) (Feroughi et al., 2017)

$$\text{HMDSO} + \text{OH} \rightarrow 2\ \text{SiO} + 6\ \text{CH}_3 + \text{H} \qquad \text{(R A.1)}$$

$$\text{SiO} + \text{H}_2\text{O} \rightarrow \text{SiO}_2\text{(g)} + \text{H}_2 \qquad \text{(R A.2)}$$

One mole of HMDSO can produce two moles of SiO_2

Yield calculation for +2 kV

Number of moles of HMDSO in 0.09 g = 0.0006

Number of moles of SiO_2 from theoretical calculation = 0.0012

Weight of maximum theoretical SiO_2 = 0.072 g

Yield = (Weight of particles collected) / (maximum theoretical weight of SiO_2)

Y = 70%

Properties of HMDSO and SiO_2

Table A.1. Properties of HMDSO and SiO_2.

The molar mass of HDMSO	162.38 g/mol
Molar mass of SiO_2	60.08 g/mol
The flow rate of HMDSO	0.03 g/min
Weight of HMDSO for three minutes	0.09 g
Weight of SiO_2 collected on 1-inch disc (+2 kV)	10 mg
Weight of SiO_2 collected on 2.25-inch disc (+2 kV)	50 mg

Table A.2. Particle yield calculations.

Voltage,kV)	**Average weight, g**	**The weight of particles on electrode**	**Yield, %**
-7	0.000967	0.004888	6.79
-6	0.000923	0.004669	6.49
-5	0.0012	0.006068	8.43
-4	0.001557	0.007872	10.93
-3	0.001077	0.005445	7.56
-2	0.000773	0.003911	5.43
-1	0.000787	0.003978	5.53
0	0.000863	0.004366	6.06
1	0.008037	0.040641	56.45
2	0.009973	0.050435	70.05
3	0.007677	0.038821	53.92
4	0.007183	0.036326	50.45
5	0.00619	0.031303	43.48
6	0.005867	0.029668	41.21
7	0.005527	0.027948	38.82

Appendix B: Hysteresis plot for the local maxima of current

To find out whether the peak in the VCC occurred when it was recorded with reducing voltage was observed. The peak remained at around 1.5 – 2 kV range for both increasing and decreasing voltages.

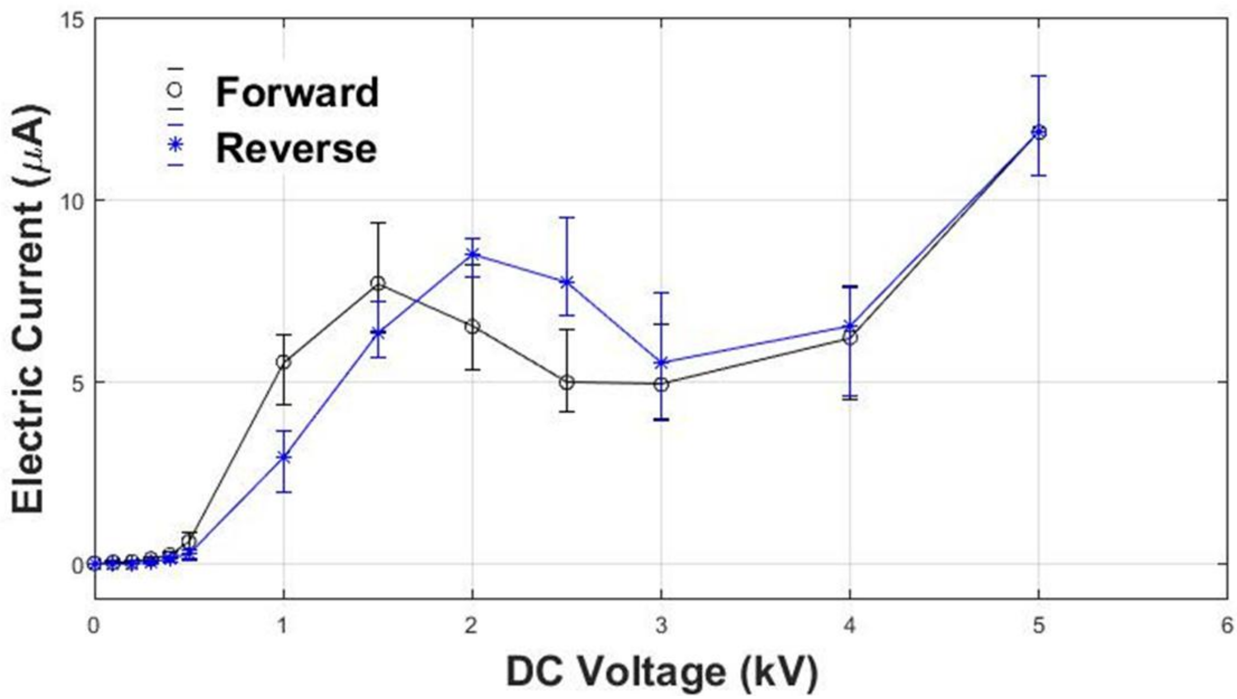

Appendix C: Drift velocity of nanoparticles under the influence of an electric field.

Drift velocity is the average velocity of a charged particle in a material due to an electric field. (https://en.wikipedia.org/wiki/Drift_velocity)

For our case, the drift velocity is calculated by equating the force due to an electric field on a charged particle and the drag force.

Force due to an electric field is given by:

$$F = qE \qquad \text{(R C.1)}$$

- q – is the charge on the particle (C)
- E - is the electric field (kV/m)

The equation for the drift velocity is obtained as,

$$v = -\frac{3}{8}\frac{qE}{(\sqrt{2\pi k_B T m_g})NR^2} \qquad \text{(R C.2)}$$

Where:

- q=1.602*10^{-19} C charge of particle (1-40 charge on each particle)
- m_g =4.65*10^{-26} kg mass of gas molecule
- k_B =1.38*10^{-23} J/K Boltzmann Constant
- E = 1kV/cm Electric Field strength
- R = 10-20 nm size of particle
- N = number density based on Loschmidt constant (m^{-3})

Loschmidt constant (https://chemistrygod.com/loschmidt-constant)

Appendix D: Mass fractions of HMDSO with respect to fuel

The mass fractions of the precursor are calculated as the ratio of HMDSO flow rate to the flow rate of methane in the reaction mixture. The mass fraction is observed to be within a range of 3-5 %, suggesting that HMDSO has an insignificant contribution to the heat released during combustion.

Table D.1. Mass fraction of precursor with respect to reaction mixture.

ϕ	Air (SLM)	Air (kg/min)	Methane (kg/min)	HMDSO (kg/min)	Mass fraction of HMDSO in the mixture	The mass fraction with fuel
0.9	12.4	0.014942	0.0008	0.00003	0.0019	0.038
0.8	12.51	0.0150746	0.0007	0.00003	0.0019	0.042
0.7	12.55	0.0151228	0.0006	0.00003	0.0019	0.048

Appendix E: Cantera governing equations and boundary conditions

Governing Equations

Cantera reduces the three-dimensional governing equation to a single dimension by modeling the flames that are stabilized in an axisymmetric flow (Kee et al., 2003). The following governing equations are used to solve the flame conditions in the 1-D premixed burner stabilized model:

Continuity:

$$\frac{\partial \rho u}{\partial z} = 0 \qquad \text{(R E.1)}$$

Energy:

$$\rho c_p u \frac{\partial T}{\partial z} = \frac{\partial}{\partial z}\left(\lambda \frac{\partial T}{\partial z} \right) - \sum_k j_k c_{p,k} \frac{\partial T}{\partial z} - \sum_k h_k W_k \dot{\omega}_k \qquad \text{(R E.2)}$$

Species:

$$\rho u \frac{\partial Y_k}{\partial z} = \frac{\partial j_k}{\partial z} + W_k \dot{\omega}_k \qquad \text{(R E.3)}$$

where,

- ρ is the density
- u is the axial velocity
- μ is the dynamic viscosity
- c_p is the heat capacity at constant pressure
- T is the temperature
- λ is the thermal conductivity
- Y_k is the mass fraction
- j_k is the diffusive mass flux,

— W_k is the molecular weight, and

— $\dot{\omega}_k$ is the molar production rate of species k.

The equations described are applicable to both ideal and non-ideal gases, which follow the respective equations of state.

7.1.2 Transport model

The mixture-averaged mass flux j_k is used to compute the transport properties of reaction species is described:

Diffusive fluxes:

$$j_k^* = -\rho \frac{W_k}{\overline{\overline{W}}} D_{km}^{'} \frac{\partial X_k}{\partial z} \qquad \text{(R E.4)}$$

$$j_k = j_k^* - Y_k \sum_i j_i^* \qquad \text{(R E.5)}$$

where,

— $\overline{W}$ is the mean molecular weight,

— $D_{km}^{'}$ is the mixture averaged diffusion coefficient,

— X_k is the mole fraction for species *k*.

An additional drift term to account for the transport of charged species in flames is formulated as (Pedersen et al., 1993):

$$j_k^* = -\rho \frac{W_k}{\overline{\overline{W}}} D_{km}^{'} \frac{\partial X_k}{\partial z} + s_k \mu_k E Y_k \qquad \text{(R E.6)}$$

where,

— s_k is the sign of charge (positive (1), negative (-1), and neutral (0) species),

— μ_k is the mobility,

— E is the electric field.

Boundary conditions

The boundary conditions for the 1-D burner stabilized flame model are explained in the current section.

The inlet (z = 0) boundary conditions are:

$$T(0) = T_{burner} \qquad \text{(R E.7)}$$

$$\dot{m}_o = \rho(0)u(0) \qquad \text{(R E.8)}$$

$$\dot{m}_o Y_{k,0} - j_{k-}\rho(0)u(0)Y_k(0) = 0 \qquad \text{(R E.9)}$$

The outlet (z= L) boundary conditions are as follows:

$$\frac{\partial T}{\partial z}(L) = 0 \qquad \text{(R E.10)}$$

$$\frac{\partial Y_k}{\partial z}(L) = 0 \qquad \text{(R E.11)}$$